Supplementary Information for

Parameterization and quantification of two key operando physio-chemical descriptors for water-assisted electro-catalytic organics oxidation

Bailin Tian[1,#], Fangyuan Wang[1,#], Pan Ran[1], Luhan Dai[1], Yang Lv[1], Yuxia Sun[1], Zhangyan Mu[1], Yamei Sun[1], Lingyu Tang[1], William A. Goddard III[2], and Mengning Ding[1]*

[1] Key Laboratory of Mesoscopic Chemistry, School of Chemistry and Chemical Engineering, Nanjing University, Nanjing, Jiangsu, 210023, China

[2] Materials and Process Simulation Center (MSC) and Liquid Sunlight Alliance (LiSA), California Institute of Technology, Pasadena, California 91125, United States

[#] B.T. and F.W. contributed equally to this work.

*Corresponding Author: mding@nju.edu.cn

Contents

Experimental methods

Chemicals. All chemical reagents were used as received without further purification (except for KOH). Co(NO$_3$)$_2$·6H$_2$O (99.99%), Ni(NO$_3$)$_2$·6H$_2$O (99.999%), NiCl$_2$·6H$_2$O (99.95%), KOH (99.999%), ultra-pure water (Milli-Q filtered, 18.2 MΩ·cm), PMMA (A8, MicroChem), PVP (average molecular weight: 40000), methanol (99.9%, chromatography grade), NaBH$_4$ (98%), furfural (99%), furfuryl alcohol (98%), 5-hydroxymethylfurfural (99.54%), benzylamine (>99.0%), benzyl nitrile (>99%), benzyl alcohol (≥99%), benzaldehyde (99%), benzoic acid (99%).

Purification procedures to prepare Fe-free KOH aqueous solution. For rigorously Fe-free measurements, the 1 M KOH electrolyte was purified according to the procedures reported in literature.[1]

Fabrication of the hydroxide devices. A free standing film was prepared by a co-solvent evaporation method,[2-5] the detailed synthesis procedures can be found in our previous work.[6]

The relationship between reaction rate and current density (Note 1)

The reaction rate equation for a typical bimolecular adsorption reaction following a Langmuir-Hinshelwood (L-H) mechanism at gas-solid interfaces can be found in the textbook:

$$r = k \cdot \theta_A \cdot \theta_B \qquad (1)$$

$$r = \frac{k \cdot a_A a_B p_A p_B}{(1 + a_A p_A + a_B p_B)^2} \qquad (2)$$

Where r is the reaction rate, k is the reaction rate constant, θ_A and θ_B represent the surface coverages of the two species, p_A and p_B represent the partial pressure of two gases.

In the typical water-oxidation-assisted electro-oxidation of organics, the electrochemical current can be calculated by:

$$i = FAk^0 \exp\left[\frac{\alpha F(E - E_i^0)}{RT}\right] \cdot C_{OH^-} \qquad (3)$$

Where i is the electrochemical current, F is the Faraday constant, A is the electrode area, k^0 is the reaction rate constant, α is the transfer coefficient, R and T are universal gas constant and temperature, C_{OH^-} is the concentration of OH$^-$. Due to the high irreversibility of elementary steps in oxygen evolution reaction, we do not consider the reverse electrochemical reaction.

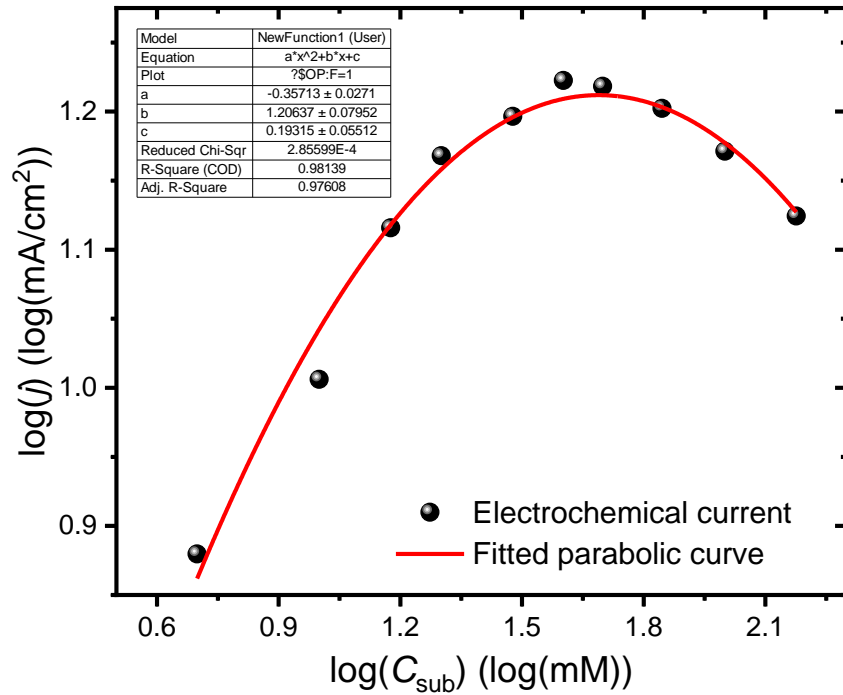If there is no organics exist in the system, the value of i is positively correlated with the surface coverage of OH* (θ_{OH^*}). The expression for the reaction rate between OH * and the adsorbed substrate is:

$$r = k \cdot \theta_{\text{OH}^*} \cdot \theta_{\text{sub}^*} \qquad (4)$$

Where r is the reaction rate, k is the reaction rate constant, θ_{OH^*} and θ_{sub^*} represent the surface coverages of OH* and organic substrates.

In the low concentration range, the θ_{sub^*} is also positively correlated with concentration/activity of substances (C_{sub}). **Thus the reaction rate is positively correlated with electrochemical current in the water-oxidation-assisted organic substances electro-oxidation reaction.**

We found the shape of experimental current densities with varying concentrations of substances is like a quadratic function.

Model	NewFunction1 (User)
Equation	a*x^2+b*x+c
Plot	?$OP:F=1
a	-0.35713 ± 0.0271
b	1.20637 ± 0.07952
c	0.19315 ± 0.05512
Reduced Chi-Sqr	2.85599E-4
R-Square (COD)	0.98139
Adj. R-Square	0.97608

Supplementary Figure S1. The fitted parabolic curve for electrochemical oxidation currents.

The fitting results shown the function expression is:

$$\log(j) = -0.35713 \times (\log(C_{\text{sub}}))^2 + 1.20637 \times \log(C_{\text{sub}}) + 0.19315 \qquad (5)$$

Where C_{sub} is the concentration of substances (mM).

The reaction rate equation can be also transformed into a function of θ_{sub^*}:

$$\theta_{\text{OH}^*} = 1 - \theta_{\text{sub}^*} \tag{6}$$

$$r = k \cdot \theta_{\text{sub}^*} \cdot (1 - \theta_{\text{sub}^*})$$

$$r = -k \cdot \theta_{\text{sub}^*}{}^2 + k \cdot \theta_{\text{sub}^*} \tag{7}$$

Interestingly, the reaction rate equation is also a form of quadratic function. The experimental current densities and simulated curve using equation S7 match with each other relatively good (**Supplementary Figure 1B** in main text), **indicating the θ_{sub^*} is proportional to log(C_{sub}) at the certain concentration range, which is similar to the Тёмкин's adsorption isotherm equation (θ is proportional to log(p)) for the chemical adsorption of single molecular layer**.

$$\theta_{\text{sub}^*} \propto \log(C_{\text{sub}}) \tag{8}$$

$$r = -k' \cdot (\log(C_{\text{sub}}))^2 + k' \cdot \log(C_{\text{sub}}) \tag{9}$$

Simultaneous equations S5, S7 and S9, the functional relationship between the reaction rate and electrochemical current in water-oxidation-assisted organics electro-oxidation can be expressed as:

$$r = -k' \cdot \left[\frac{1.20637 + \sqrt{1.20637^2 + 4 \times 0.35713 \times (0.19315 - \log(j))}}{2 \times 0.35713} \right]^2$$

$$+ k' \cdot \frac{1.20637 + \sqrt{1.20637^2 + 4 \times 0.35713 \times (0.19315 - \log(j))}}{2 \times 0.35713}$$

Replace the constant in the special case, and the general expression is:

$$r = -k' \cdot \left[\frac{b + \sqrt{b^2 + 4a \times (c - \log(j))}}{2a} \right]^2$$

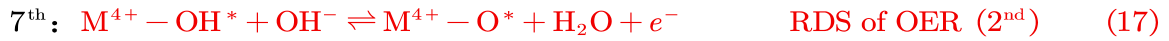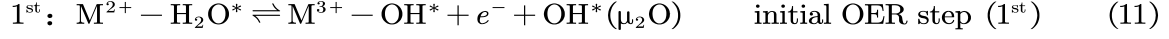$$+ k' \cdot \frac{b + \sqrt{b^2 + 4a \times (c - \log(j))}}{2a} \tag{10}$$

Where a, b, c are constants in the fitted quadratic equation with one unknown for log(j). Equation S10 could predict the existence of a maximum reaction rate and effectively predict the positive correlation between reaction rate and electrochemical current density.
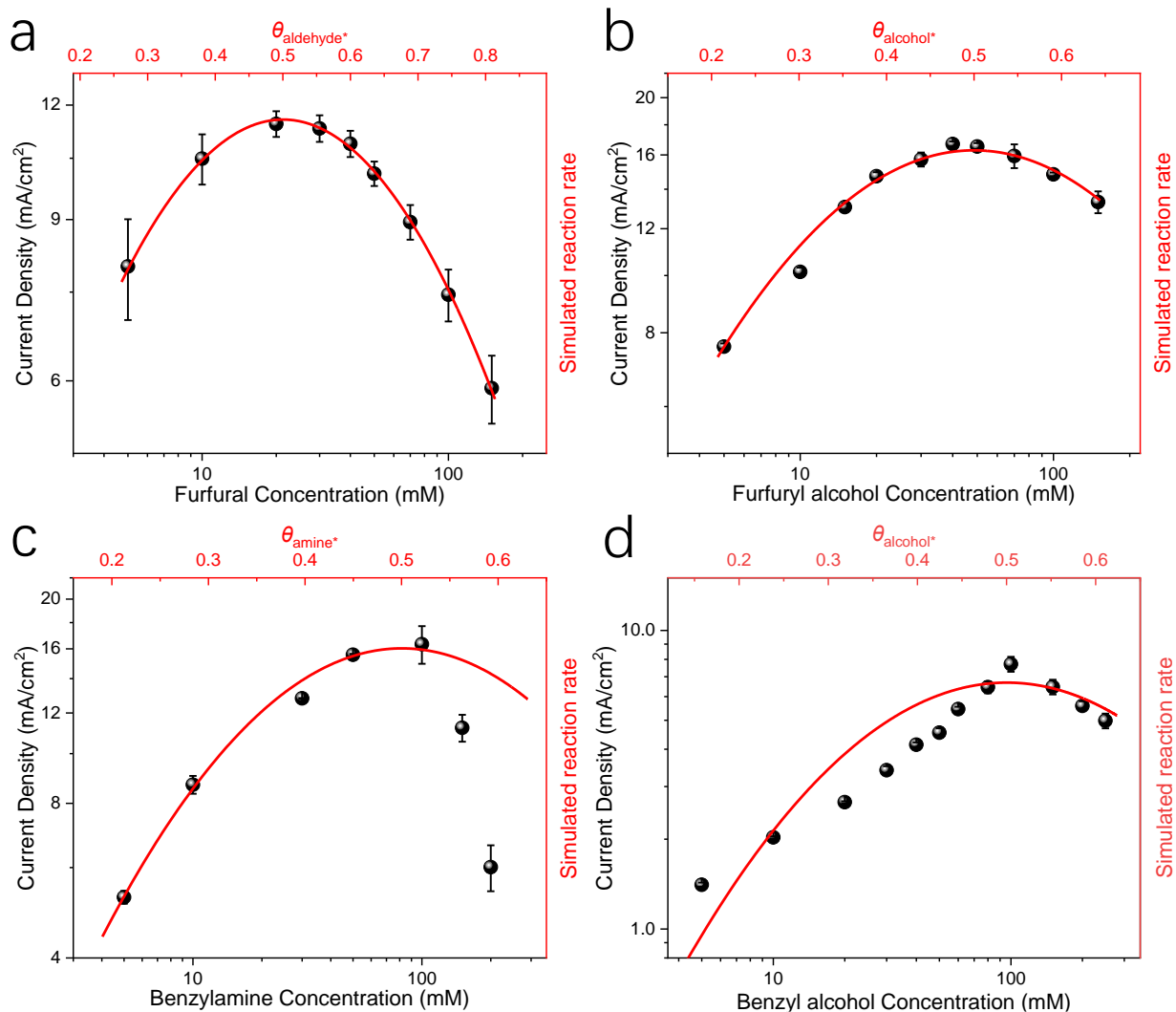
Supplementary Figure S2. The experimental kinetic and simulation results for electro-catalytic organic oxidation reactions (EOOR) assuming a surface bimolecular adsorption/reaction (Langmuir-Hinshelwood) mechanism. Dependence of electro-oxidation partial current densities on the varying organic substrate concentrations for (a) furfural (in 1.0 M KOH), (b) furfuryl alcohol (in 1.0 M KOH), (c) benzylamine (in 1.0 M KOH) and (d) benzyl alcohol (in 1.0 M K_2CO_3, weak alkaline) in which reaction rate vertexes $@\theta_{sub*} = 0.5$ were observed. Error bars were obtained from three independent experiments.

Models for micro-kinetic and thermodynamic analysis (Note 2)

I. Micro-kinetic simulation for qualitative surface coverages of intermediates

1st：$M^{2+} - H_2O^* \rightleftharpoons M^{3+} - OH^* + e^- + OH^* (\mu_2 O)$ initial OER step (1st) (11)

2nd：$M^{2+*} + \text{substance} \rightarrow M^{2+} - \text{substance}^*$ organic adsorption   (12)

3rd：$M^{3+} - OH^* \rightleftharpoons M^{4+} - OH^* + e^-$ initial OER step (1.5^{th}) (13)

4th：$M^{3+} - OH^* + \text{substance}^* \Rightarrow \Rightarrow \text{product}^*$ catalytic oxidation   (14)

5th：$M^{4+} - OH^* + \text{substance}^* \Rightarrow \Rightarrow \text{product}^*$ catalytic oxidation   (15)

6th：$\text{product}^* \rightarrow * + \text{product}$ organic desorption   (16)

7th：$M^{4+} - OH^* + OH^- \rightleftharpoons M^{4+} - O^* + H_2O + e^-$ RDS of OER (2nd) (17)

8th：$O^* + OH^- \rightleftharpoons OOH^* + e^-$ late OER step (3rd) (18)

9th：$OOH^* + OH^- \rightleftharpoons OO^* + H_2O + e^-$ late OER step (4th) (19)

10th：$OO^* \rightarrow * + O_2$ O_2 evolution   (20)

For qualitatively analysis the relationship of $\Delta V_{harmonic}$ and surface $M^{3+/4+}-OH^*$ coverage, we consider,

$$E^0 = G^{\ominus}/e \qquad (21)$$

where the E^0 and $G^{\ominus}$ represent the equilibrium potential of an electron transfer step and its Gibbs free energy in the standard condition.

The equilibrium potential of each elementary step can be obtained from the difference of Gibbs free energy between reactants and products.

$$E_1^0 = \frac{\Delta G_{M^{3+}-OH^*} - \Delta G_{M^{2+}-*+OH^-}}{e} \qquad (22)$$

$$E_3^0 = \frac{\Delta G_{M^{4+}-OH^*} - \Delta G_{M^{3+}-OH^*}}{e} \qquad (23)$$

$$E_7^0 = \frac{\Delta G_{M^{4+}-O^*} - \Delta G_{M^{4+}-OH^*}}{e} \qquad (24)$$

$$E_8^0 = \frac{\Delta G_{M^{4+}-OOH^*} - \Delta G_{M^{4+}-O^*}}{e} \qquad (25)$$

$$E_9^0 = \frac{\Delta G_{M^{4+}-OO^*} - \Delta G_{M^{4+}-OOH^*}}{e} \qquad (26)$$

E_i^0 is the equilibrium potential of ith reaction. ΔG is the adsorption energy of intermediates (eV) and its numerical value equals to E_i^0.[7]

Due to the low reversibility of the reactions in OER and EOOR systems, the reaction rates of inverse reaction were omitted.

$$r_i = k_i^0 \exp\left[\frac{\beta F(E - E_i^0)}{RT}\right] \cdot \theta_\xi \qquad (27)$$

$$\sum_{i=1}^{i} \theta_\xi = 1 \qquad (28)$$

where the r_i is the forward reaction rate of the ith reaction; k_i^0 is the rate constant of ith reaction; β is the symmetry factor; θ_ξ is the surface coverage of the species; R and T are the universal gas constant and temperature, respectively.

For the microkinetic simulations, consider the differential equations for surface coverage of each species among all of the reactions:

$$\frac{d\theta_{\text{M}^{3+}-\text{OH}^*}}{dt} = r_1 - r_3 - r_4$$

$$= k_1^0 \exp\left[-\frac{\beta F E_1^0}{RT}\right] \exp\left[\frac{\beta F E(t)}{RT}\right] \cdot \theta_{\text{M}^{2+}-*} \cdot a_{\text{OH}^-} - k_3^0 \exp\left[-\frac{\beta F E_3^0}{RT}\right] \exp\left[\frac{\beta F E(t)}{RT}\right] \cdot \theta_{\text{M}^{3+}-\text{OH}^*} - k_4^0 \cdot \theta_{\text{M}^{3+}-\text{OH}^*} \cdot \theta_{\text{sub}^*} \qquad (29)$$

$$\frac{d\theta_{\text{sub}^*}}{dt} = r_2 - r_4 - r_5$$

$$= k_2^0 \cdot \theta_{\text{M}^{2+}-*} \cdot a_{\text{sub}} - k_4^0 \cdot \theta_{\text{M}^{3+}-\text{OH}^*} \cdot \theta_{\text{sub}^*} - k_5^0 \cdot \theta_{\text{M}^{4+}-\text{OH}^*} \cdot \theta_{\text{sub}^*} \qquad (30)$$

$$\frac{d\theta_{\text{M}^{4+}-\text{OH}^*}}{dt} = r_3 - r_5 - r_7$$

$$= k_3^0 \exp\left[-\frac{\beta F E_3^0}{RT}\right] \exp\left[\frac{\beta F E(t)}{RT}\right] \cdot \theta_{\text{M}^{3+}-\text{OH}^*} - k_5^0 \cdot \theta_{\text{M}^{4+}-\text{OH}^*} \cdot \theta_{\text{sub}^*} - k_7^0 \exp\left[-\frac{\beta F E_7^0}{RT}\right] \exp\left[\frac{\beta F E(t)}{RT}\right] \cdot \theta_{\text{M}^{4+}-\text{OH}^*} \cdot a_{\text{OH}^-} \qquad (31)$$

$$\frac{d\theta_{\text{M}^{4+}-\text{O}^*}}{dt} = r_7 - r_8$$

$$= k_7^0 \exp\left[-\frac{\beta F E_7^0}{RT}\right] \exp\left[\frac{\beta F E(t)}{RT}\right] \cdot \theta_{\text{M}^{4+}-\text{OH}^*} \cdot a_{\text{OH}^-} - k_8^0 \exp\left[-\frac{\beta F E_8^0}{RT}\right] \exp\left[\frac{\beta F E(t)}{RT}\right] \cdot \theta_{\text{M}^{4+}-\text{O}^*} \cdot a_{\text{OH}^-} \qquad (32)$$

$$\frac{d\theta_{\text{M}^{4+}-\text{OOH}^*}}{dt} = r_8 - r_9$$

$$= k_8^0 \exp\left[-\frac{\beta F E_8^0}{RT}\right] \exp\left[\frac{\beta F E(t)}{RT}\right] \cdot \theta_{\text{M}^{4+}-\text{O}^*} \cdot a_{\text{OH}^-} - k_9^0 \exp\left[-\frac{\beta F E_9^0}{RT}\right] \exp\left[\frac{\beta F E(t)}{RT}\right] \cdot \theta_{\text{M}^{4+}-\text{OOH}^*} \cdot a_{\text{OH}^-} \qquad (33)$$

$$\frac{d\theta_{\text{prod}^*}}{dt} = r_4 + r_5 - r_6$$

$$= k_4^0 \cdot \theta_{\text{M}^{3+}-\text{OH}^*} \cdot \theta_{\text{sub}^*} + k_5^0 \cdot \theta_{\text{M}^{4+}-\text{OH}^*} \cdot \theta_{\text{sub}^*} - k_6^0 \cdot \theta_{\text{prod}^*} \qquad (34)$$

$$\frac{d\theta_{\text{M}^{4+}-\text{OO}^*}}{dt} = r_9 - r_{10}$$

$$= k_9^0 \exp\left[-\frac{\beta F E_9^0}{RT}\right] \exp\left[\frac{\beta F E(t)}{RT}\right] \cdot \theta_{\text{M}^{4+}-\text{OOH}^*} \cdot a_{\text{OH}^-} - k_{10}^0 \cdot \theta_{\text{M}^{4+}-\text{OO}^*} \qquad (35)$$

$$\theta_{\text{M}^{2+}-*} = 1 - \theta_{\text{sub}^*} - \theta_{\text{M}^{3+}-\text{OH}^*} - \theta_{\text{M}^{4+}-\text{OH}^*} - \theta_{\text{M}^{4+}-\text{O}^*} - \theta_{\text{M}^{4+}-\text{OOH}^*} - \theta_{\text{M}^{4+}-\text{OO}^*} \qquad (36)$$

We use the "ode15s" function in Matlab (R2019b) to solve these differential equations. Part of the parameters used for the microkinetic simulations are listed in **Supplementary Table S1**:

Table S1. Parameters used for simulation of qualitative surface coverages of intermediates. [a]

Parameters \ Materials	α-Co(OH)$_2$	α-Ni(OH)$_2$
E_{1st}^0 (V vs. RHE)	1.00	1.12
E_{3rd}^0 (V vs. RHE)	1.30	1.25
E_{7th}^0 (V vs. RHE)	1.60	1.65
E_{8th}^0 (V vs. RHE)	1.65	1.70
E_{9th}^0 (V vs. RHE)	1.66	1.71
β	0.40	0.40

[a] The numerical values of these parameters have been referenced from reported literature[8] and adjusted appropriately. The accuracy of the parameters is far outside the scope of this work. Their values may vary a lot depending on the used simulation method.

With the differential equations and parameters in hand, we can use the Matlab (R2019b) software to obtain varied surface coverages of the species in dependent with applied potential, and the overall current can be calculated by:

$$j = \sum_{i=1}^{i} k_i^0 \exp\left[\frac{\beta F (E - E_i^0)}{RT} \right] \cdot \theta_\xi \cdot a_{\mathrm{OH}^-} \cdot F \qquad (37)$$
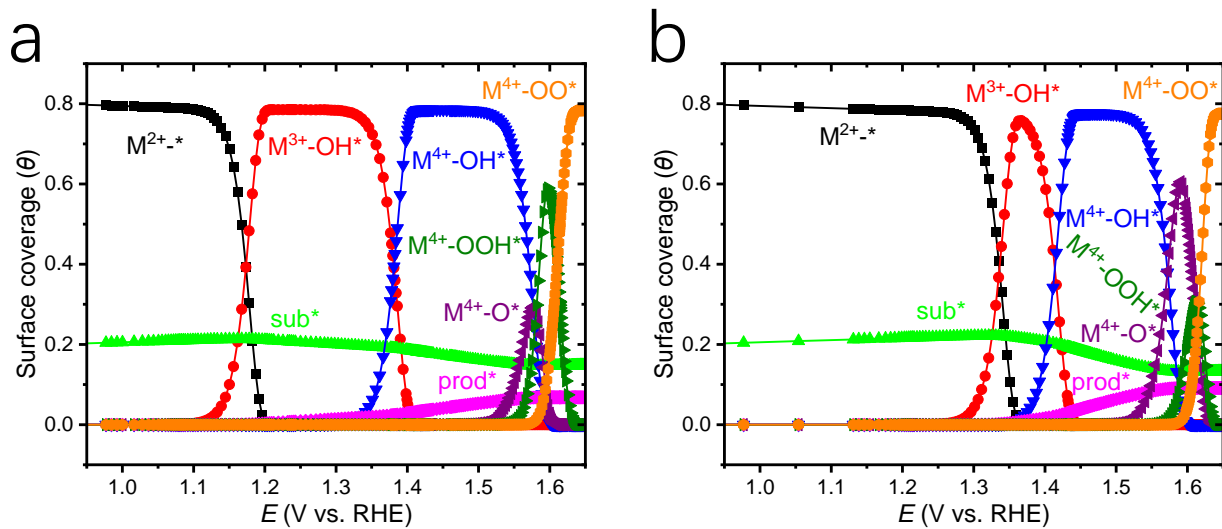
Supplementary Figure S3. The micro-kinetic simulation results of surface coverages of possible species

for α-Co(OH)₂ (a) and α-Ni(OH)₂ (b).
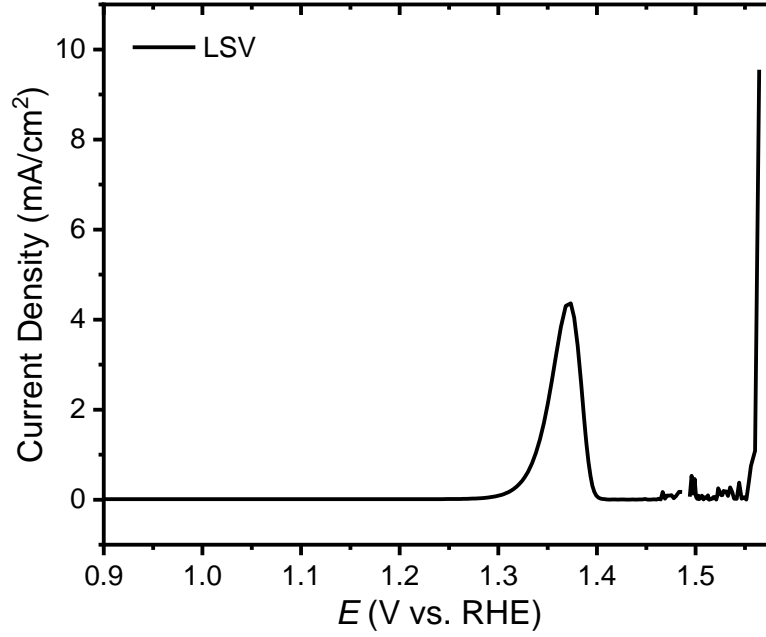
Supplementary Figure S4. The micro-kinetic simulation results of LSV.

II. Micro-kinetic analysis for the fitting of rate constants in experimental electro-oxidation reaction

Considering the same elementary steps in part I, the reaction rate is given by:

$$r_1 = k_1' \theta_* a_{H_2O} e^{\alpha f \varphi} = k_1 \theta_* a_{H_2O} \tag{38}$$

$$K_2 = \frac{\gamma_{sub} \theta_{sub}}{\gamma c \gamma_* \theta_*} \tag{39}$$

$$r_3 = k_3' \theta_{M^{3+}-OH^*} e^{\alpha f \varphi} = k_3 \theta_{M^{3+}-OH^*} \tag{40}$$

$$r_4 = k_4 \theta_{M^{3+}-OH^*} \theta_{sub} \tag{41}$$

$$r_5 = k_5 \theta_{M^{4+}-OH^*} \theta_{sub} \tag{42}$$

$$r_7 = k_7' \theta_{M^{4+}-OH^*} e^{\alpha f \varphi} = k_7 \theta_{M^{4+}-OH^*} \tag{43}$$

$$r_8 = k_8' \theta_{M^{4+}-O^*} e^{\alpha f \varphi} = k_8 \theta_{M^{4+}-O^*} \tag{44}$$

$$r_9 = k_9' \theta_{M^{4+}-OOH^*} e^{\alpha f \varphi} = k_9 \theta_{M^{4+}-OOH^*} \tag{45}$$

$$r_{10} = k_{10} \theta_{M^{4+}-OO^*} \tag{46}$$

We apply the pseudo-steady-state hypothesis (PSSH) to the water oxidation intermediates[9]:

$$\frac{\mathrm{d}\Gamma_{\mathrm{M}^{3+}-\mathrm{OH}^*}}{\mathrm{d}t} = r_1 - r_3 - r_4 = 0, \quad \frac{\mathrm{d}\Gamma_{\mathrm{M}^{4+}-\mathrm{OH}^*}}{\mathrm{d}t} = r_3 - r_5 - r_7 = 0,$$

$$\frac{\mathrm{d}\Gamma_{\mathrm{M}^{4+}-\mathrm{O}^*}}{\mathrm{d}t} = r_7 - r_8 = 0, \quad \frac{\mathrm{d}\Gamma_{\mathrm{M}^{4+}-\mathrm{OOH}^*}}{\mathrm{d}t} = r_8 - r_9 = 0,$$

$$\frac{\mathrm{d}\Gamma_{\mathrm{M}^{4+}-\mathrm{OO}^*}}{\mathrm{d}t} = r_9 - r_{10} = 0 \qquad (47)$$

Substitution of Eq S38-S46 into Eq S47 gives:

$$\theta_{\mathrm{sub}^*} = \frac{K_2 \gamma c \gamma_* \theta_*}{\gamma_{\mathrm{sub}}} = k_2 c \theta_* \qquad (48)$$

$$\theta_{\mathrm{M}^{3+}-\mathrm{OH}^*} = \frac{k_1 \theta_* a_{\mathrm{H}_2\mathrm{O}}}{k_3 + k_4 k_2 c \theta_*} \qquad (49)$$

$$\theta_{\mathrm{M}^{4+}-\mathrm{OH}^*} = \frac{k_1 k_3 \theta_* a_{\mathrm{H}_2\mathrm{O}}}{(k_3 + k_4 k_2 c \theta_*) \cdot (k_7 + k_5 k_2 c \theta_*)} \qquad (50)$$

$$\theta_{\mathrm{M}^{4+}-\mathrm{O}^*} = \frac{k_1 k_3 k_7 \theta_* a_{\mathrm{H}_2\mathrm{O}}}{k_8 (k_3 + k_4 k_2 c \theta_*) \cdot (k_7 + k_5 k_2 c \theta_*)} \qquad (51)$$

$$\theta_{\mathrm{M}^{4+}-\mathrm{OOH}^*} = \frac{k_1 k_3 k_7 \theta_* a_{\mathrm{H}_2\mathrm{O}}}{k_9 (k_3 + k_4 k_2 c \theta_*) \cdot (k_7 + k_5 k_2 c \theta_*)} \qquad (52)$$

$$\theta_{\mathrm{M}^{4+}-\mathrm{OO}^*} = \frac{k_1 k_3 k_7 \theta_* a_{\mathrm{H}_2\mathrm{O}}}{k_{10} (k_3 + k_4 k_2 c \theta_*) \cdot (k_7 + k_5 k_2 c \theta_*)} \qquad (53)$$

Then the reaction rate of electro-oxidation can be expressed as:

$$r = r_4 + r_5 = k_4 \theta_{\mathrm{M}^{3+}-\mathrm{OH}^*} \theta_{\mathrm{sub}^*} + k_5 \theta_{\mathrm{M}^{4+}-\mathrm{OH}^*} \theta_{\mathrm{sub}^*}$$

$$= \frac{k_1 k_4 \theta_* a_{\mathrm{H}_2\mathrm{O}} k_2 c \theta_*}{k_3 + k_4 k_2 c \theta_*} + \frac{k_1 k_3 k_5 \theta_* a_{\mathrm{H}_2\mathrm{O}} k_2 c \theta_*}{(k_3 + k_4 k_2 c \theta_*) \cdot (k_7 + k_5 k_2 c \theta_*)} \qquad (54)$$

Fitting method:

We used the curves fitting tool in the Matlab (R2019b) to fit the kinetics data. Robustness: off; algorithm: Trust-region; DiffMinChange: 1E-8; DiffMaxchange: 0.1; MaxFunEvals: 600; Maxlter: 400; TolFun: 1E-6; TolX: 1E-6.

The best fit of reaction rate of alcohol electro-oxidation using the second term of Eq. S54 was shown in **Supplementary Figure S5**:
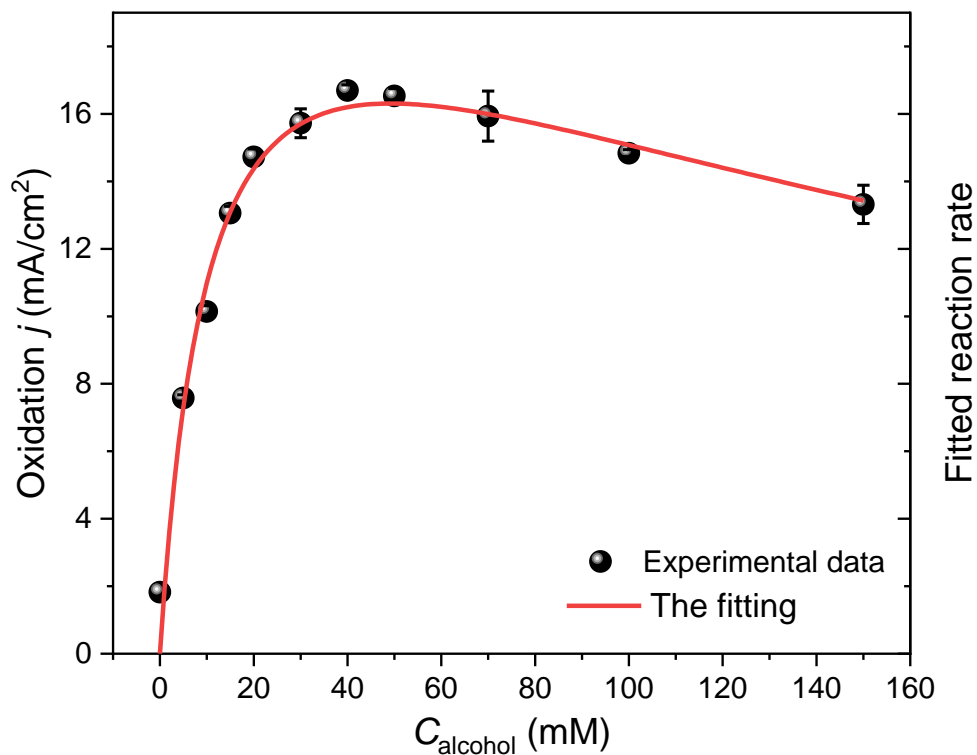
Supplementary Figure S5. The micro-kinetic analysis of OH* as reactive specie. Data points depict the dependence of experimental partial current densities (equivalent to reaction rates under high FEs), and the red curve shows the mathematical fitting of the kinetic data. Error bars were obtained from three independent experiments.

Supplementary Table S2. Parameters used for rate constants fitting in experimental electro-oxidation reaction.

Reactive species	k_1 (s^{-1})	k_2 (s^{-1})	k_3 (s^{-1})	k_4 (s^{-1})	k_5 (s^{-1})	k_7 (s^{-1})	R-square	Adjusted R-square	RMSE
OH*	50	0.4736	90.04	1.842	2.492	6.908	0.9781	0.9636	0.8756

It is found that the rate constants of electron transfer steps (E, k_1 and k_3 of equations 11 and 13) are much higher than chemical catalytic reactions (C).

Materials characterization
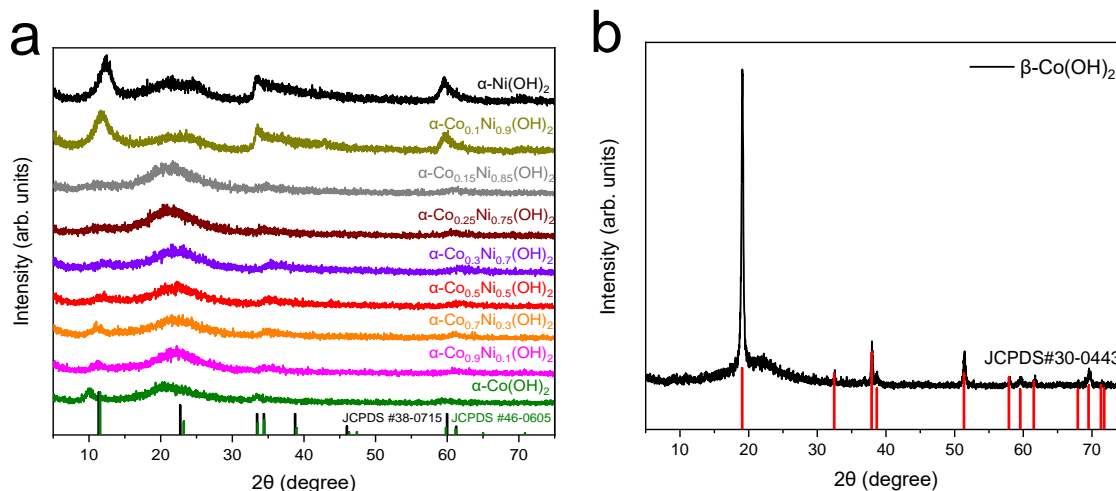
Supplementary Figure S6. The XRD pattern of a series of α type Ni doped Co hydroxides (a) and β type Co hydroxides (b).

The diffraction peaks of a series of hydroxides stay closely to the standard PDF cards of α-Co(OH)$_2$ (JCPDS #46-0605)[10-12] and α-Ni(OH)$_2$ (JCPDS #38-0715)[13], except for the first diffraction peak around 10°, which is probably the reason of different synthetic methods induced different degrees of alkali metal ions (Na$^+$, K$^+$) intercalation.
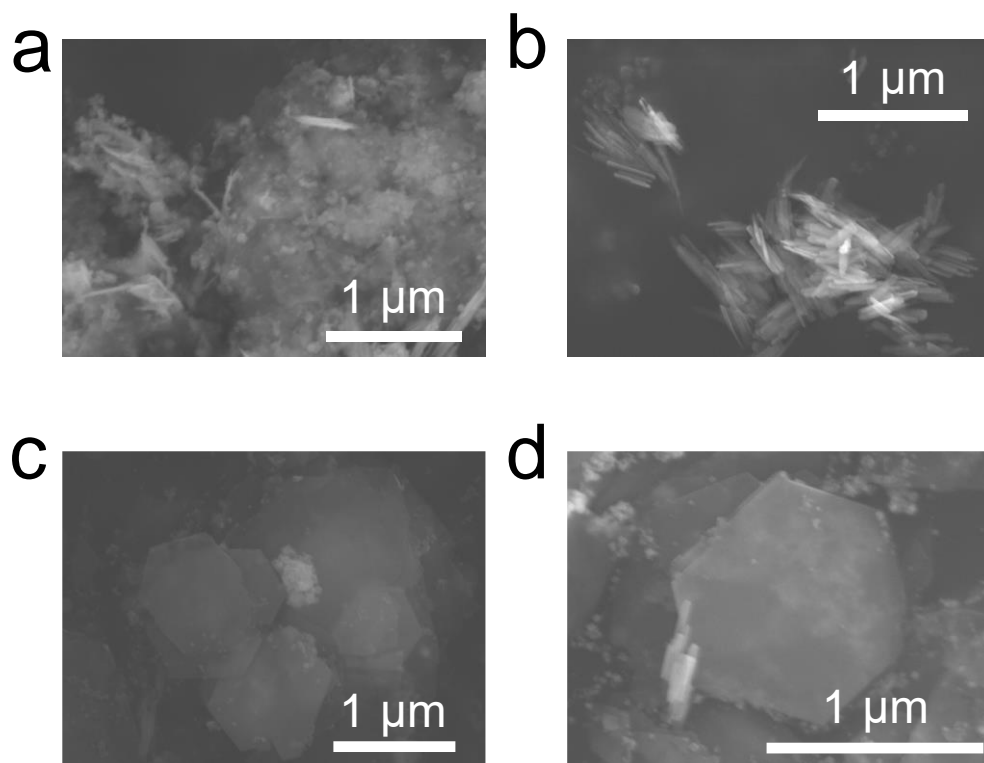
Supplementary Figure S7. The scanning electron microscope (SEM) images of α-Co(OH)$_2$ (a, b) and β-Co(OH)$_2$ (c, d), scale bars are 1 μm.
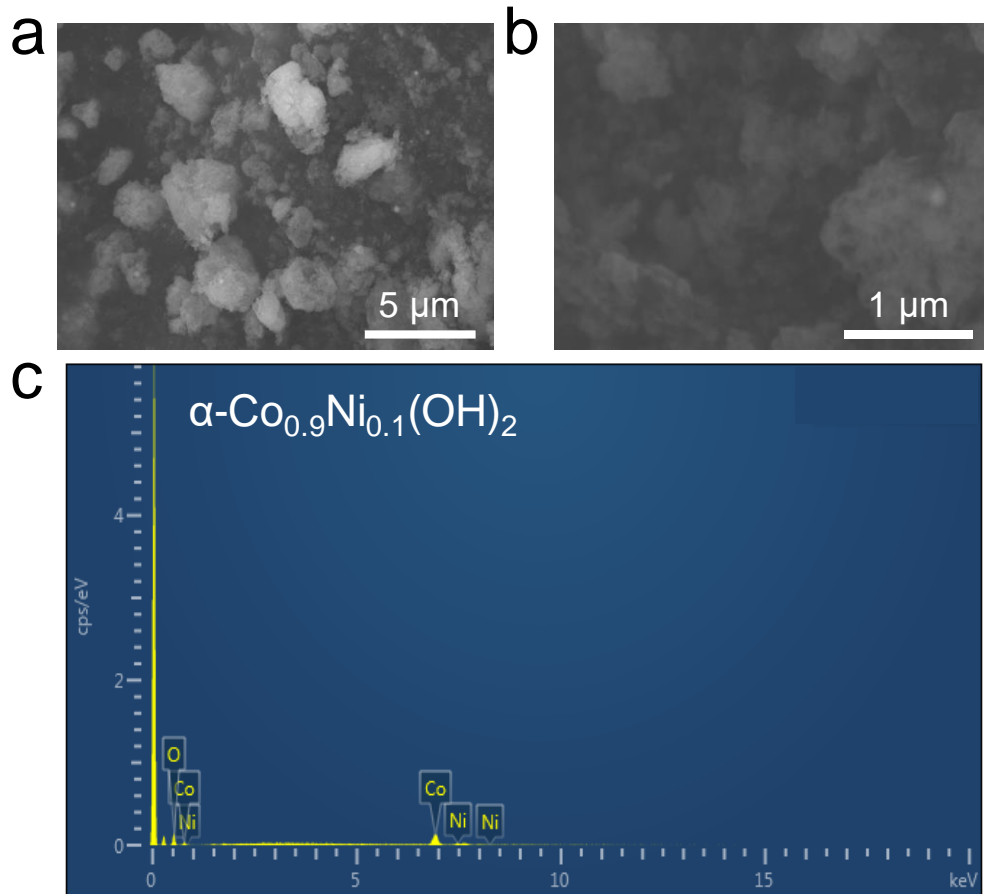
a

b

c

$\alpha\text{-Co}_{0.9}\text{Ni}_{0.1}(\text{OH})_2$

Elements	Line Type	Apparent concentration	k ratio	wt%	wt% Sigma	Standard sample label
O	K line	7.96	0.02679	14.41	1.06	SiO_2
Co	K line	28.89	0.28895	76.60	2.34	Co
Ni	K line	3.51	0.03512	8.98	2.44	Ni
Total:				100.00		
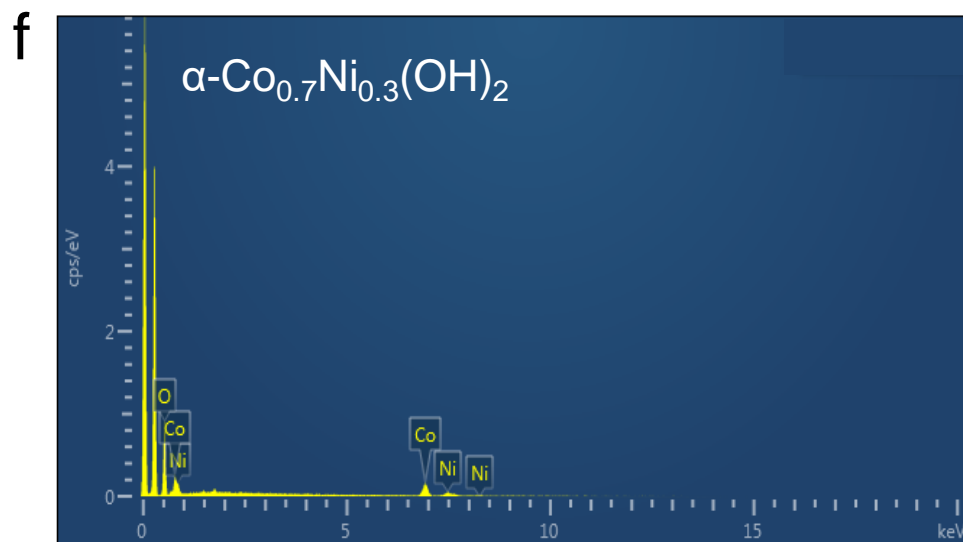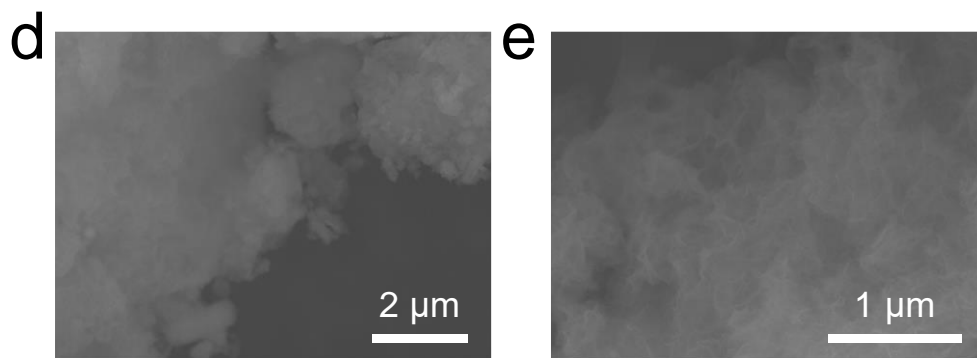
d

2 µm

e

1 µm

f

$\alpha\text{-Co}_{0.7}\text{Ni}_{0.3}(\text{OH})_2$

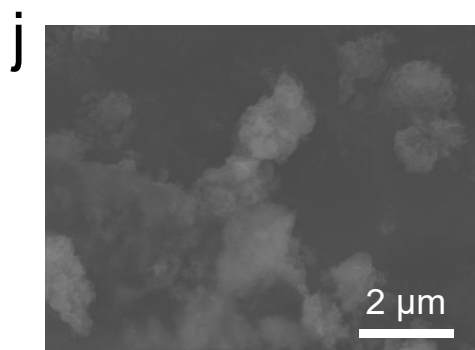| Elements	Line Type	Apparent concentration	k ratio	wt%	wt% Sigma	Standard sample label
O	K line	29.65	0.09976	39.95	1.19	SiO_2
Co	K line	19.16	0.19157	45.75	1.38	Co
Ni	K line	6.19	0.06193	14.30	1.47	Ni
Total:				100.00		

g
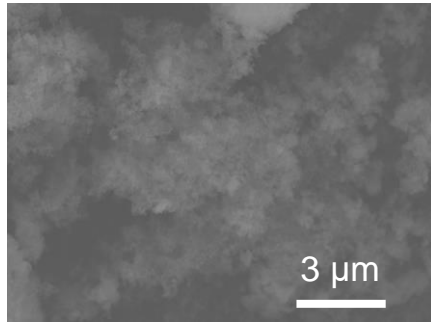
h
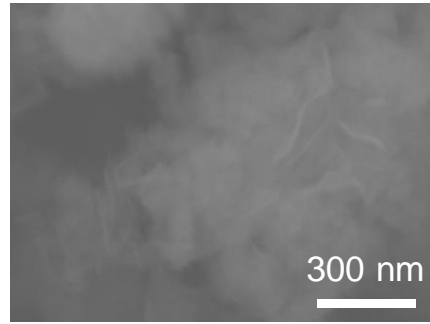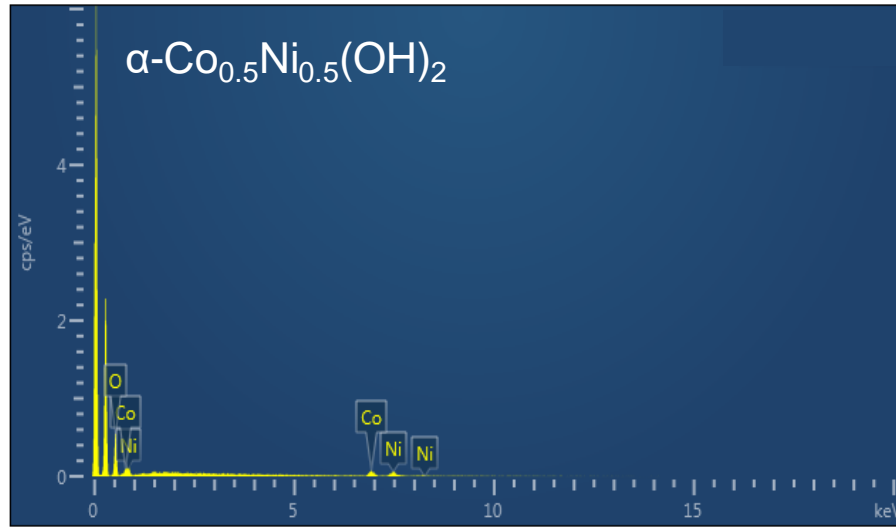
3 µm

300 nm

i

α-$Co_{0.5}Ni_{0.5}(OH)_2$

Elements	Line Type	Apparent concentration	k ratio	wt%	wt% Sigma	Standard sample label
O	K line	21.28	0.07162	38.42	1.64	SiO_2
Co	K line	10.14	0.10145	31.36	1.92	Co
Ni	K line	10.11	0.10111	30.22	2.13	Ni
Total:				100.00		
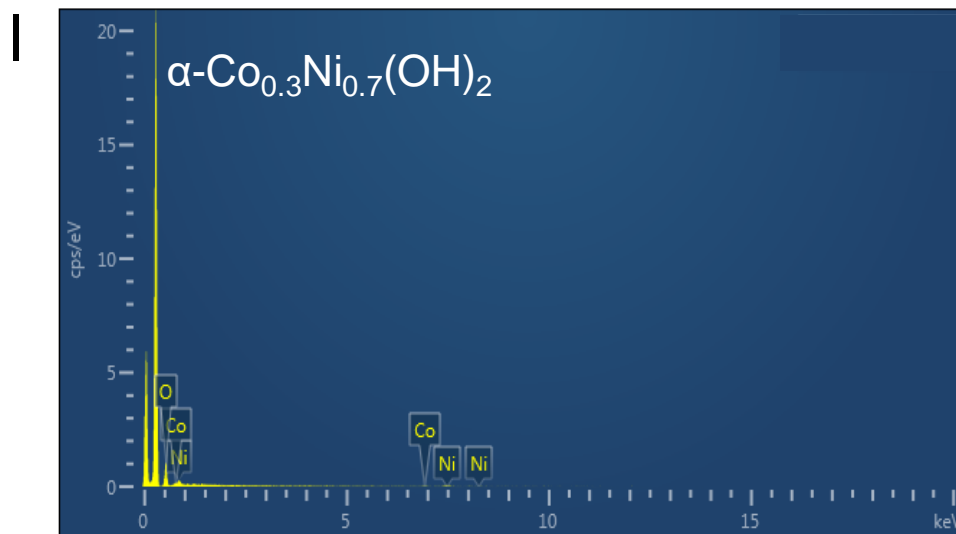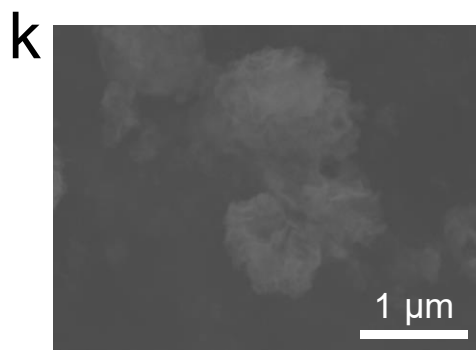
j

k

2 µm

1 µm

l

$\alpha\text{-Co}_{0.3}\text{Ni}_{0.7}(\text{OH})_2$

Elements	Line Type	Apparent concentration	k ratio	wt%	wt% Sigma	Standard sample label
O	K line	16.05	0.05401	66.33	4.17	SiO_2
Co	K line	1.10	0.01096	9.83	2.99	Co
Ni	K line	2.74	0.02741	23.84	4.06	Ni
Total:				100.00		
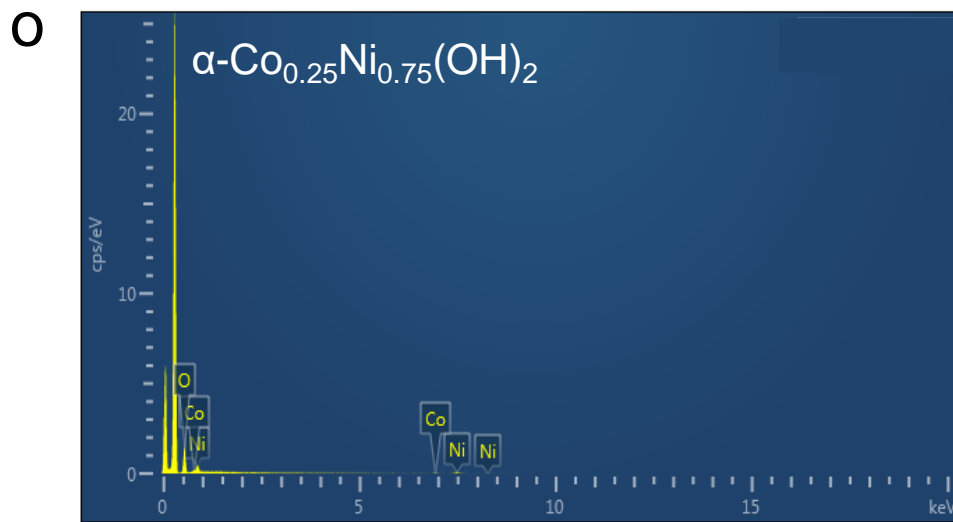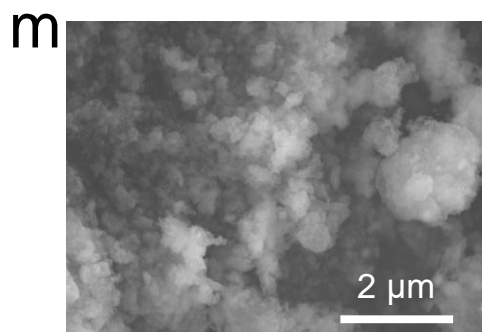
m

n

2 µm

500 nm

o

$\alpha\text{-}Co_{0.25}Ni_{0.75}(OH)_2$

Elements	Line Type	Apparent concentration	k ratio	wt%	wt% Sigma	Standard sample label
O	K line	18.70	0.06294	67.67	2.87	SiO_2
Co	K line	0.98	0.00983	7.80	1.99	Co
Ni	K line	3.19	0.03188	24.52	2.75	Ni
Total:				100.00		
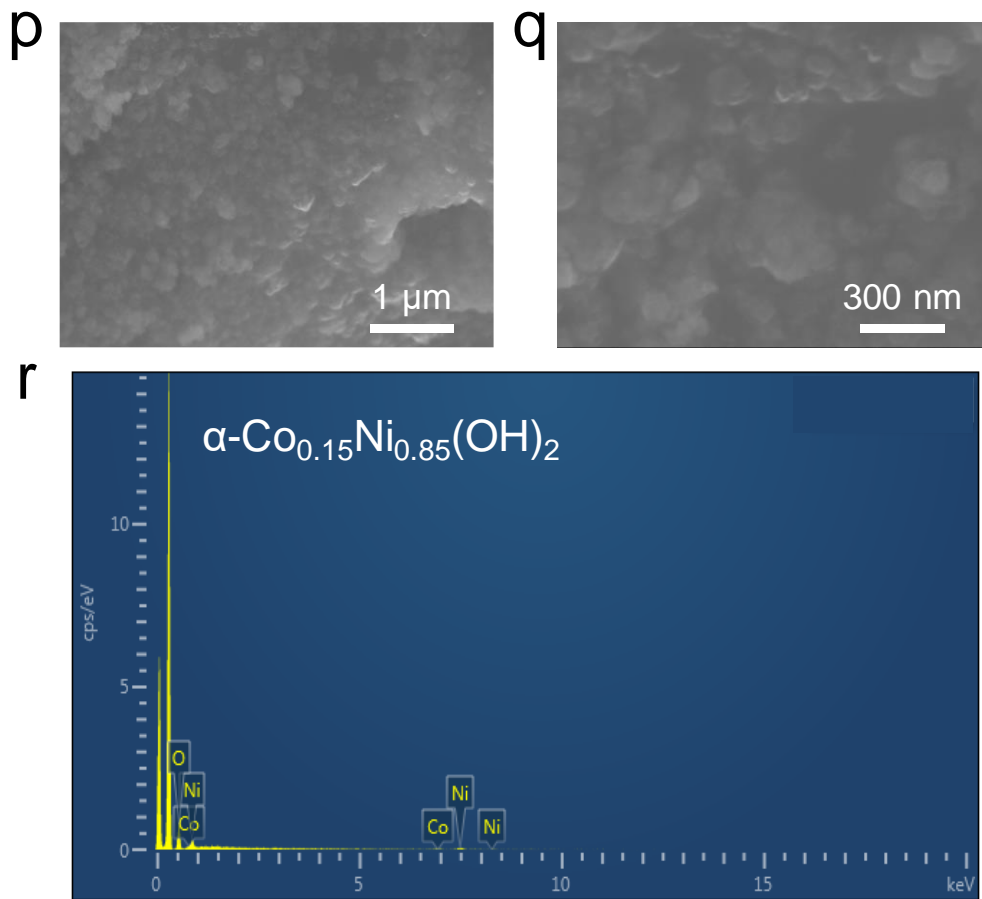
p

q

1 μm

300 nm

r

$\alpha\text{-}Co_{0.15}Ni_{0.85}(OH)_2$

Elements	Line Type	Apparent concentration	k ratio	wt%	wt% Sigma	Standard sample label
O	K line	15.45	0.05198	59.86	4.39	SiO_2
Co	K line	0.84	0.00838	6.57	3.48	Co
Ni	K line	4.42	0.04421	33.57	4.28	Ni
Total:				100.00		
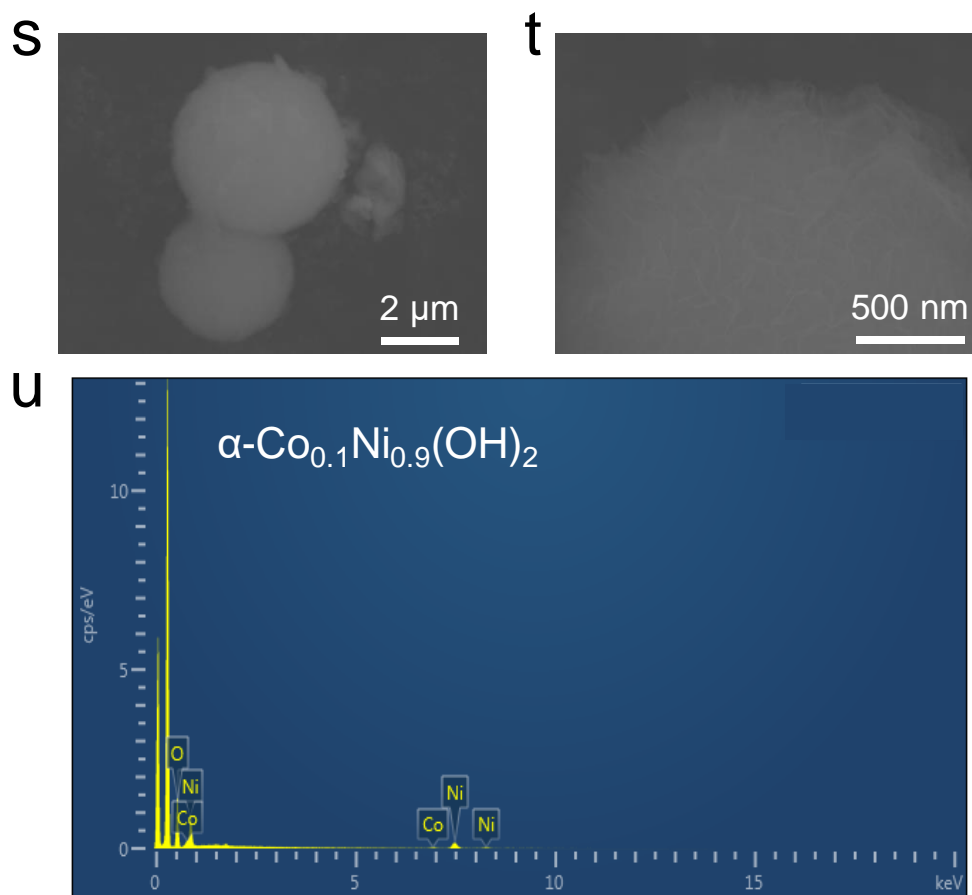
s

t

u

α-Co$_{0.1}$Ni$_{0.9}$(OH)$_2$

Elements	Line Type	Apparent concentration	k ratio	wt%	wt% Sigma	Standard sample label
O	K line	26.51	0.08923	48.11	0.96	SiO$_2$
Co	K line	1.29	0.01293	4.23	0.67	Co
Ni	K line	15.07	0.15067	47.66	1.00	Ni
Total:				100.00		

Supplementary Figure S8. The SEM images and elements distribution spectroscopy (EDS) analysis of a series of nickel doped cobalt hydroxides. (a-c) α-Co$_{0.9}$Ni$_{0.1}$(OH)$_2$, (d-f) α-Co$_{0.7}$Ni$_{0.3}$(OH)$_2$, (g-i) α-Co$_{0.5}$Ni$_{0.5}$(OH)$_2$, (j-l) α-Co$_{0.3}$Ni$_{0.7}$(OH)$_2$, (m-o) α-Co$_{0.25}$Ni$_{0.75}$(OH)$_2$, (p-r) α-Co$_{0.15}$Ni$_{0.85}$(OH)$_2$ and (s-u) α-Co$_{0.1}$Ni$_{0.9}$(OH)$_2$, it can be seen that the atomic ratios of Co and Ni calculated from the wt% agree well with the stoichiometric number.

The ICP-OES test results of the series of Co/Ni hydroxides were listed in **Supplementary Table S3** and **S4**.

Supplementary Table S3. The ICP-OES test results of the series of Co/Ni hydroxides (as prepared).

Catalysts	Mass (mg)	Co (mg/L)	Ni (mg/L)	Total (mg/L)	Co ratios (%)	Ni ratios (%)
α-$Co_{0.9}Ni_{0.1}(OH)_2$	5.14	46.6	5.68	52.28	**89.14**	**10.86**
α-$Co_{0.7}Ni_{0.3}(OH)_2$	5.06	33.7	16.1	49.80	**67.67**	**32.33**
α-$Co_{0.5}Ni_{0.5}(OH)_2$	5.20	24.0	26.6	50.60	**47.43**	**52.57**
α-$Co_{0.3}Ni_{0.7}(OH)_2$	5.21	13.8	37.3	51.10	**27.01**	**72.99**
α-$Co_{0.15}Ni_{0.85}(OH)_2$	4.99	6.32	41.1	47.42	**13.33**	**86.67**
α-$Co_{0.1}Ni_{0.9}(OH)_2$	5.12	4.81	50.50	55.31	**8.70**	**91.30**

The Co/Ni ratios match very well (less than 3% error) with the preset ratios during the metal salt solutions preparation.

Supplementary Table S4. The ICP-OES test results of the series of Co/Ni hydroxides (post electrolysis).

Catalysts	Co (mg/L)	Ni (mg/L)	Total (mg/L)	Co ratios (%)	Ni ratios (%)
α-$Co_{0.9}Ni_{0.1}(OH)_2$	10.1	1.16	11.26	**89.70**	**10.30**
α-$Co_{0.7}Ni_{0.3}(OH)_2$	6.46	2.92	9.38	**68.87**	**31.13**
α-$Co_{0.5}Ni_{0.5}(OH)_2$	4.48	4.68	9.16	**48.91**	**51.09**
α-$Co_{0.3}Ni_{0.7}(OH)_2$	1.74	4.38	6.12	**28.43**	**71.57**
α-$Co_{0.15}Ni_{0.85}(OH)_2$	2.74	17.0	19.74	**13.88**	**86.12**
α-$Co_{0.1}Ni_{0.9}(OH)_2$	2.48	23.5	25.98	**9.55**	**90.45**

The carbon papers after electrolysis were dissolved in dilute HCl for later ICP-OES tests. The Co/Ni ratios in the catalysts after long-term electrolysis stayed close to the as-prepared catalysts, indicating the excellent stability of Co/Ni hydroxides.

On-chip device fabrication procedures (Note 3)

Fabrication of the hydroxide devices. A free standing film was prepared by a co-solvent evaporation method.[2-5] Typically, the hydroxide suspensions in ethanol (4 mL, ~2.5 mg·mL-1) were mixed with DI water (6 mL) and n-butanol (2.5 mL). The suspension of hydroxides in mixed solvents was added drop by drop into a flask (about 9 cm in diameter) filled with DI water. A film of hydroxides was then formed on the water surface. In specific, a PMMA film was prepared by spin coating on the substrate (p++ silicon wafer with 300 nm thermal oxide) surface with pre-patterned Ti/Au electrodes (20/50 nm). E-beam lithography (EBL) was then used to open windows between electrodes on PMMA with desired patterns. The as-prepared films of hydroxides were then transferred onto the substrate surface. After the removal of PMMA template, hydroxides films were deposited on the device with desired patterns. To avoid electrochemical reactions on the metal electrodes, another layer of PMMA (electrochemically inert) was then deposited on the device with hydroxide film patterns and a smaller window that only exposes hydroxides was opened by EBL. The final device, with exposed hydroxides was used for on-chip electrochemistry and *in situ* electrical transport spectroscopy (ETS) measurements.

On-chip cyclic voltammetry (CV) and *in situ* electrical transport (ETS) measurements. A 2-channel (Source/Measure Unit) SMU (Keysight B2902A or Keithley 2612B) was used for the CV and ETS measurements.[3-6, 14, 15] The first SMU channel was used as a potentiostat to control the potential of source electrode as to the reference electrode (V_G), while collecting the current (I_G) through the counter electrode. An Ag/AgCl electrode (in 3.5 M KCl) and a platinum wire were used as reference and counter electrode, respectively. In a typical on-chip CV measurement, the scan rate is 5 mV·s^{-1}. The measured potential vs. $E_{\text{Ag/AgCl}}$ was converted to reverse hydrogen electrode potential (RHE) based on the Nernst equation, E_{RHE} = $E_{\text{vs. Ag/AgCl}}$ + 0.059 × pH + E^0, where E^0 = 0.2046 V at 298.15 K. The second SMU was used to supply a small bias voltage (50 mV) between drain and source electrodes and collecting the corresponding lateral transport current (I_{DS}).

Electrical conductivity calculations. The *in situ* electrical conductivity of on-chip devices were calculated by

$$\sigma = \frac{I_{\text{DS}} \cdot l}{V_{\text{DS}} \cdot w \cdot h \cdot N} \qquad (55)$$

where I_{DS} is the conductive current, l is the length of electrochemical window, w is the width of

electrochemical window, V_{DS} is the small bias voltage (50 mV) between drain and source electrodes, h is the average film thickness determined by AFM, and N is the number of devices connected in parallel.
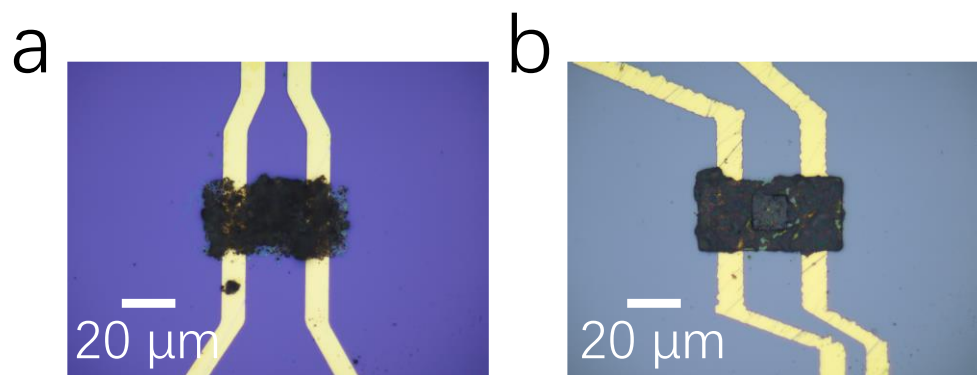
Supplementary Figure S9. The typical thin film devices for on-chip CV and *in situ* conductance (ETS) measurements.

Ag/AgCl reference electrode calibration
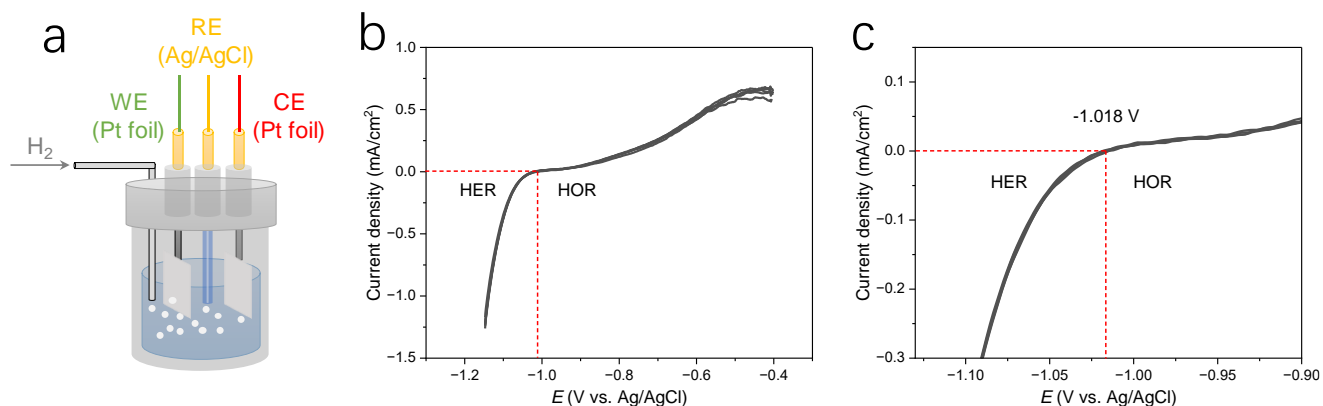
Supplementary Figure S10. Potential calibration of the Ag/AgCl reference electrode. (a) Schematic illustration for RE calibration. Pt foils were used as both the working electrode and counter electrode. (b) Cyclic voltammetry curves for Ag/AgCl electrode calibration in 1.0 M KOH (99.999%) solution. (c) Zoom-in of the (b). The CV tests were carried out after pumping high-purity hydrogen for 30 mins to saturate the electrolyte. HER, hydrogen evolution reaction, HOR, hydrogen oxidation reaction. All electrochemical data were presented without *iR*-correction. The size of carbon papers (C.P.) were 1×2 cm^2.

Note that all long-term electrolysis experiments used a Hg/HgO reference electrode, which is stable in alkaline solutions. We performed calibration tests in 1 M KOH (99.999%) following the method described in the literature.[16] We found that the potential of the Ag/AgCl electrode (1.018 V) is very close to the value calculated using the Nernst equation (0.059 × 13.8 + 0.2046 = 1.0188 V). Therefore, for relatively short-term *in situ* tests (100 ~ 200 s) such as ETS, FTacV, Raman and EIS characterization, the potential values calculated using the Nernst equation for the Ag/AgCl electrode are reliable.

In situ electrical transport measurements of the catalysts
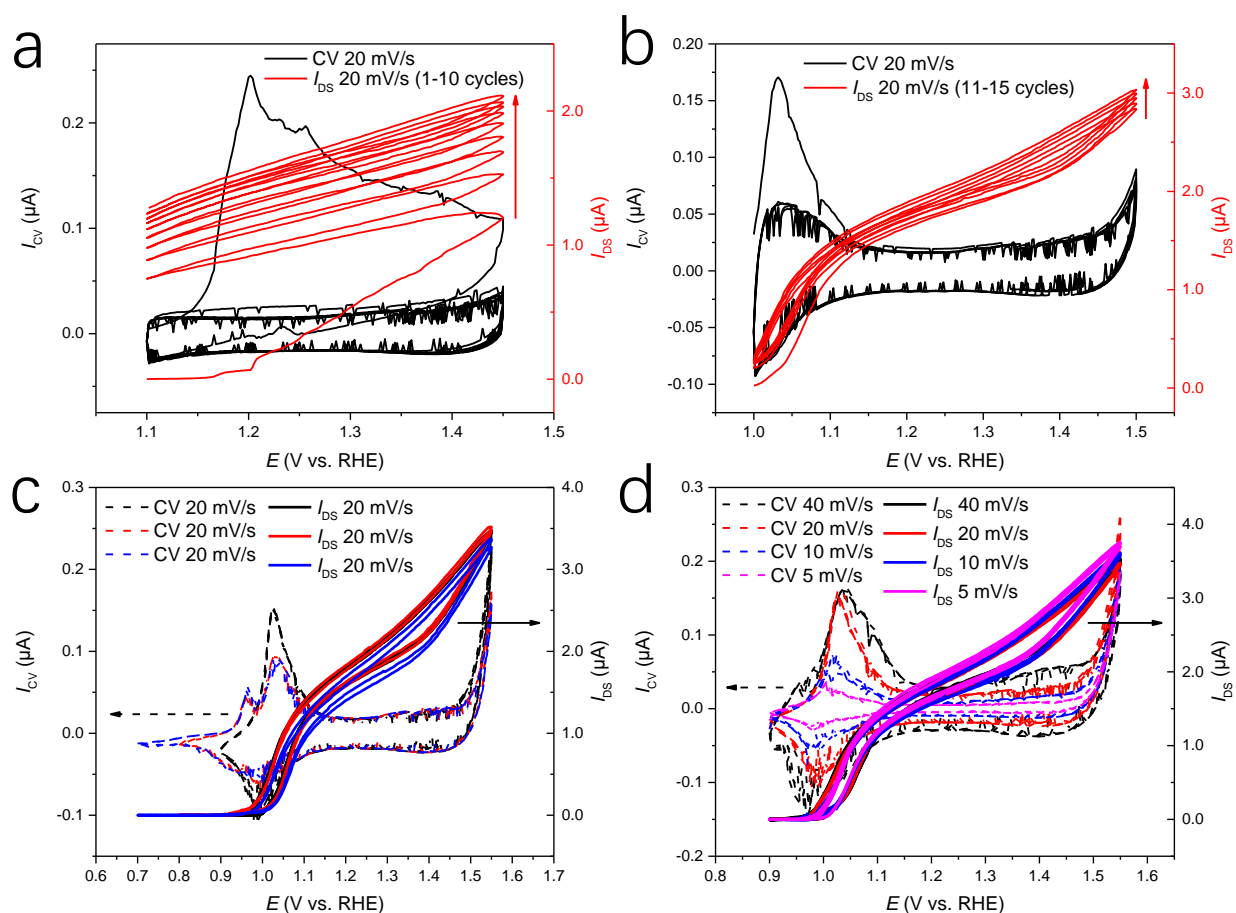
Supplementary Figure S11. The *in situ* electrical transport characterization (ETS) of α-Co(OH)$_2$. (a, b) The activation of the α-Co(OH)$_2$ thin film device during the electrochemical potential scan. (c, d) The comparison of different potential scan ranges (c) and scan rates (d) ETS results. The *in situ* conductance

currents stay relatively very stable after activation.
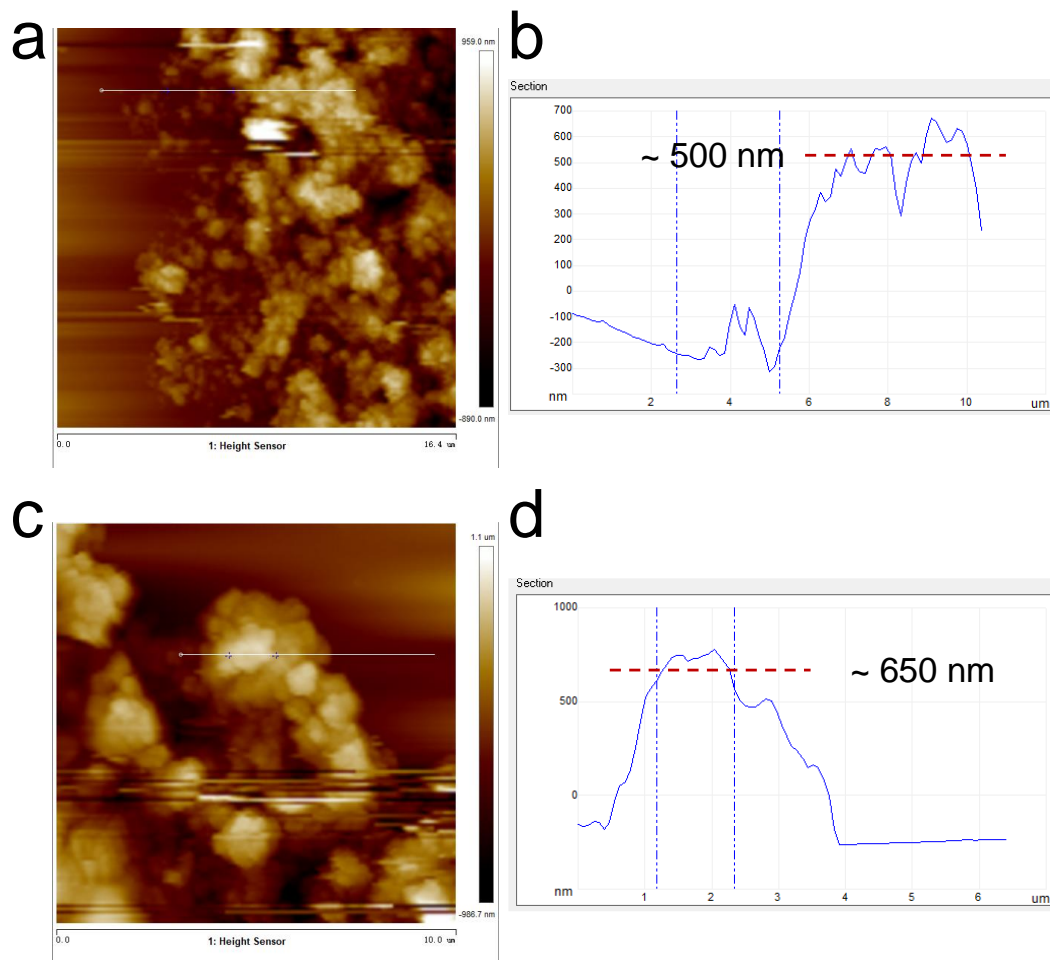
Supplementary Figure S12. The average height of the devices characterized by the atomic force microscopy (AFM) of α-Co(OH)$_2$ (a-b) and α-Co$_{0.5}$Ni$_{0.5}$(OH)$_2$ (c-d) catalysts thin films.
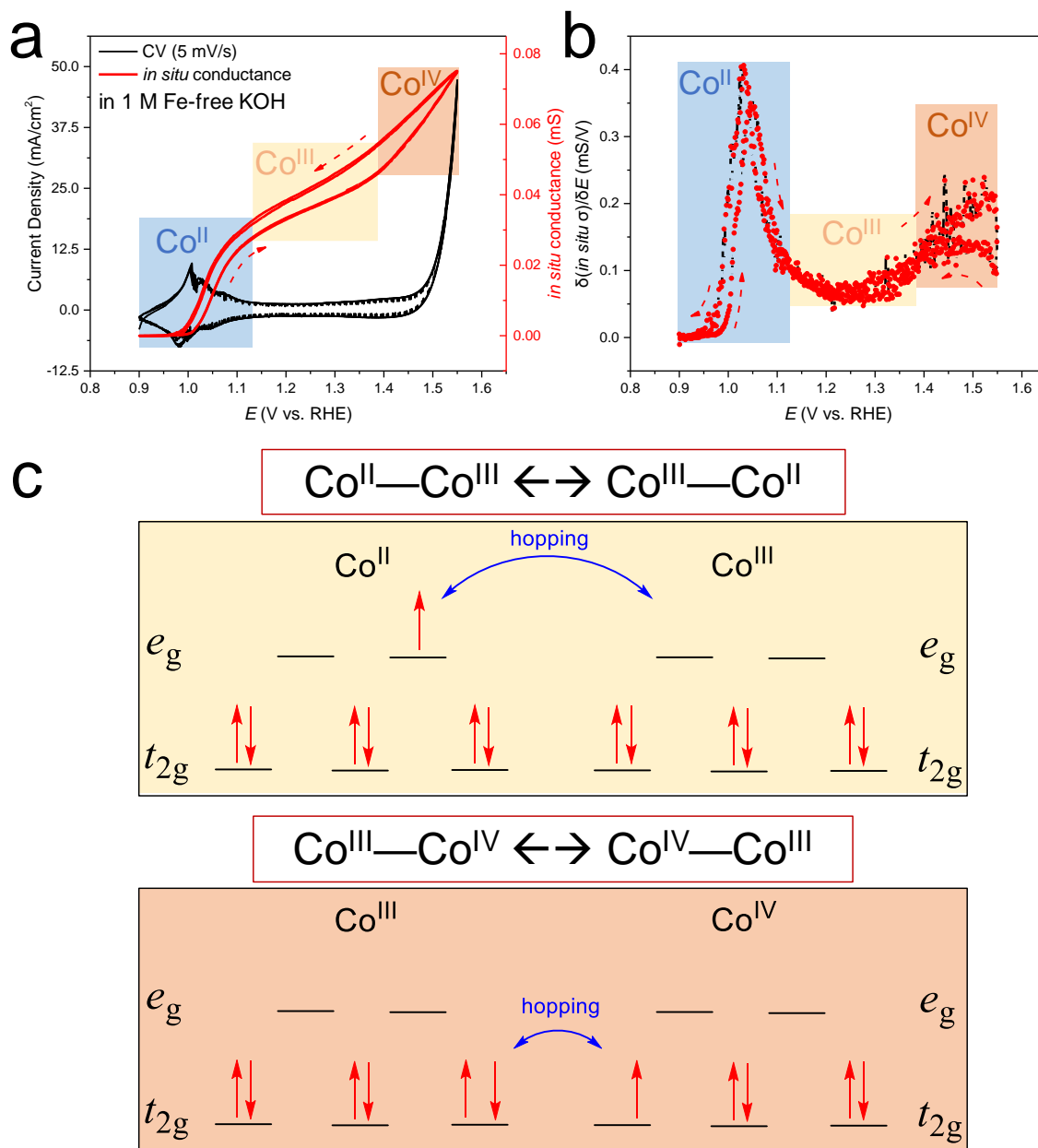
Supplementary Figure S13. The *in situ* electrical transport characterization (ETS) of α-Co(OH)$_2$. (a) The typical ETS signals of the α-Co(OH)$_2$ thin film device concurrent with the electrochemical potential scan. (b) The differential ETS signals derived from red curves in (a), where the three regions are related with oxidation of Co^{II}−H$_2$O*, formation of Co^{III}−OH* species and formation of high-valent OER related Co^{IV}−O*/OOH* active species. (c) The proposed "double exchange" interaction in the lattice of Co oxyhydroxides according to the previous work.[6]
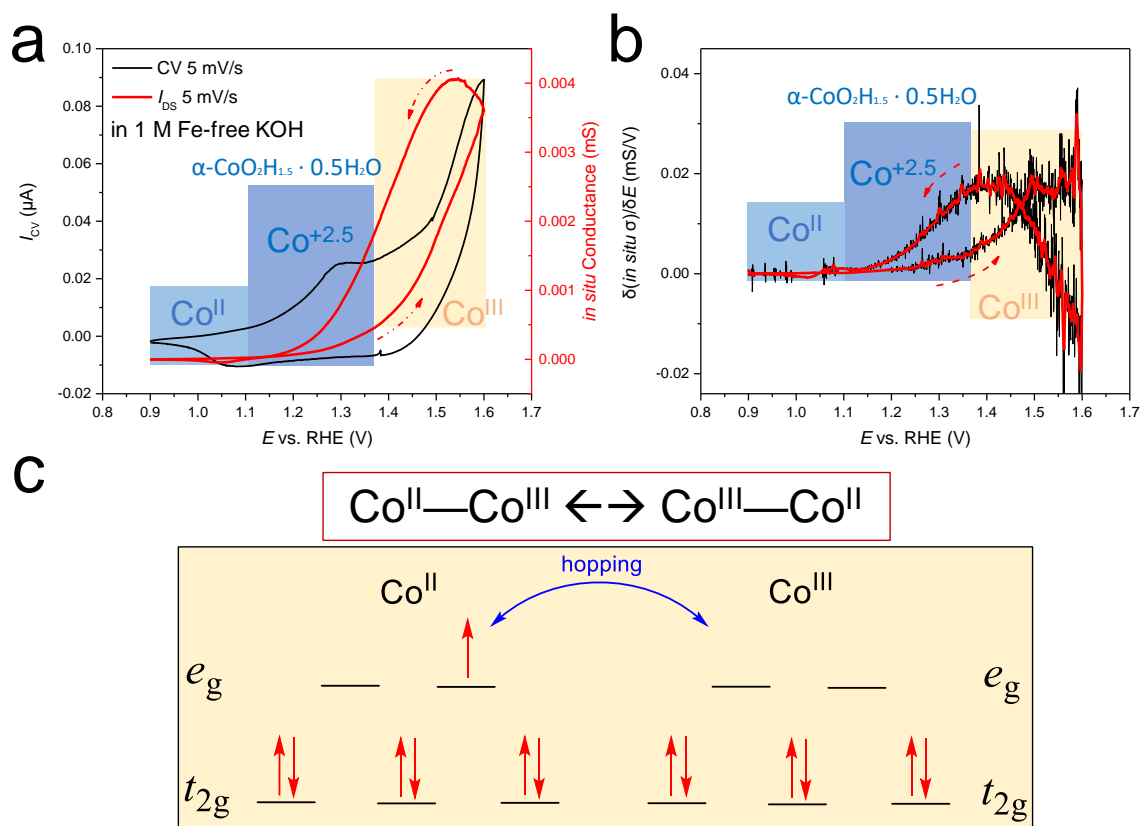
Supplementary Figure S14. The *in situ* electrical transport characterization (ETS) of β-Co(OH)$_2$. (a) The typical ETS signals of the β-Co(OH)$_2$ thin film device concurrent with the CV, which is much lower than that of α-Co(OH)$_2$. (b) The differential ETS signals derived from red curves in a, where the three regions are related with oxidation of Co^{II}–H$_2$O*, formation of Co$^{+2.5}$–OH* species[17] and formation of OER related Co^{III}–OH* active species. (c) The proposed "double exchange" interaction in the lattice of Co oxyhydroxides according to the previous work.[6]
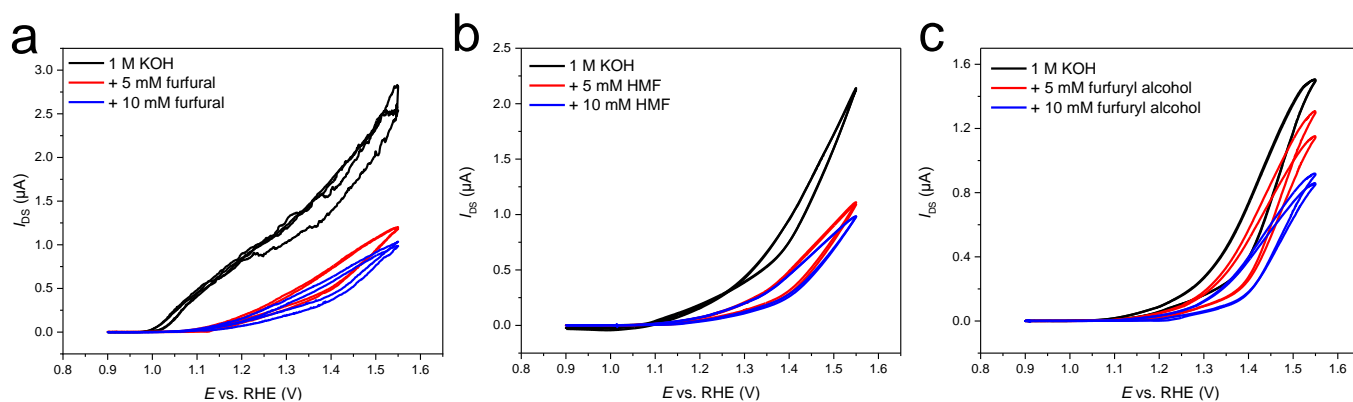
Supplementary Figure S15. The typical *in situ* electrical transport characterization (ETS) measurement results of α-Co(OH)$_2$ thin film devices in 1 M Fe-free KOH and the addition of 5 mM and 10 mM organic substrates for (a) furfural, (b) HMF and (c) furfuryl alcohol.
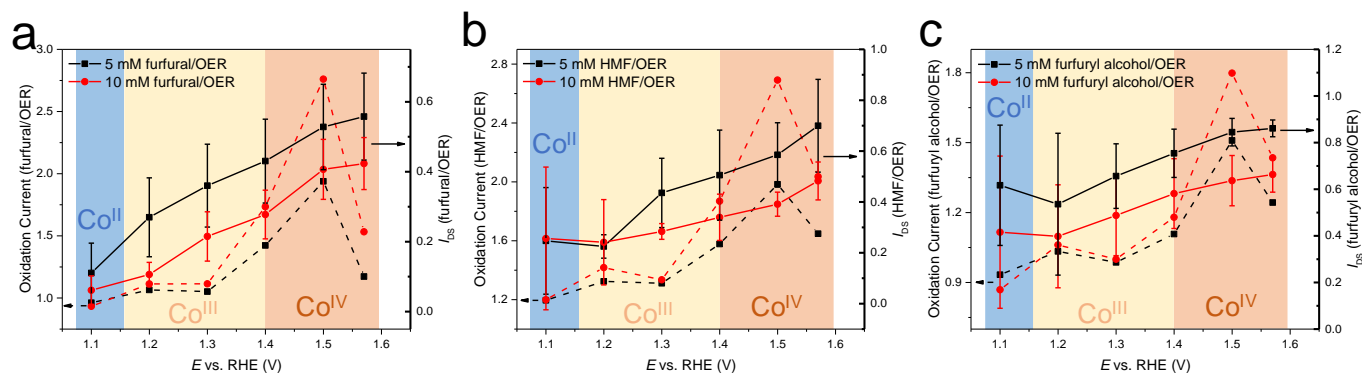

Supplementary Figure S16. The statistical ratios of the measured *in situ* transport current I_{DS} in 1 M Fe-free KOH and the addition of 5 mM and 10 mM organic substrates for (a) furfural, (b) HMF and (c) furfuryl alcohol. The error bars are derived from three independent measurements with 3 thin film devices for each substrate. The bulk CV curves are used to calculate the ratios of electrochemical oxidation current (symbols in dashed lines) for better accuracy.

# Comparison of OER and electro-oxidation activities by d.c. CV
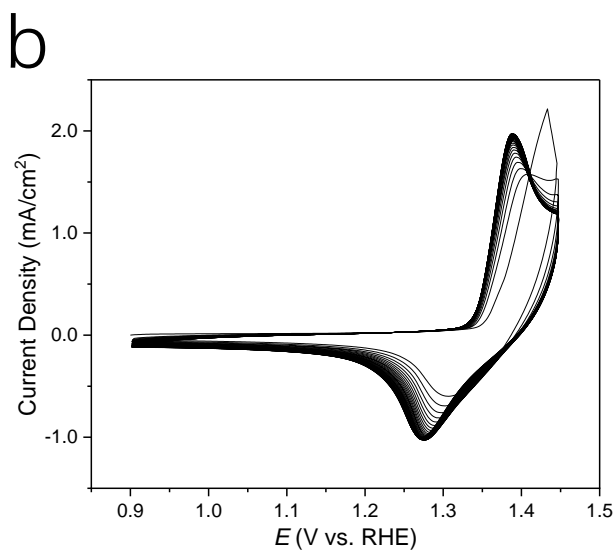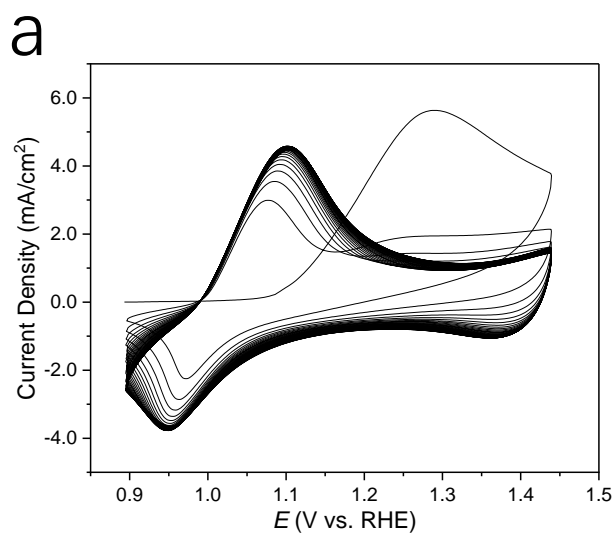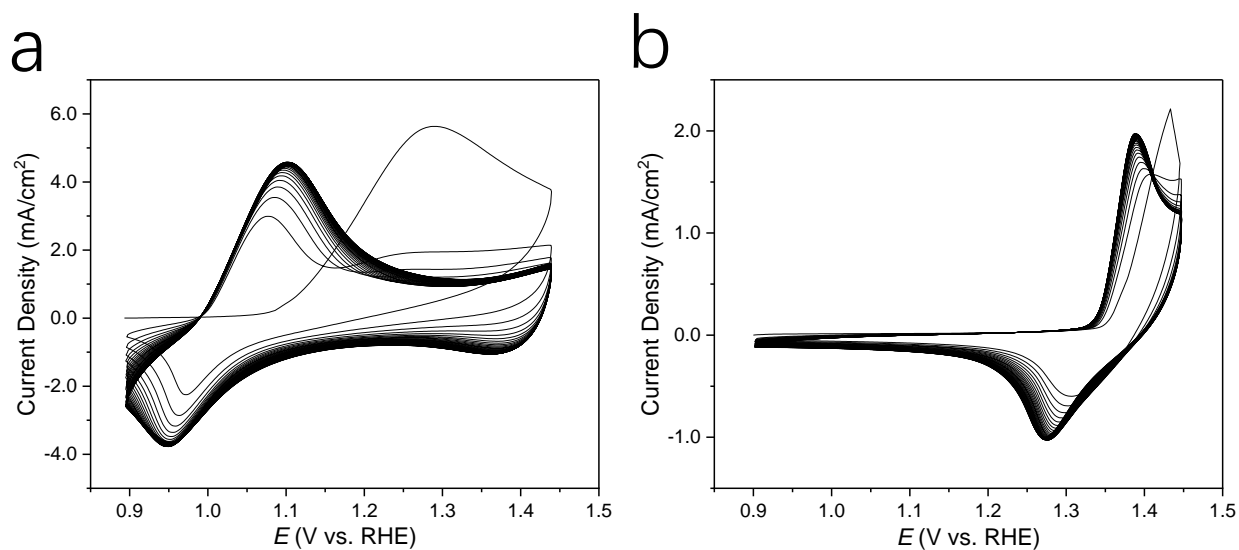
Supplementary Figure S17. The d.c. CV activation of α-Co(OH)$_2$ (a) and α-Ni(OH)$_2$ (b) in the range of 0.9 V ~ 1.45 V *vs*. RHE (100 mV/s) to achieve a steady surface state. All electrochemical data were presented without *iR*-correction. The size of carbon papers (C.P.) were 1×2 cm^2.
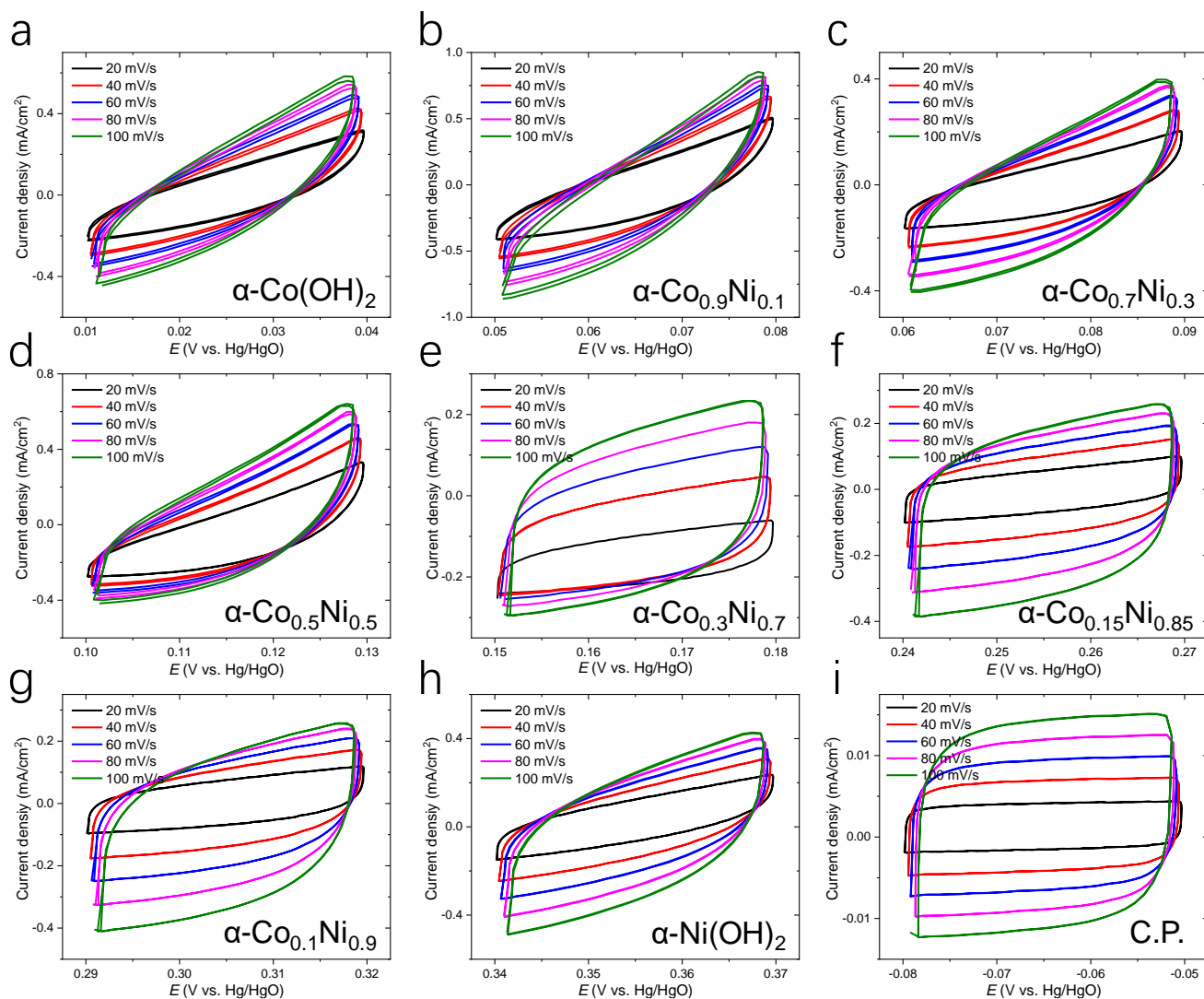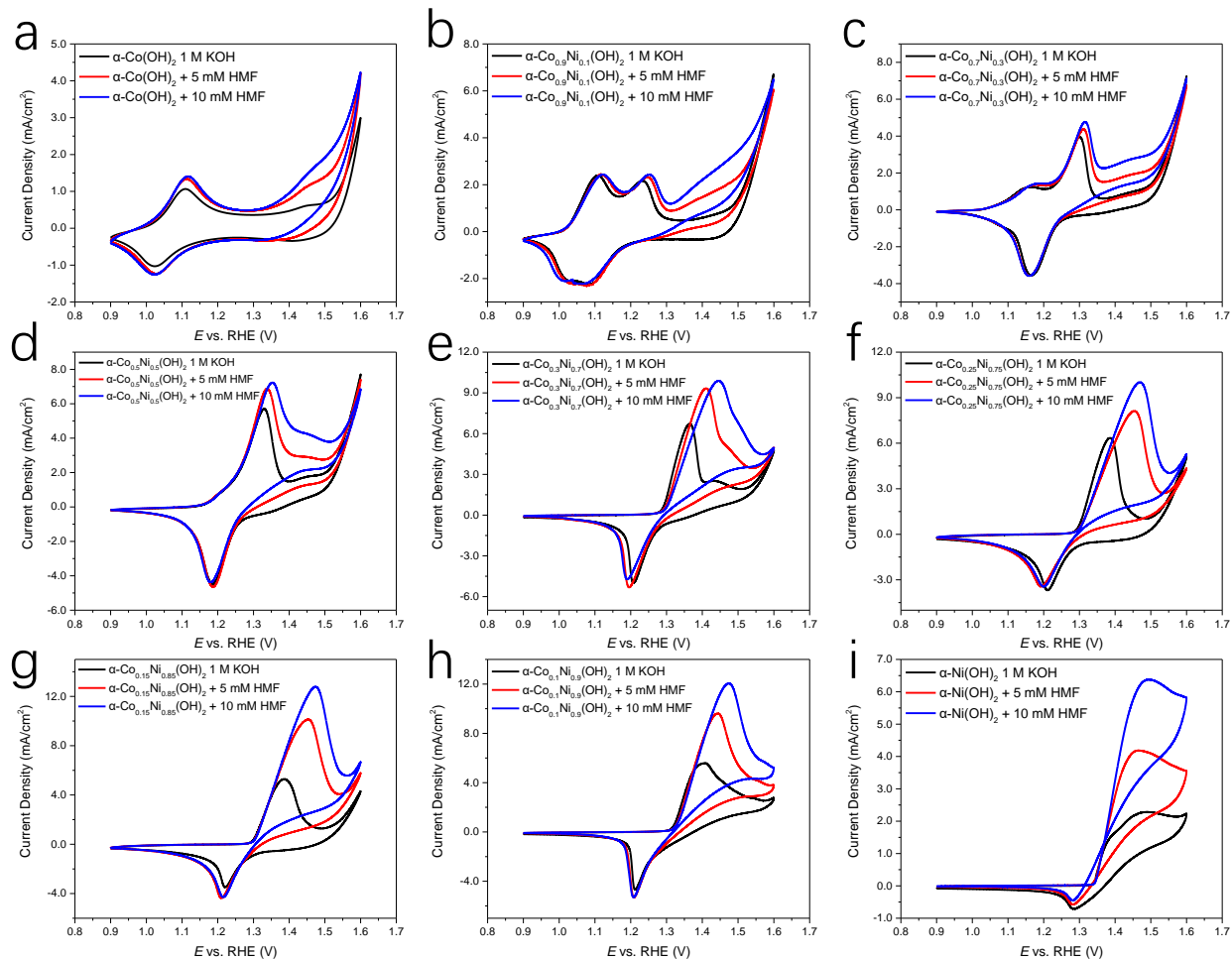

Supplementary Figure S18. The electrochemical active surface area (ECSA) measurements for different α-Co$_x$Ni$_{1-x}$(OH)$_2$ ($x = 0$~1) (a-h) and blank carbon paper (i).
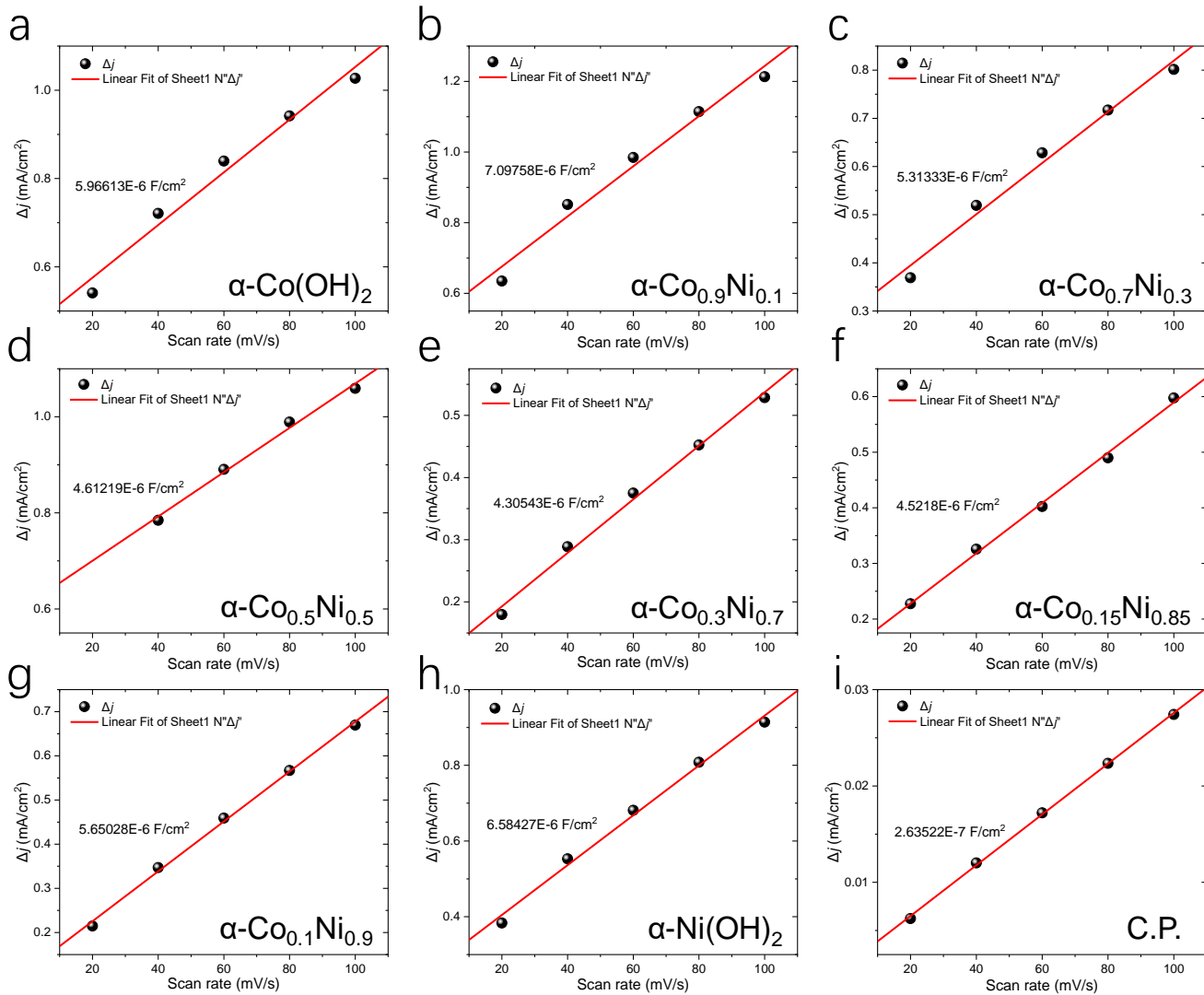
**Supplementary Figure S19**. The linear fitting results and the fitted slopes for ECSA calibration.
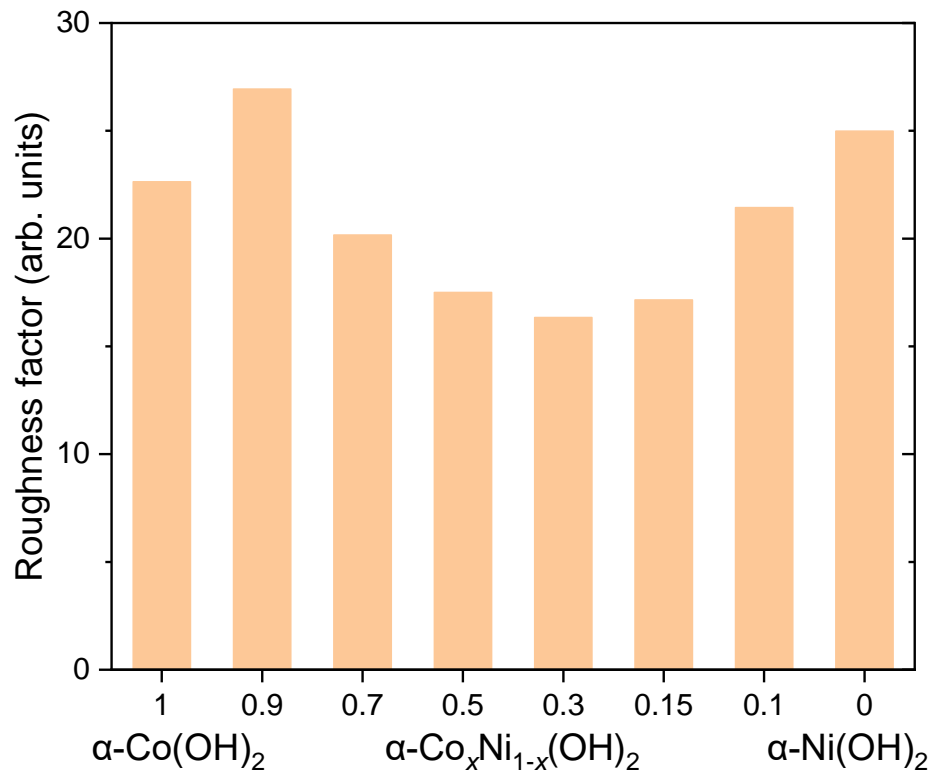
Supplementary Figure S20. The roughness factors of different α-Co$_x$Ni$_{1-x}$(OH)$_2$ (x = 0~1), defined as ECSA$_{\text{catalyst}}$/ECSA$_{\text{blank carbon paper}}$.

Supplementary Figure S21. The measured CV curves of pure α-Co(OH)₂, α-Ni(OH)₂ and a series of nickel doped α-Co(OH)₂ hydroxides in 1 M Fe-free KOH and the addition of 5 mM and 10 mM HMF. All electrochemical data were presented without *iR*-correction. The size of carbon papers (C.P.) were 1 × 2 cm².
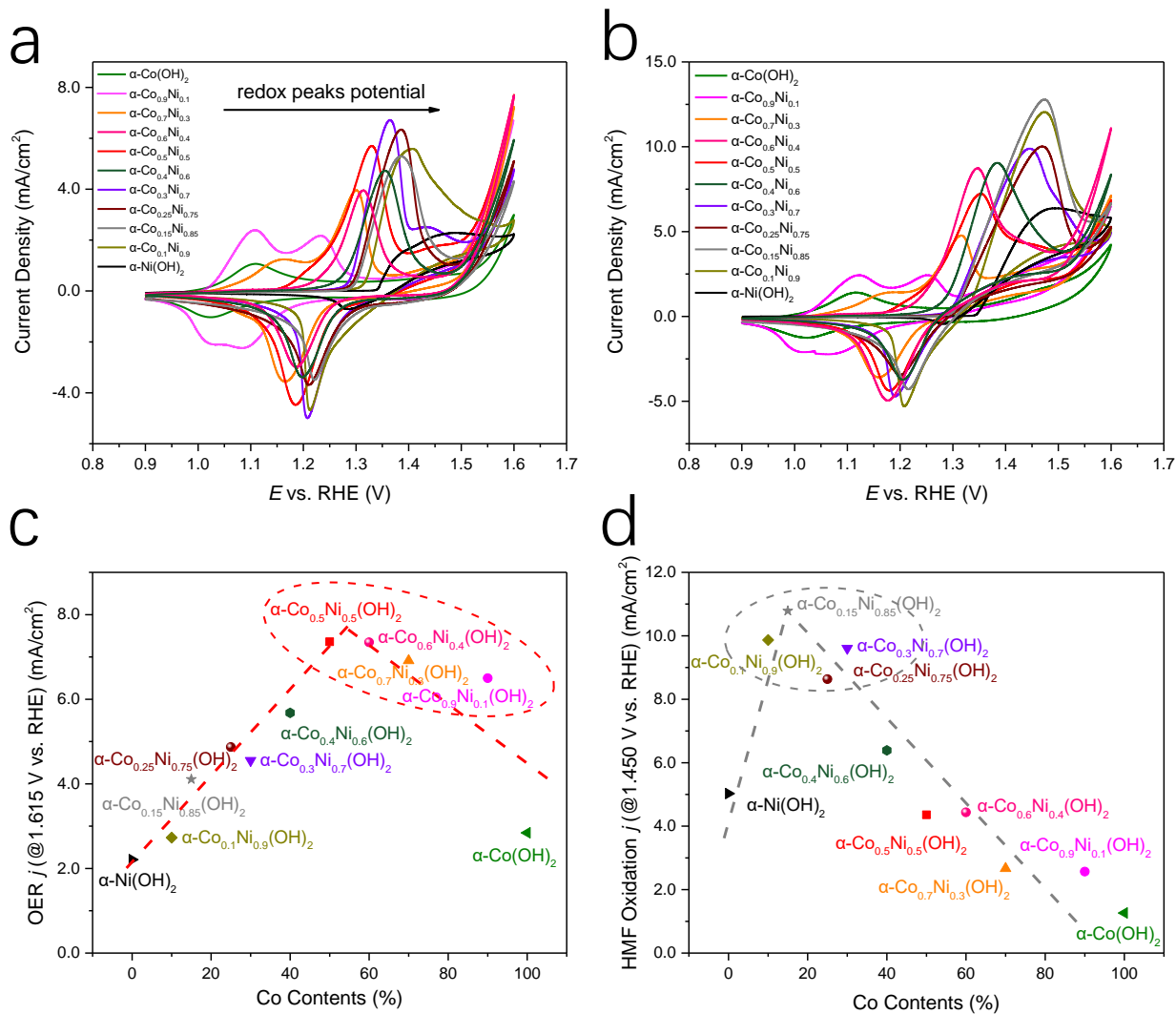
Supplementary Figure S22. (a, b) The summarized CV curves of pure α-Co(OH)₂, α-Ni(OH)₂ and a series of nickel doped α-Co(OH)₂ hydroxides in the conditions of OER and EOOR. It can be seen that the redox peak potentials of the catalysts gradually move to higher potential with lower concentration of cobalt. There are both volcano shape relationships in OER and EOOR activity *vs.* Co contents plots (c, d). All electrochemical data were presented without *iR*-correction. The size of carbon papers (C.P.) were 1 × 2 cm².
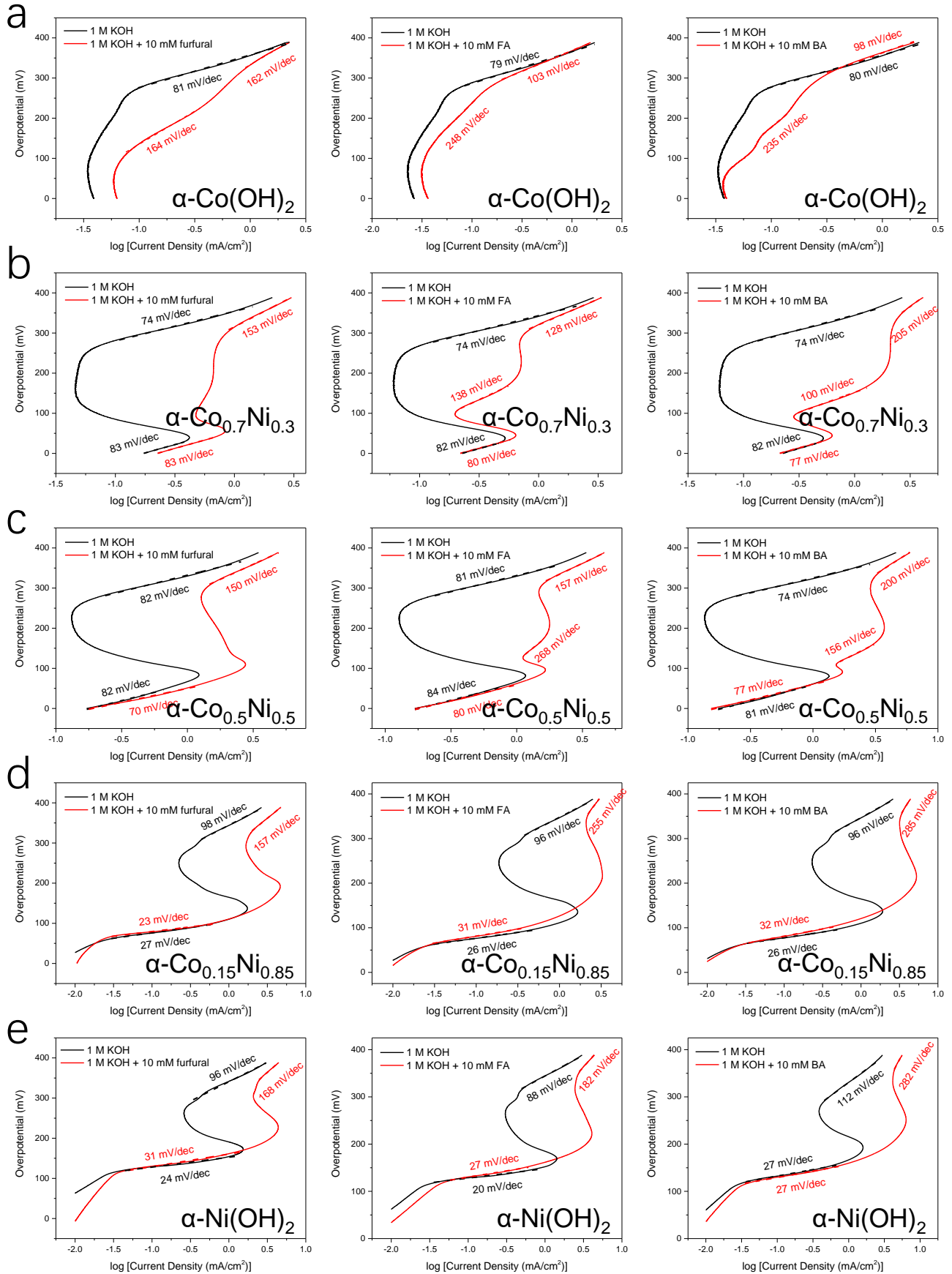
Supplementary Figure S23. The OER-relevant Tafel slope analysis of a series of nickel doped cobalt hydroxides α-Co$_x$Ni$_{1-x}$(OH)$_2$ (x = 0~1) under the condition of OER and electro-oxidation of different organic substrates. Note that the OER-relevant Tafel slopes are derived from kinetic Tafel region at the potential range of 1.5−1.6 V$_{RHE}$, where the OER electro-dynamics are dominant, i.e., FE$_{OER}$ > 80%, which is determined by the HPLC and GC analysis of products.
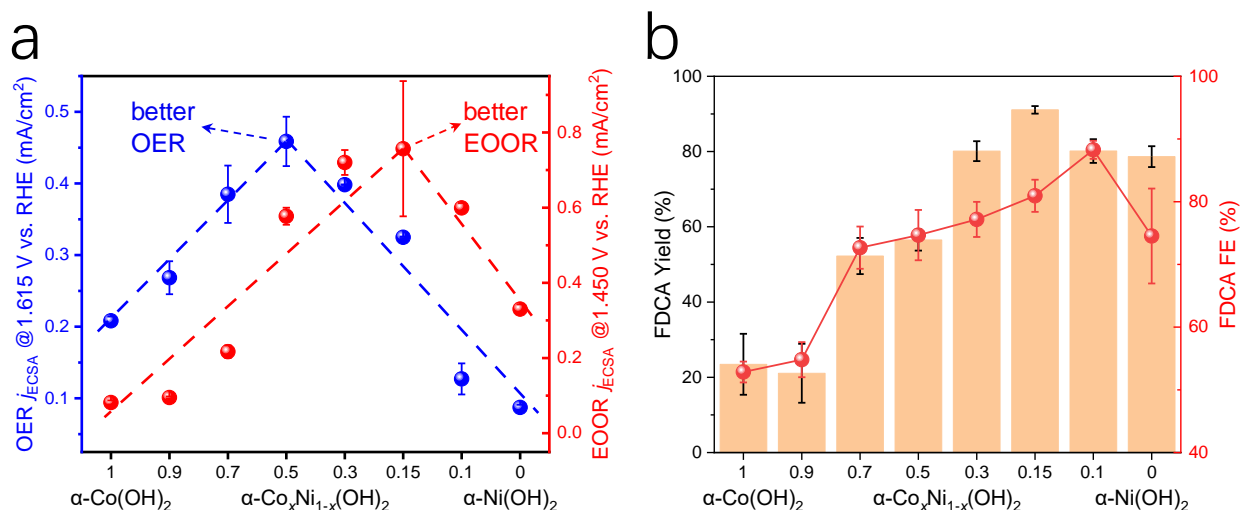
Supplementary Figure S24. The comparisons of OER and EOOR catalytic activities of different α-Co$_x$Ni$_{1-x}$(OH)$_2$ (x = 0~1). (a) The current densities of OER (@1.615 V$_{RHE}$) and EOOR (@1.450 V$_{RHE}$) of different α-Co$_x$Ni$_{1-x}$(OH)$_2$ (x = 0~1), where two sets of volcano-like correlations can be observed. (b) The yield and FE of FDCA products in bulk electrolysis. Note that the catalyst with the highest yield is consistent with the EOOR activity vertex in (a). Error bars were obtained from three independent experiments.
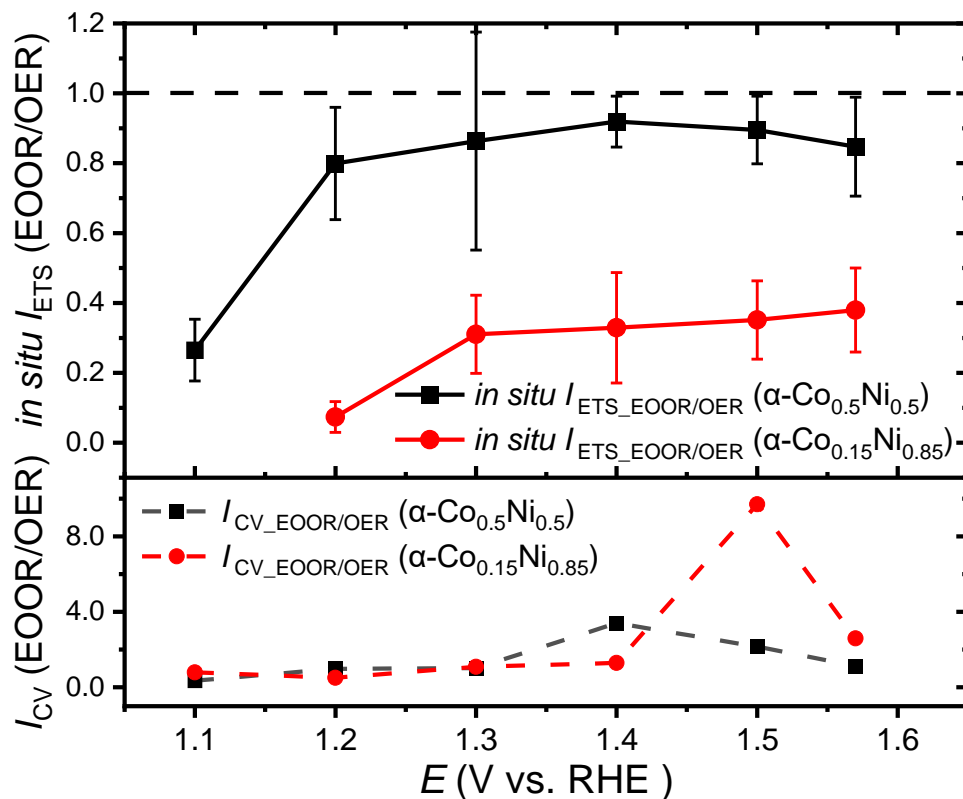
Supplementary Figure S25. The ETS (upper part) and CV (bottom part) signal ratios between EOOR and OER conditions of representative α-Co$_{0.5}$Ni$_{0.5}$(OH)$_2$ and α-Co$_{0.15}$Ni$_{0.85}$(OH)$_2$. Error bars were obtained from three independent experiments.

To better reveal and quantify the key *operando* surface intermediates resulting from OER and EOOR on α-Co$_x$Ni$_{1-x}$(OH)$_2$, we conducted further *in situ* ETS measurements for α-Co$_{0.5}$Ni$_{0.5}$(OH)$_2$ and α-Co$_{0.15}$Ni$_{0.85}$(OH)$_2$ (located at two vertexes in **Figure 2d**), representing the best OER and EOOR catalyst, respectively. The ratio of *in situ* conductance under EOOR and OER conditions (I_{ETS_EOOR}/I_{ETS_OER}, averaged from three different measurements) were utilized to represent the surface M$^{3+\delta}$−OH* (Co^{3+}−OH* at low potentials and Co^{4+}/Ni$^{3+/4+}$−OH* at high potentials) relative variation from OER to EOOR, from which we found the I_{ETS_EOOR}/I_{ETS_OER} and I_{CV_EOOR}/I_{CV_OER} could be divided into three potential ranges:

i) At the low potential region (1.10−1.20 V$_{RHE}$), both α-Co$_{0.5}$Ni$_{0.5}$(OH)$_2$ and α-Co$_{0.15}$Ni$_{0.85}$(OH)$_2$ exhibit almost identical CV (~1.0) and a low I_{ETS_EOOR}/I_{ETS_OER} ratio (~0.20), indicating that these two structures have similar initial inert surface states before their oxidation processes.

ii) At higher potentials reaching the onset of Co/Ni oxidations toward high valence (+3 for Co and +3/+4 for Ni) state (1.20−1.40 V$_{RHE}$), the I_{CV_EOOR}/I_{CV_OER} still remain low (~1.0) as no obvious

EOOR occurs, while the OER-initiated surface oxygenated species ($M^{3+}-OH^*$) start to accumulate, as indicated by the increased I_{ETS_EOOR}/I_{ETS_OER} ratios.

iii)   With the further increase of the applied potentials (up to $1.40-1.57\ V_{RHE}$), the occurrence of EOOR is reflected in the dramatically increased I_{CV_EOOR}/I_{CV_OER}. Simultaneously, the competitive surface co-adsorptions of organic substances and oxygenated species reach a relatively steady state, as indicated by the relatively stable I_{ETS_EOOR}/I_{ETS_OER} ratios, as shown in Figure S18. Overall:

- the α-Co$_{0.5}$Ni$_{0.5}$(OH)$_2$ with higher *in situ* conductance ratio (I_{ETS_EOOR}/I_{ETS_OER} ~0.80) exhibits better OER activity,

- while the α-Co$_{0.15}$Ni$_{0.85}$(OH)$_2$ with generally lower ratio (I_{ETS_EOOR}/I_{ETS_OER} ~0.40) exhibits better EOOR catalytic performance, during which the majority of $M^{4+}-OH^*/O^*$ species are consumed for organic oxidation (at actual electrocatalytic potential of ~1.42 V_{RHE}).

This characteristic $M^{4+}-OH^*$-function correlation provides an effective parameter for catalyst design toward optimal OER or EOOR performance. Different I_{ETS_EOOR}/I_{ETS_OER} ratios are also observed from organic molecules with varying functional groups (furfural, HFM, and furfuryl alcohol). As revealed by the comparison in **Supplementary Figure S16** and **Supplementary Figure S25**, we conclude that co-adsorption of organics and oxygenate species generally exist in electro-oxidation processes assisted by water oxidation, and that the surface coverage of aldehyde tends to be higher compared to -CH$_2$OH.

In situ Raman spectroscopy of Co/Ni hydroxides
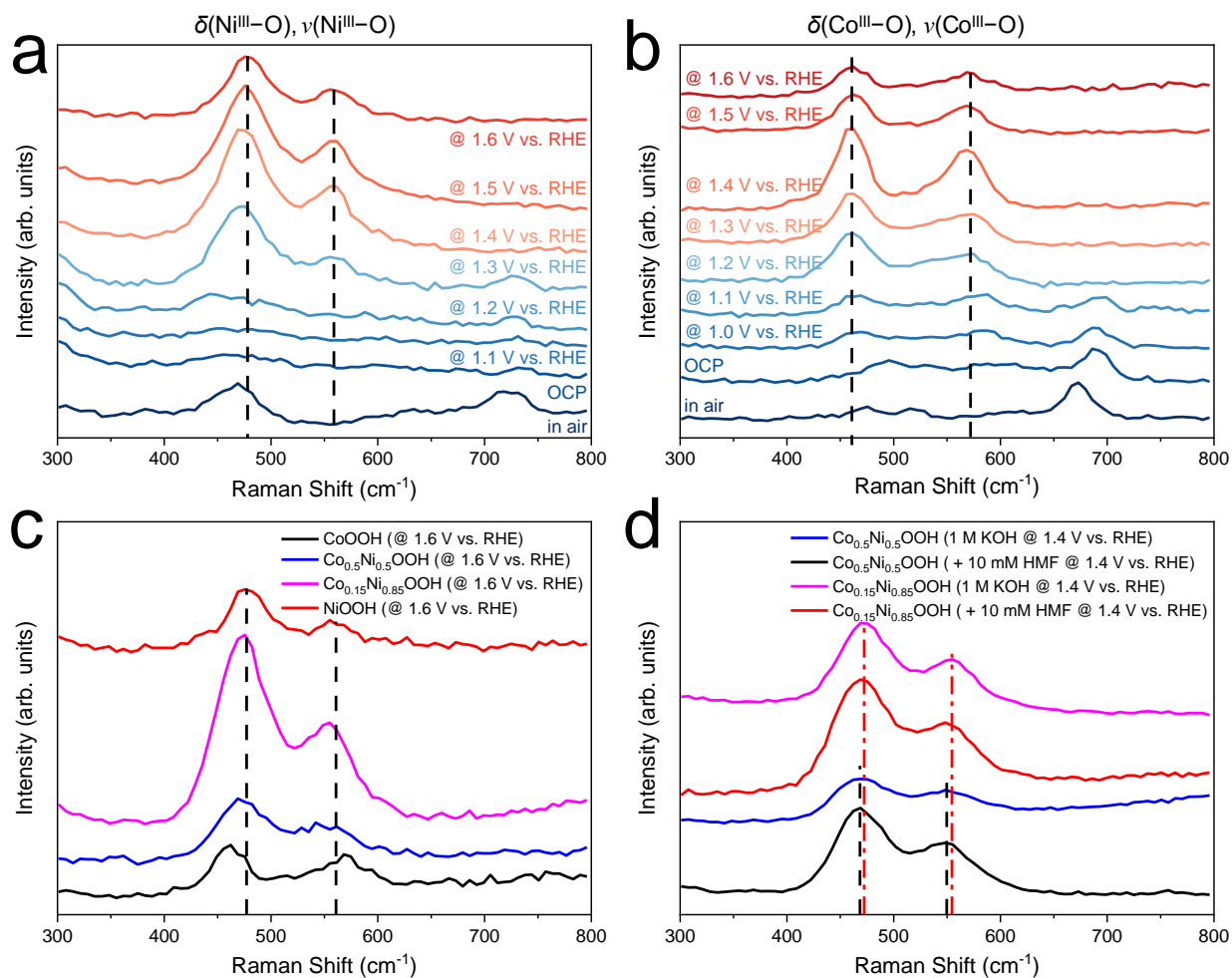
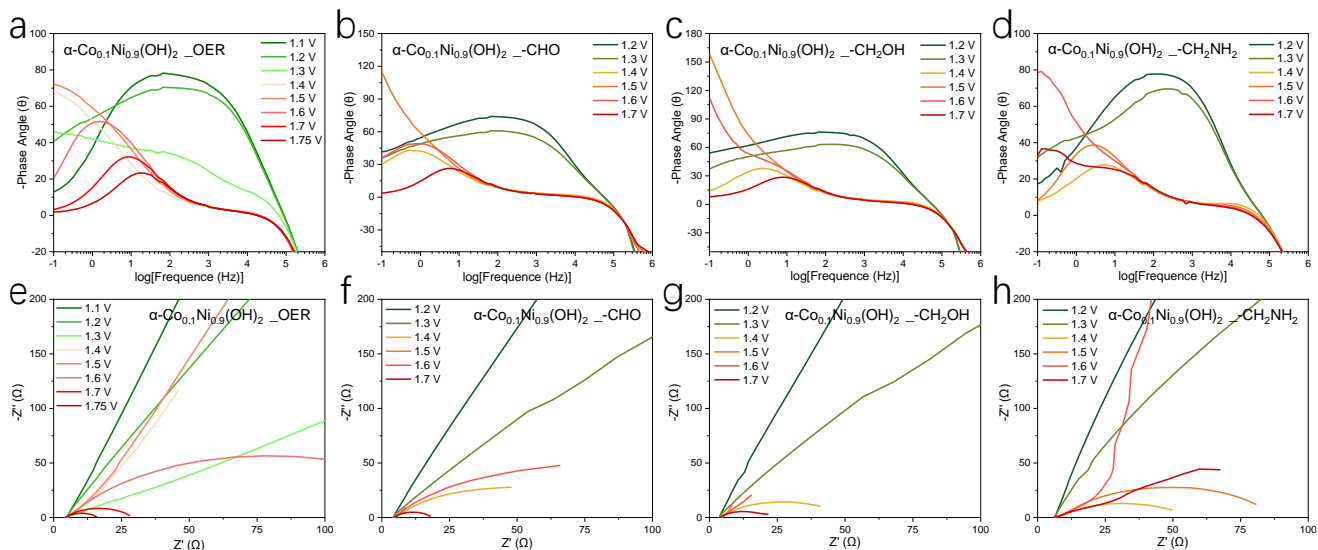**Supplementary Figure S26**. The *in situ* Raman spectroscopy of pure α-Ni(OH)$_2$ (a) and α-Co(OH)$_2$ (b) in 1 M Fe-free KOH. (c) The comparison of *in situ* Raman shift of four catalysts @1.60 V vs. RHE in 1 M Fe-free KOH. (d) The comparison of *in situ* Raman shift of α-Co$_{0.5}$Ni$_{0.5}$(OH)$_2$ and α-Co$_{0.15}$Ni$_{0.85}$(OH)$_2$ @1.40 V *vs*. RHE with and without addition of 10 mM HMF.
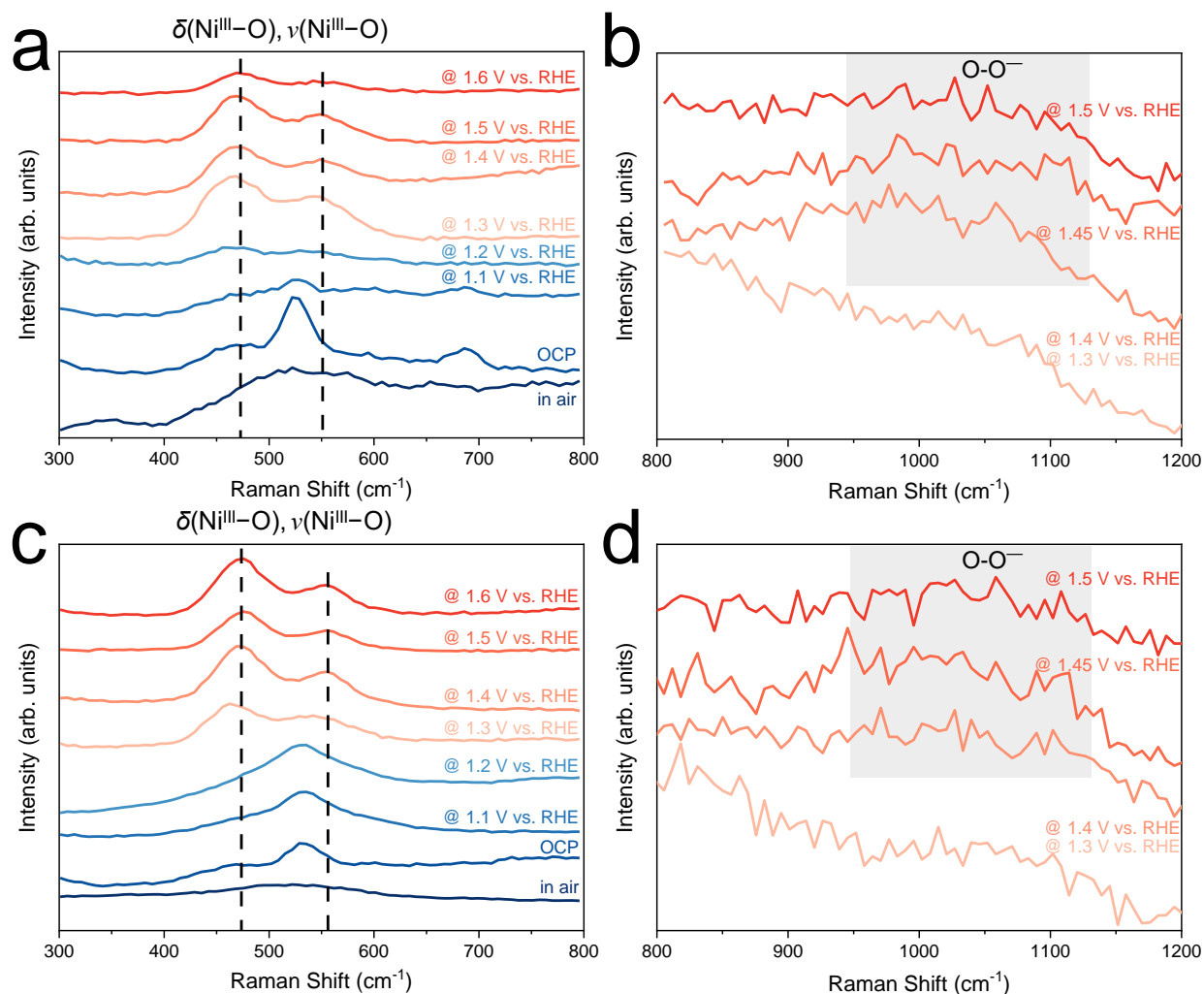
Supplementary Figure S27. The *in situ* Raman spectroscopy of α-$Co_{0.5}Ni_{0.5}(OH)_2$ (a, b) and α-$Co_{0.15}Ni_{0.85}(OH)_2$ (c, d) in 1 M Fe-free KOH. The electrochemical potential driven phase transition (vibrational peaks at 475 cm⁻¹ and 550 cm⁻¹) appears at higher potential when the nickel concentration increases.

In situ electrochemical impedance spectroscopy (EIS) of Co/Ni hydroxides

Supplementary Figure S28. The *in situ* EIS measurements of typical α-Co$_{0.1}$Ni$_{0.9}$(OH)$_2$ in the conditions of OER and electro-oxidation reactions. (a-d) The Bode plots. (e-h) The Nyquist plots.
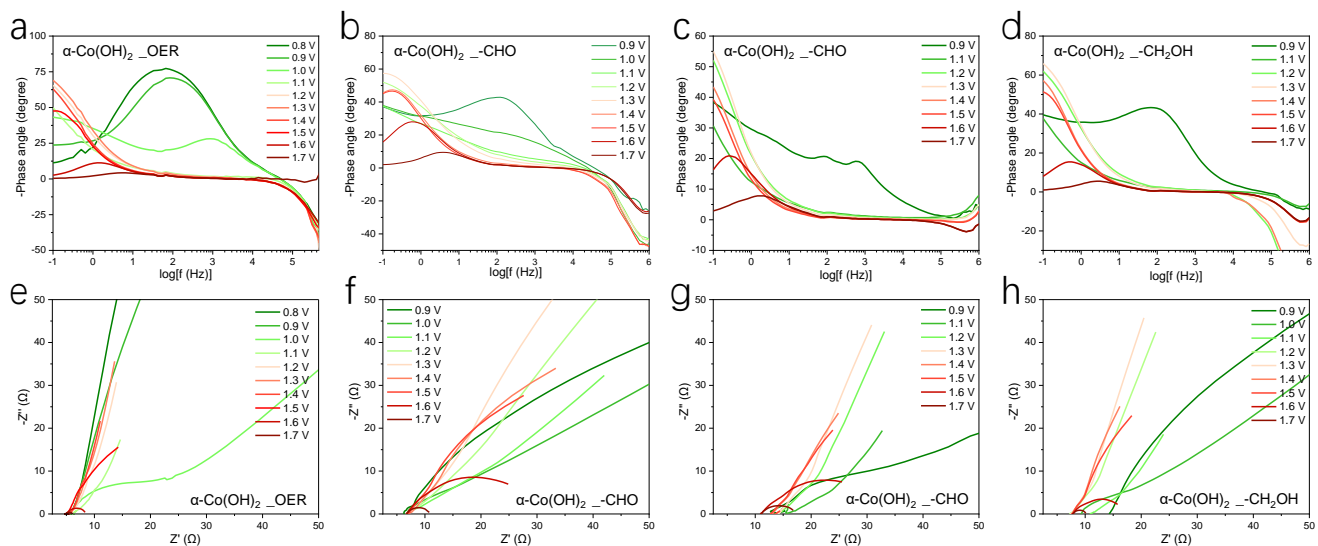
Supplementary Figure S29. The *in situ* EIS measurements of typical α-Co(OH)$_2$ in the conditions of OER and electro-oxidation reactions. (a-d) The Bode plots. (e-h) The Nyquist plots.
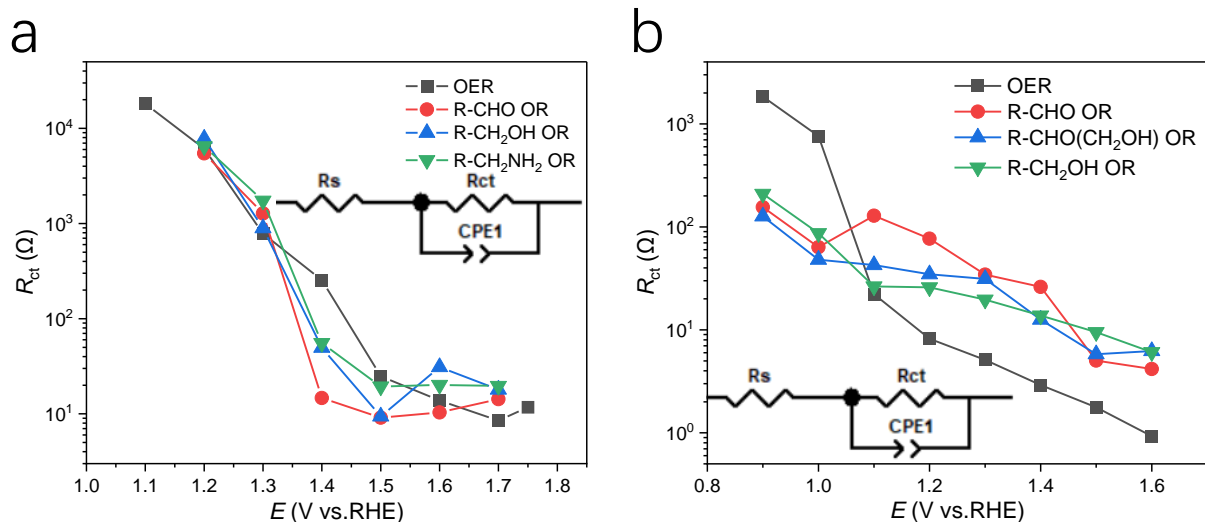
Supplementary Figure S30. Correlation of the charge transfer resistances (R_{ct}) and electrochemical potentials of α-Co$_{0.1}$Ni$_{0.9}$(OH)$_2$ (a) and α-Co(OH)$_2$ (b).

It can be observed that for optimal EOOR catalyst α-Co$_{0.1}$Ni$_{0.9}$(OH)$_2$, the R_{ct} value under OER conditions is relatively large at electrolysis potentials (1.4 ~ 1.5 V$_{RHE}$). In contrast, under the EOOR conditions with three different types of molecules, the R_{ct_EOOR} values are all smaller than R_{ct_OER}, with the order of R-CHO OR < R-CH$_2$OH OR < R-CH$_2$NH$_2$ OR. For α-Co(OH)$_2$ that tends to undergo OER pathway over EOOR (with the lowest EOOR yields and FEs) on the other hand, the R_{ct_EOOR} value at electrolysis potentials (1.4~1.5 V$_{RHE}$) is larger than R_{ct_OER}.

Detailed products analysis by HPLC and GC (Note 4)

High performance liquid chromatography (HPLC) measurements. HPLC (Agilent 1260) test was used to calculate the yield and Faradaic efficiency (FE) of the electro-oxidation products of furfuryl alcohol, furfural and HMF. The HPLC column is Agilent Eclipse XDB-C18 (5μm, 4.6 × 250 mm). To analyze the oxidation products of organics quantitatively and calculate the corresponding FE, 100 μL of the electrolyte solution was removed during electrolysis at 1.42 V (at a three-electrode cell) and diluted to 1 mL with ultra-pure water and analyzing it by HPLC. The specific parameters for furfural and furfuryl alcohol and theirs products are set as follows. The wavelength of the UV detector is set to 220 nm, mobile phase A was methanol and phase B was ultra-pure water, the ratio of A:B is 2:8 at controlled 20 ºC column

temperature, flow rate is 0.6 mL/min. The ultraviolet-visible detector was set at 265 nm for HMF and its products. A mixture of eluting solvents (A and C) was utilized. Solvent A was methanol and solvent C was 5 mM ammonium formate aqueous solution. Separation and quantification were accomplished using an isocratic elution of 30% A and 70% C for the oxidation of HMF at controlled 30 ℃ column temperature. The flow rate was set at 0.6 mL/min. The identification and quantification of the products were determined from the calibration curves by applying standard solutions with known concentrations of commercially purchased pure reactants, intermediates, and final products. The substrates conversion rate (%) and the corresponding product yield (%) were calculated using equations (Furoic acid (FCA), 2,5-furandicarboxylic acid (FDCA) and benzoic acid were quantified by HPLC):

$$\text{Substrate conversion rate}\,(\%) = \frac{n\,(\text{substrate consumed})}{n\,(\text{substrate initial})} \times 100\% \qquad (56)$$

$$\text{Products yield}\,(\%) = \frac{n\,(\text{product formed})}{n\,(\text{substrate initial})} \times 100\% \qquad (57)$$

Gas chromatography (GC) measurements. To analyze the oxidation products of benzyl amine quantitatively and calculate the corresponding FE, the total electrolyte solution was extracted with 20 mL ethyl acetate after electrolysis (at an undivided cell) and analyzing it by GC. Gas chromatography measurements were conducted on Shimadzu Nexis GC-2030 with a flame ionization detector and SH-Rtx-1 capillary column (30 m, 0.25 mm ID, 0.25 µm df) for quantitative analysis of benzonitrile. For quantitative analysis, the sample was injected for 3 times to get a mean value for one electrolysis. Dodecane was used as the internal standard to quantify benzonitrile. The temperature of the column was initially kept at 70 ℃ for 1 min and first increased to 150 ℃ at a rate of 10 ℃/min. Then the temperature was increased to 250 ℃ at a rate of 25 ℃/min and kept for 3 min. Dodecane was used as the internal standard to quantify the substrate and products. The conversion and the yields (benzonitrile and benzaldehyde were quantified by GC) were calculated as follows:

$$\text{Conversion rate}\,(\%) = \frac{1 - n\,(\text{moles of amine})}{n\,(\text{moles of amine loaded})} \times 100\% \qquad (58)$$

$$\text{Yield}\,(\%) = \frac{n\,(\text{moles of product})}{n\,(\text{initial moles of amine})} \times 100\% \qquad (59)$$

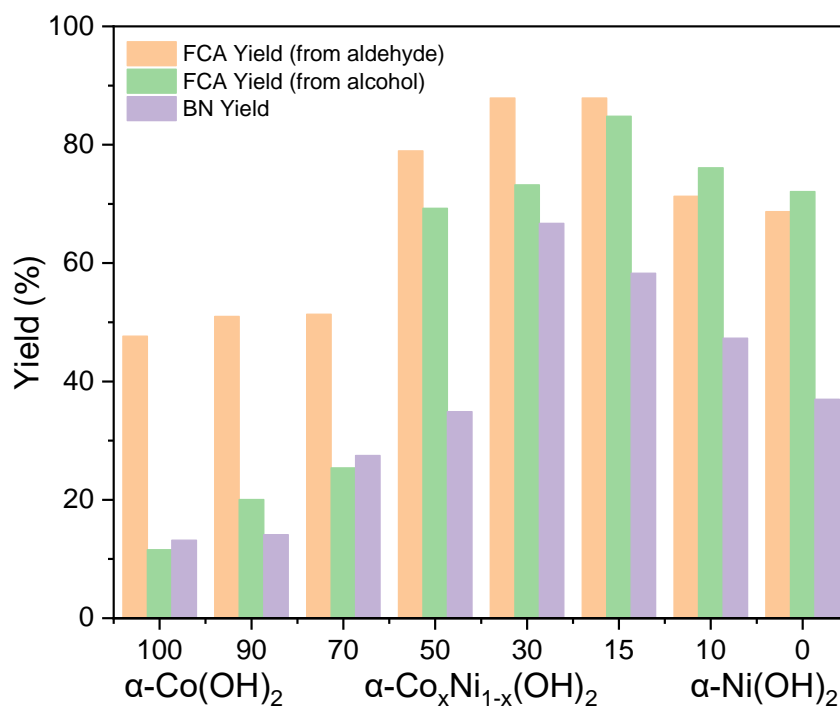The calibration curves used to quantitatively determine the products concentration and the yield can be found in **Supplementary Figure S31** and **Supplementary Figure S32**.
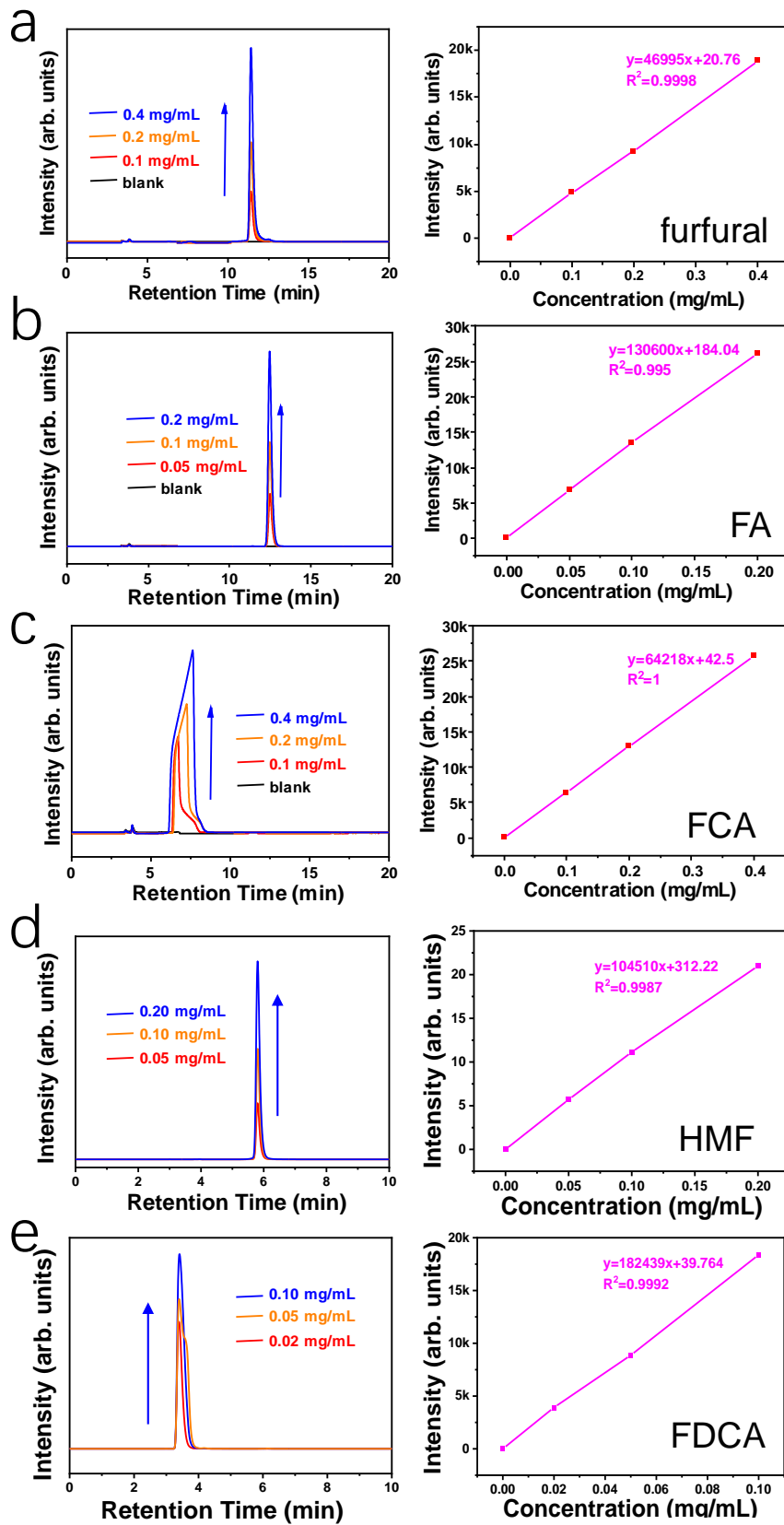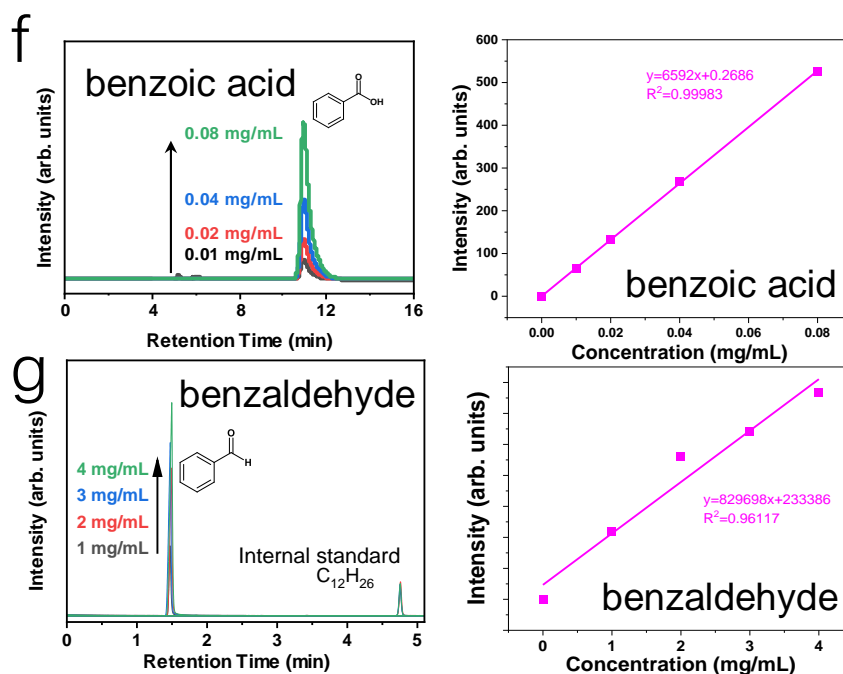
Supplementary Figure S31. The calibration curves used to quantitatively determine the products concentration.

Supplementary Figure S32. The electro-oxidation yields of 3 substrates catalyzed by a series of nickel doped cobalt hydroxides.
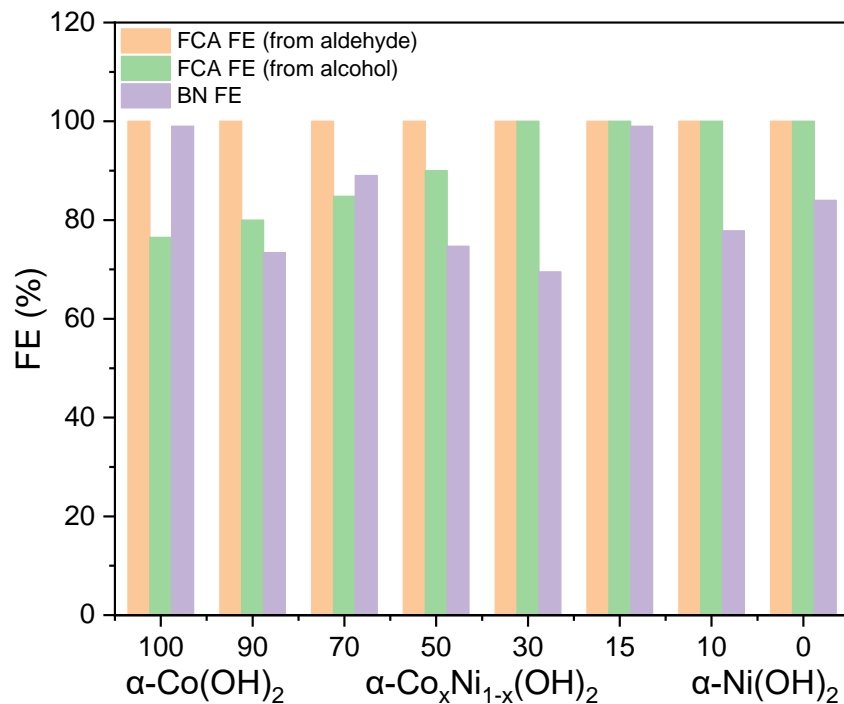
Supplementary Figure S33. The electro-oxidation FEs of 3 substrates catalyzed by a series of nickel doped cobalt hydroxides.
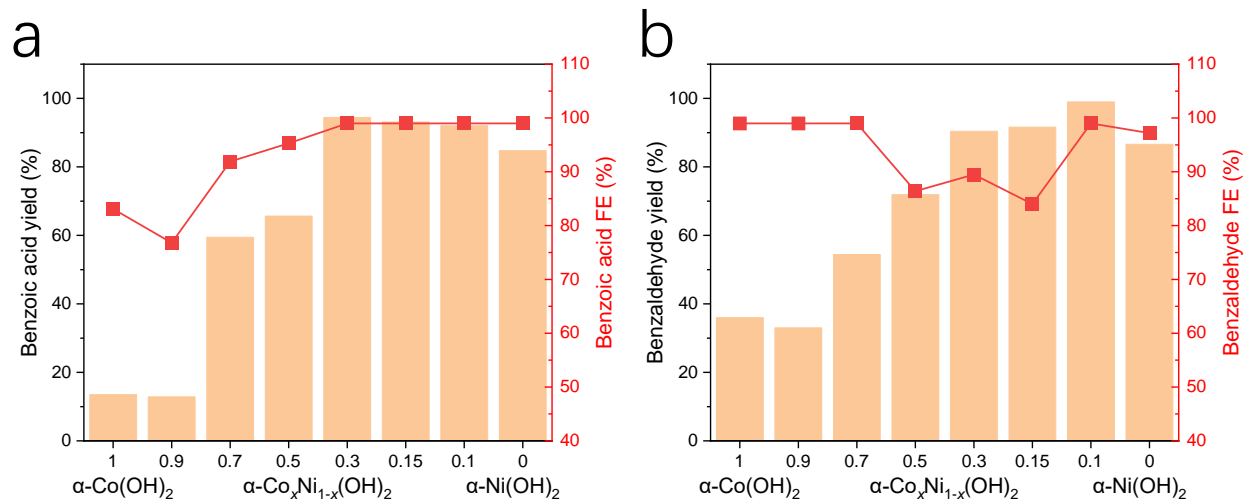
Supplementary Figure S34. The electro-oxidation yields and FEs of benzoic acid (a, in 1 M KOH) and the selective oxidation yields and FEs of benzaldehyde (b, in 1 M K_2CO_3) from benzyl alcohol.

Extracted FTacV harmonics
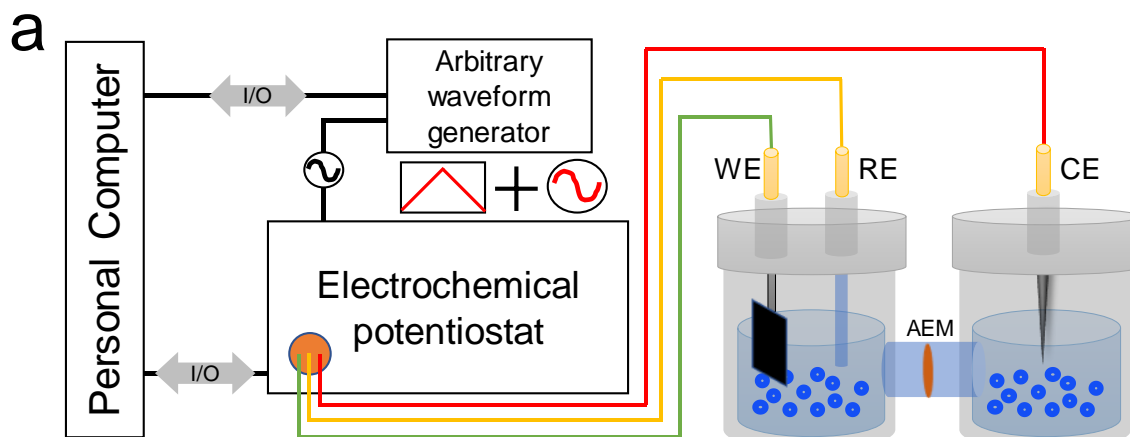
Supplementary Figure S35. The schematic (a) and photos (b-c) of experimental apparatus to conduct the Fourie transformed alternating current voltammetry (FTacV) measurements.
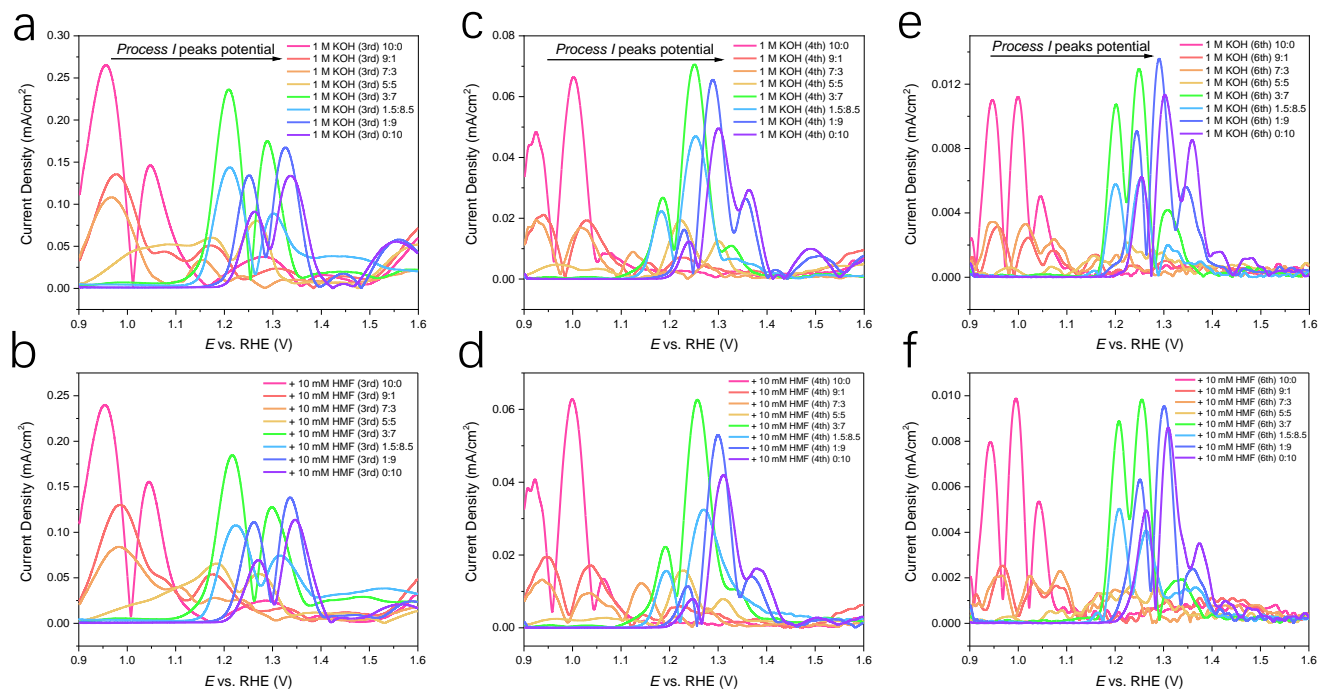
Supplementary Figure S36. The extracted 3rd (a, b), 4th (c, d) and 6th (e, f) harmonics in the conditions of OER and HMF electro-oxidation. All electrochemical data were presented without *iR*-correction. The size of carbon papers (C.P.) were 1×2 cm^2.
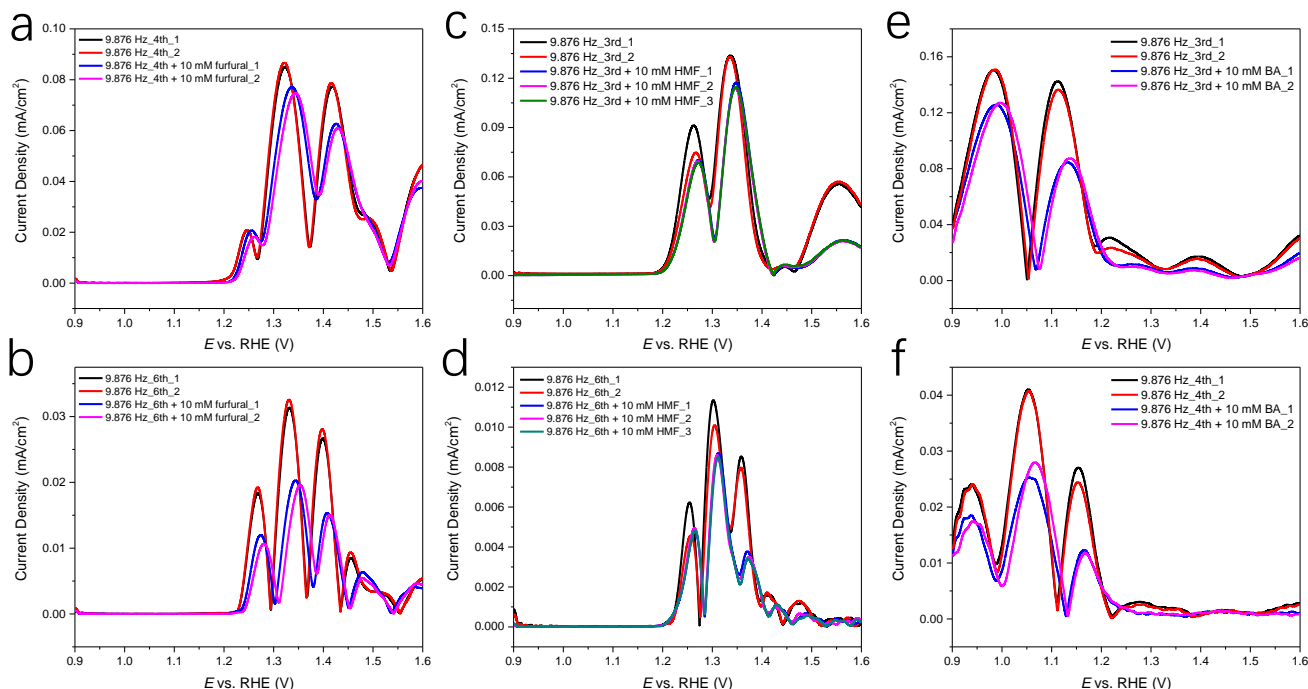
Supplementary Figure S37. The harmonics extracted from the FTacV measurements, (a, b) the spinel derived oxyhydroxides catalyzed furfural oxidation, (c, d) nickel doped cobalt hydroxides catalyzed HMF oxidation and (e, f) doped nickel hydroxides catalyzed BA oxidation. **It is worthy to note that the current densities and the main peaks potential of the harmonics in OER and electro-oxidation conditions both stay relative very stable unless the organic substrates have been added.** All electrochemical data were presented without *iR*-correction. The size of carbon papers (C.P.) were 1×2 cm^2.
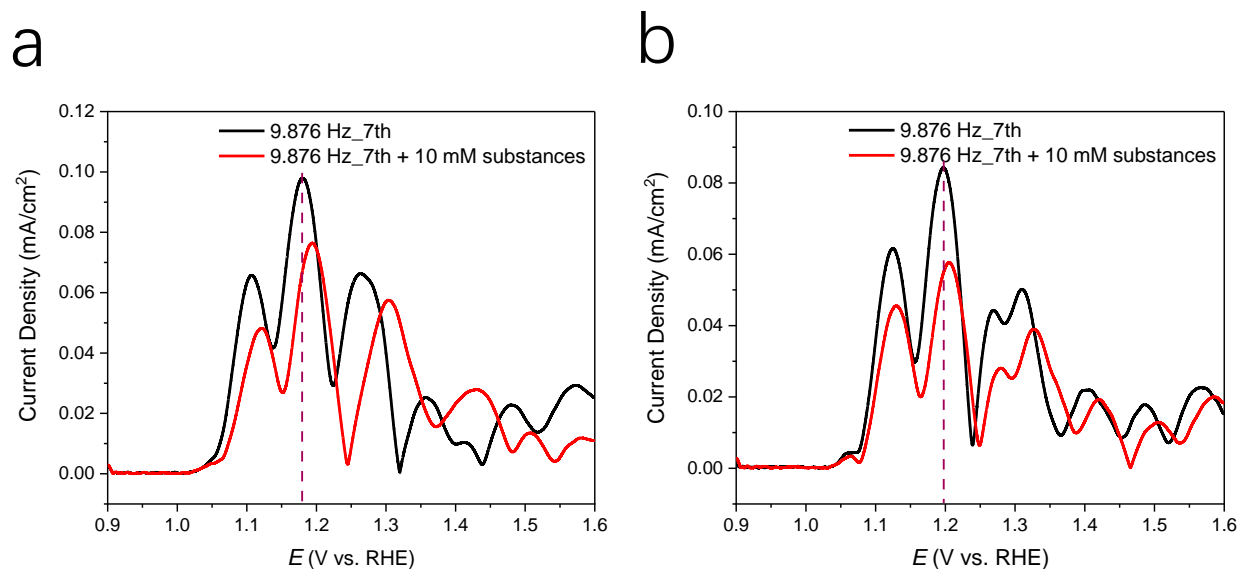
Supplementary Figure S38. The odd (7th) high-order harmonics of α-Co$_{0.1}$Ni$_{0.9}$(OH)$_2$ (a) and α-Ni(OH)$_2$

(b).
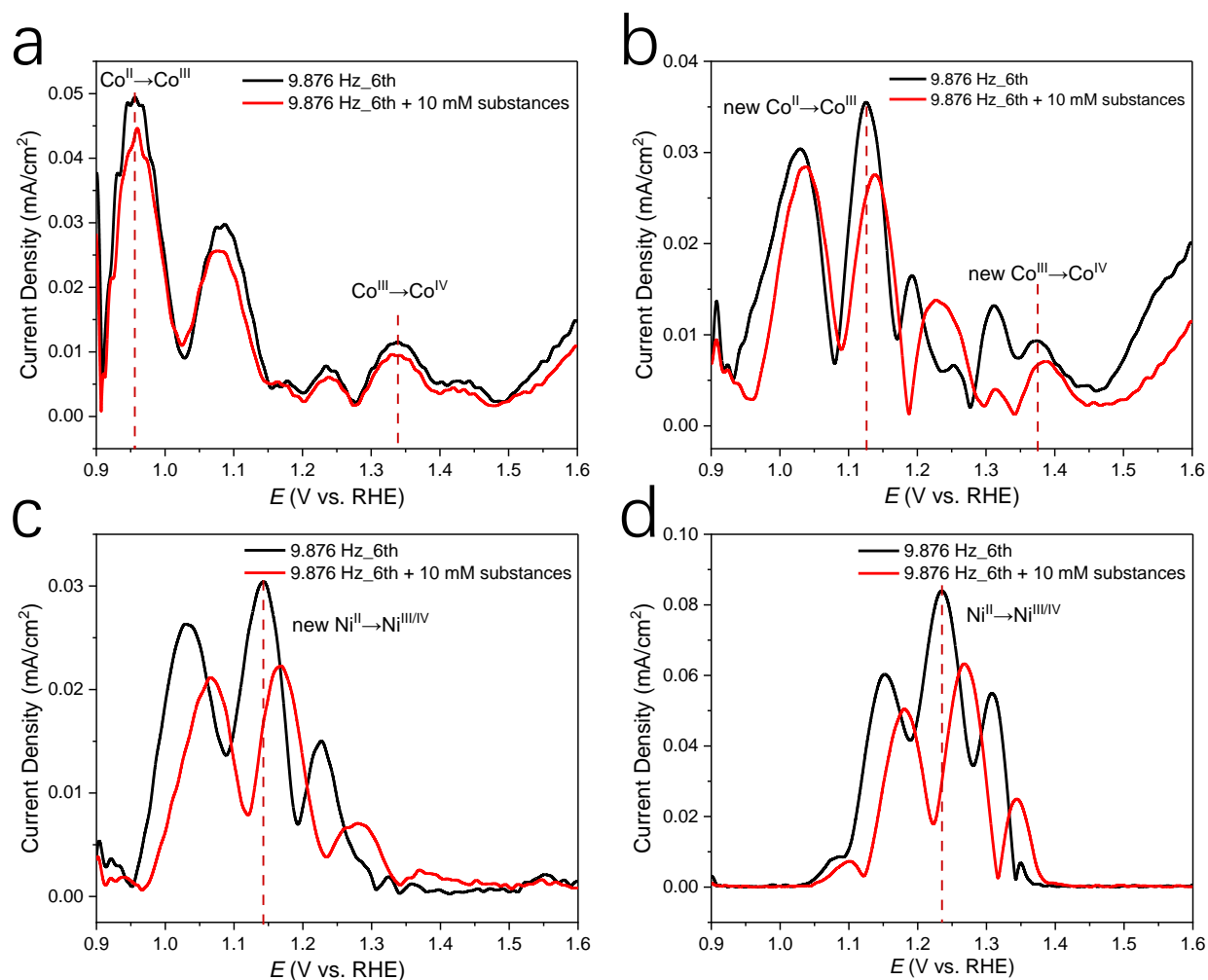
Supplementary Figure S39. The detailed Co and Ni sites clarification of α-Co(OH)$_2$ (a), α-Co$_{0.7}$Ni$_{0.3}$(OH)$_2$ (b), α-Co$_{0.5}$Ni$_{0.5}$(OH)$_2$ (c) and α-Ni(OH)$_2$ (d). The "M" in main text represents Ni sites because of its dominant Ni^{3+}−O Raman (**Figure 2e-f** and **Supplementary Figure S27**) and *Process I* peaks, unless the Co composition is larger than 70%. The Co^{II}−H$_2$O* → Co^{III}−OH* and Co^{III}−OH* → Co^{IV}−OH* processes can be well distinguished in the α-Co(OH)$_2$ and α-Co$_{0.7}$Ni$_{0.3}$(OH)$_2$ catalysts (a, b), while the Ni^{II}−H$_2$O* → Ni$^{III/IV}$−OH* process is almost indistinguishable in α-Co$_{0.5}$Ni$_{0.5}$(OH)$_2$ (c) and α-Ni(OH)$_2$ (d). All electrochemical data were presented without *iR*-correction. The size of carbon papers (C.P.) were 1×2 cm^2.

Theoretical explanations of high-order FTacV harmonics (Note 5)

The major advantage of the high-order harmonics extracted from the FTacV measurements is its ability to separate relative fast electron transfer (E) from coupled electrocatalytic processes (C).[18] To demonstrate how high-order FTacV harmonics deconvolute the E and coupled C processes, considering a reversible surface E (equation S61) and a homogeneous catalytic reaction (equation S61):

$$O\,(\text{surf}) + e^- \rightleftharpoons R\,(\text{surf}) \tag{60}$$

$$R\,(\text{surf}) + S^* \longrightarrow O\,(\text{surf}) + P^* \tag{61}$$
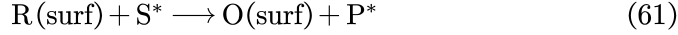
The analytical solution for the dc component (equation S62)[19] contains terms from both E and catalytic process. The first term is independent of potential and represents half of the limiting plateau current associated with the coupled catalytic process. Thus the catalytic reactions contribute both the shape and magnitude of the dc component.

$$I_{\text{dcnorm}} = -\frac{K_{\text{catl}}}{2} - \sum_{N=0}^{\infty} \frac{g^{(2N+1)}\left(\frac{E_{\text{dcnorm}}(\tau) - E_{\text{norm}}^{0'}}{2}\right) - 2K_{\text{catl}}g^{(2N)}\left(\frac{E_{\text{dcnorm}}(\tau) - E_{\text{norm}}^{0'}}{2}\right)}{(2N!)^2}\left(\frac{\Delta E_{\text{norm}}}{4}\right)^{2N} \tag{62}$$

$$I_{1^{\text{st}}\ \text{norm}} = (K_{\text{catl}}\sin(\Omega\tau) + \Omega\cos(\Omega\tau))\sum_{N=0}^{\infty} \frac{g^{(2N+1)}\left(\frac{E_{\text{dcnorm}}(\tau) - E_{\text{norm}}^{0'}}{2}\right)}{N!\,(N+1)!}\left(\frac{\Delta E_{\text{norm}}}{4}\right)^{2N+1} \tag{63}$$

$$I_{2^{\text{nd}}\ \text{norm}} = (-K_{\text{catl}}\sin(2\Omega\tau) + 2\Omega\cos(2\Omega\tau))\sum_{N=0}^{\infty} \frac{g^{(2N+2)}\left(\frac{E_{\text{dcnorm}}(\tau) - E_{\text{norm}}^{0'}}{2}\right)}{N!\,(N+2)!}\left(\frac{\Delta E_{\text{norm}}}{4}\right)^{2N+2} \tag{64}$$

$$I_{3^{\text{rd}}\ \text{norm}} = -(K_{\text{catl}}\sin(3\Omega\tau) + 3\Omega\cos(3\Omega\tau))\sum_{N=0}^{\infty} \frac{g^{(2N+1)}\left(\frac{E_{\text{dcnorm}}(\tau) - E_{\text{norm}}^{0'}}{2}\right)}{(N-1)!(N+2)!}\left(\frac{\Delta E_{\text{norm}}}{4}\right)^{2N+1} \tag{65}$$

$$
\begin{aligned}
I_{\text{norm, odd}} = & \sum_{N=0}^{\infty} g^{(2N+1)}\left(\frac{E_{\text{dcnorm}}(\tau) - E_{\text{norm}}^{0'}}{2}\right)\left(\frac{\Delta E_{\text{norm}}}{4}\right)^{2N+1} \\
& \times \sum_{i=0}^{N} \frac{(-1)^i\{K_{\text{catl}}\sin[(2i+1)\Omega\tau] + (2i+1)\Omega\cos[(2i+1)\Omega\tau]\}}{(N-i)1(N+i+1)!}
\end{aligned} \tag{66}
$$

$$
\begin{aligned}
I_{\text{norm, even}} = & \sum_{N=0}^{\infty} g^{(2N+2)}\left(\frac{E_{\text{dcnorm}}(\tau) - E_{\text{norm}}^{0'}}{2}\right)\left(\frac{\Delta E_{\text{norm}}}{4}\right)^{2N+2} \\
& \times \sum_{i=0}^{N} \frac{(-1)^i\{-K_{\text{catl}}\cos[(2i+1)\Omega\tau] + (2i+1)\Omega\sin[(2i+1)\Omega\tau]\}}{(N-i)1(N+i+2)!}
\end{aligned} \tag{67}
$$

Equations S63−S65 derived for the 1st, 2nd, 3rd harmonic components also contain contributions from E and catalytic processes. However, unlike the dc component, equations S63−S65 elucidate that the catalytic processes do not contribute to the shape of the ac components because this feature is only determined by the terms present within the summation notation, which are devoid of variables related to the catalytic

reaction. Comparison of these two terms leads to the conclusion that the catalytic reaction contribution becomes less significant the higher the order of the harmonic. **The contribution from the catalytic process is predicted to become insignificant when the harmonic order or frequency of the higher harmonic is sufficiently high (6ᵗʰ in this work).**[18] Therefore, according to the theoretical analysis, contributions from the heterogeneous electron transfer process and coupled homogeneous catalytic process can be effectively deconvoluted using high-order harmonics extracted from FTacV measurements.

Simulation of the FTacV harmonics
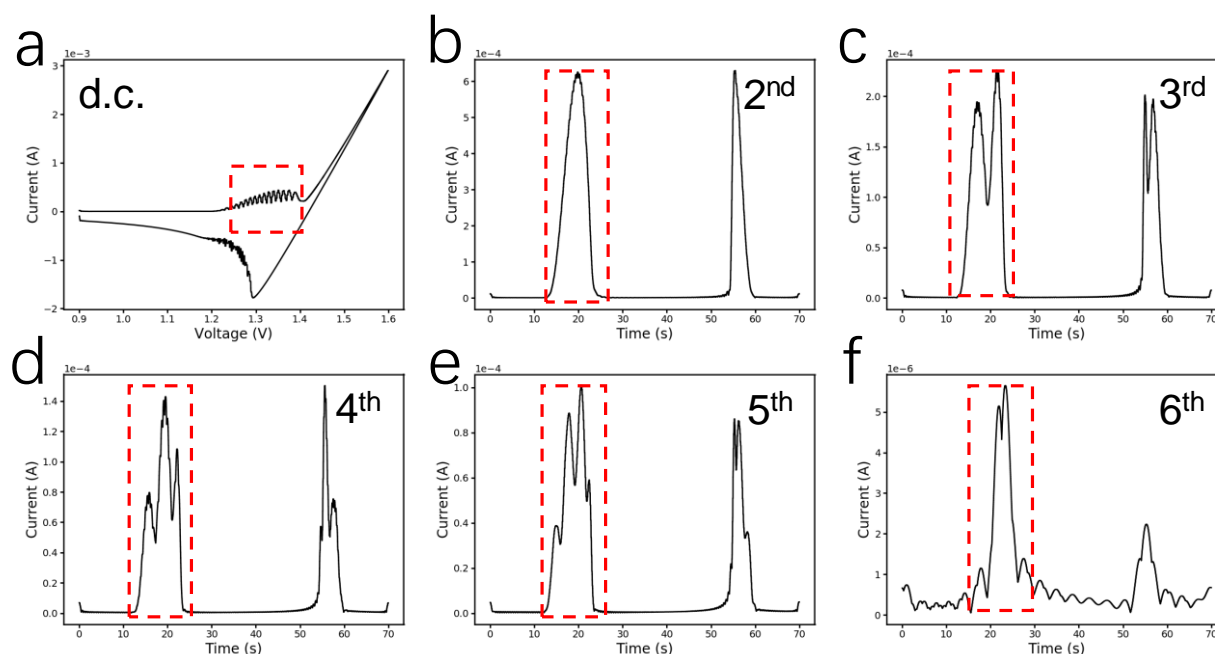
Supplementary Figure S40. The simulated results of d.c. CV (a) and FTacV harmonics (b-f) using MECSim program package using the "surface confined catalysis" mechanism.[20] It is obvious that the harmonics peaks are mainly originated from the oxidation/reduction of the transition metal active sites (dashed red boxes) accompanied by $M^{III}–OH^* \rightarrow M^{IV}–OH^* + e^-$ process. It is also need to note that there are almost no harmonics peaks generation during *Process II* of OER.

Comparison of d.c. CV and FTacV harmonics at different potential scan rates
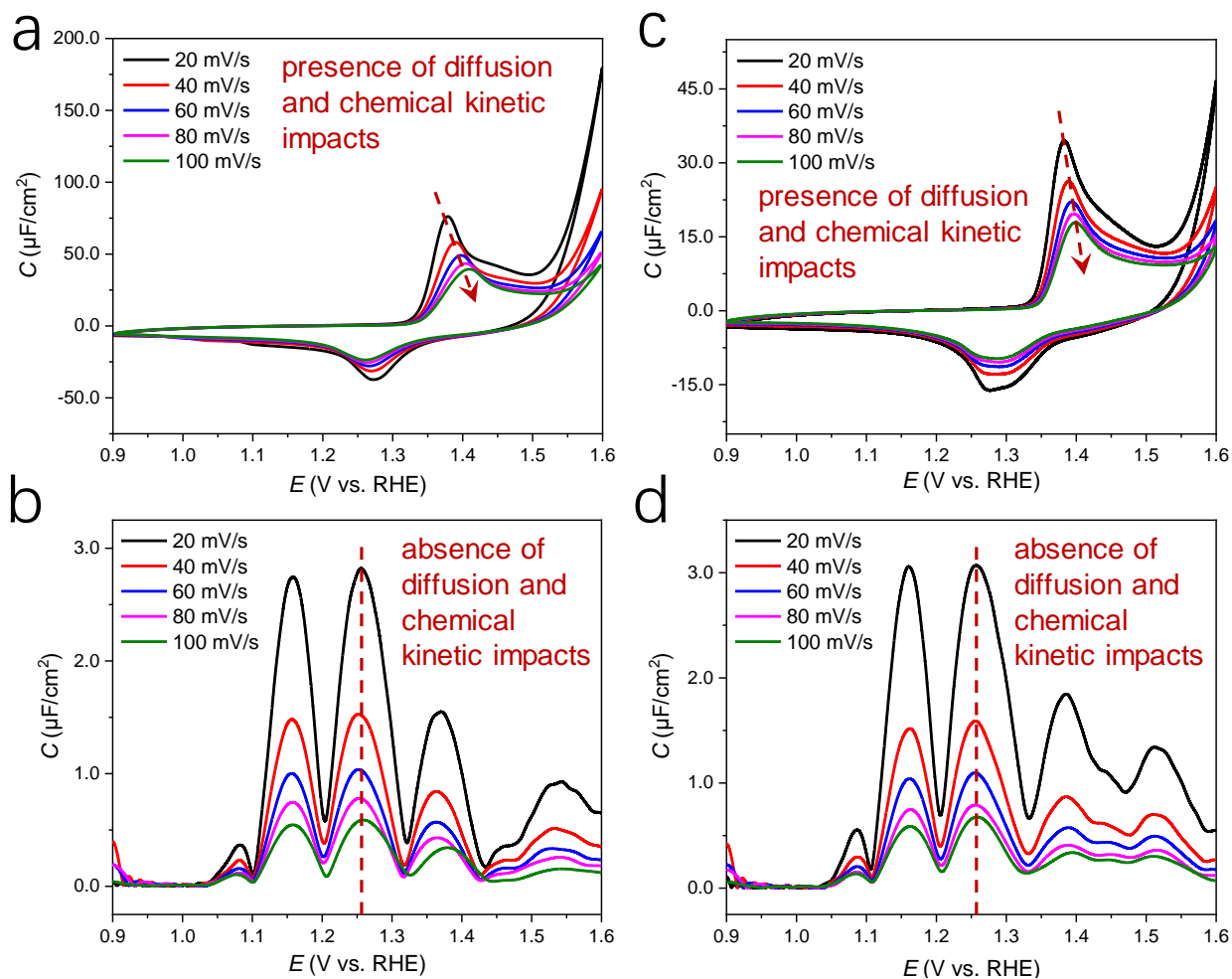
Supplementary Figure S41. The comparison of d.c. CV and FTacV in the condition of different scan rate, the capacitance have been converted by C = current density / scan rate. It can be seen that the redox peak potential in a and c varies with the scan rate, while the *Process I* peaks in (b) and (d) stay unchanged. Therefore, the extracted peak potential well represents the ΔG of $M^{III}-OH^* \rightarrow M^{IV}-OH^* + e^-$, excluding the diffusion and chemical kinetic (electro-adsorption) impacts. All electrochemical data were presented without *iR*-correction. The size of carbon papers (C.P.) were 1×2 cm^2.

In classical d.c. CV, with the linear increasing of electrochemical potential, the diffusion of H_2O/OH^- and electro-adsorption of OH* proceed gradually when the scan rate was not so high. Then the peak potential of $M^{II}-H_2O^* + OH^- \rightarrow M^{III/IV}-OH^* + H_2O + e^-$ in the potential range of 1.3~1.4 V is influenced by both diffusion of H_2O/OH^- and electro-adsorption of OH* ($\ln[\theta_{OH^*}/(1-\theta_{OH^*})]$).

In the FTacV measurement, the potential varies at a large amplitude of sinusoidal wave ($E = E^0 + vt +$ $A\sin(2\pi ft)$) so fast that the reactive species in the solution phase (such as H_2O/OH^-) do not have enough time to diffuse appreciably to the electrode surface. In such condition, only the electron transfer steps involving pre-adsorbed OH*/H$_2$O* (with fast enough kinetics) would generate the current response at the measured potential (in this work, M^{III}–OH* → M^{IV}–OH* + e$^-$ or M^{II}–H$_2$O* → M^{III}–OH* + e$^-$ + H*-μ$_2$O (bridge O)[6, 21]. The redox transition between these pre-adsorbed states do not involve solution phase reactants and structural rearrangement, exhibiting much faster kinetics compared to other elementary steps (k_{fast} / k_{slow} > 10^2), and thus solely contribute to the high-order FTacV harmonic signals. The specific potential-dependent electro-adsorption process of OH* with slower kinetics leads to negligible FTacV signal response, and would not be reflected in the overall FTacV results.

Correlation coefficient between the two physio-chemical descriptors
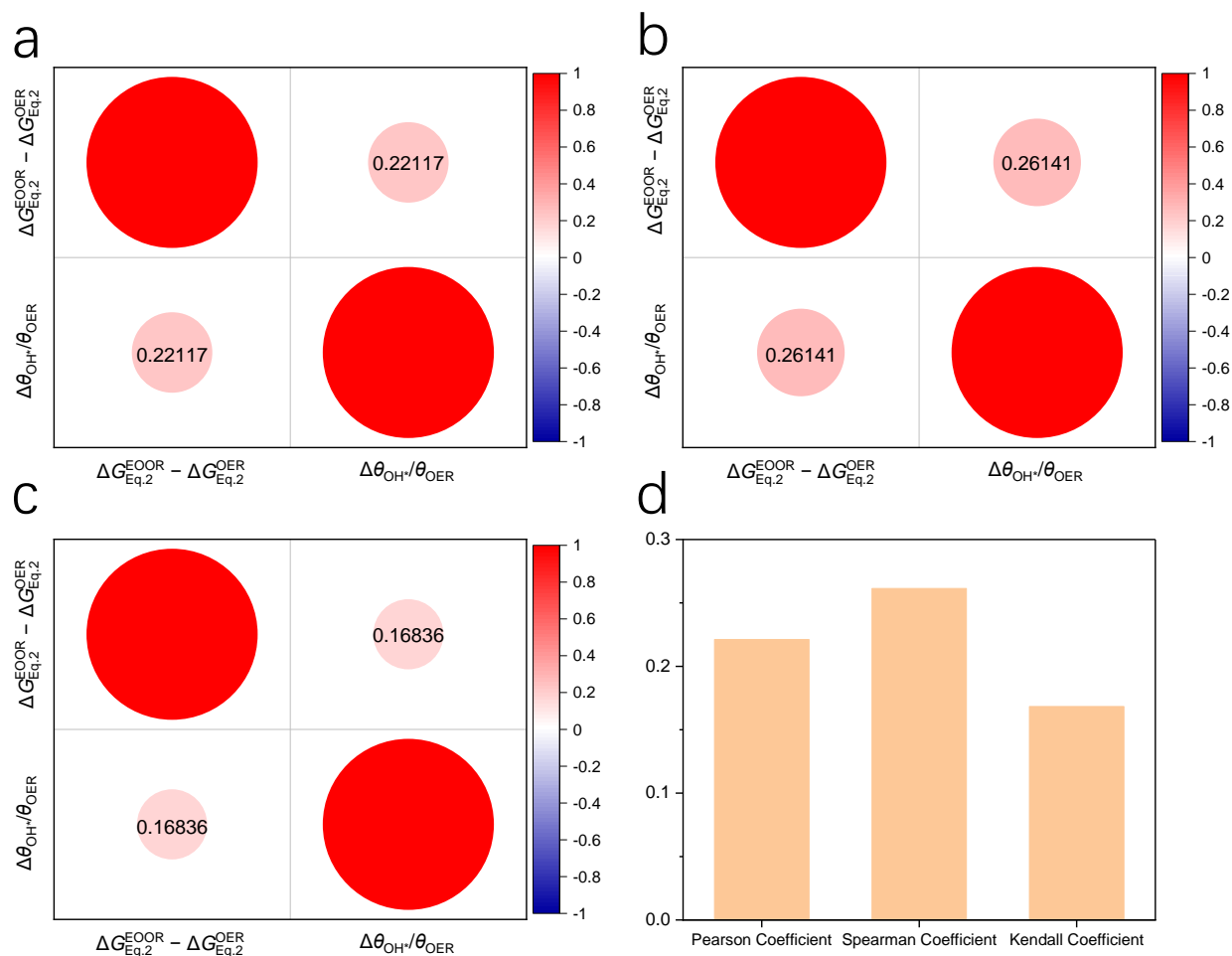
Supplementary Figure S42. The Pearson, Spearman and Kendall coefficients of two physio-chemical descriptors, $\Delta\Delta G_{OH^*}^{EOOR-OER}$ and $\Delta\theta_{OH^*}/\theta_{OH^*}^{OER}$, all of them indicate the relatively small correlation between the two descriptors.

Mathematical correlation between the experimental parameters and two physio-chemical descriptors (Note 6)

(1) The correlations between FTacV peak current (from high-order harmonics) and the quantity of the electro-active sites can be found in previous discussions.[18, 22-26] Based on the general model of a single-surface-confined electroactive species with a surface concentration that follows the Nernst equation with no thermodynamic (single and constant E^0) or kinetic dispersion (single and constant k^0), the quantitative

parameters including the surface concentration of active sites and rate constant (of the elementary step corresponding to the fast electron transfer process) can be extracted from the simulation by fitting to experimental data. In this work, the software package MECSim[20] was used for such model simulation.

Briefly, the specific fast electron transfer steps of OER and EOOR in this investigation can be written as $M^{\delta+}-OH^* \rightarrow M^{\delta+1}-OH^* + e^-$, where M=Co, Ni (+3 to +4). As a result, the ΔI in FTacV exclusively reflects the kinetics of this specific fast electron transfer step, which is proportional to the amount of electrochemically active species ($M^{\delta+}-OH^*$). This correlation can be demonstrated by the following numerical expression:

$$j_{FTacV} \propto r_{fast\ e-process} = \frac{\partial c_{M^{\delta+}-OH^*}}{\partial t} = k_0 \exp\left[\frac{\alpha F(E - E^0)}{RT}\right] c_{M^{\delta+}-OH^*} \quad (68)$$

where $c_{M^{\delta+}-OH^*}$ is the surface concentration of electrochemically active species ($M^{\delta+}-OH^*$). With the experimental determination of the initial surface concentration of the active metal sites, $c_{M^{\delta+}-OH^*}$ can be converted to $\theta_{M^{\delta+}-OH^*}$.

Furthermore, the water-assisted EOOR is a typical surface EC reaction. Once the electrochemically active $M^{3+\delta}-OH^*$ species are generated, the reaction between $M^{2++\delta}-Sub^*$ and $M^{3+\delta}-OH^*$ proceeds spontaneously. Meanwhile, the adsorption of organic substance to form $M^{2++\delta}-Sub^*$ will in turn reduce the available sites for the OH^* adsorption, practically reduce the surface coverage of $M^{3+\delta}-OH^*$ (as compared to intrinsic $M^{3+\delta}-OH^*$ coverage during OER). Hence, this work focused more on the change in coverage of active $M^{3+\delta}-OH^*$ species (designated as $\Delta\theta_{OH^*}/\theta_{OH^*}^{OER} = (\theta_{OH^*}^{EOOR} - \theta_{OH^*}^{OER})/\theta_{OH^*}^{OER}$) by calculating the relative change in harmonic peak currents, rather than extracting the absolute values of $c_{M^{\delta+}-OH^*}$ or $\theta_{M^{\delta+}-OH^*}$. Specifically, at the fixed potential:

$$\frac{\Delta I_{harmonics}^{EOOR-OER}}{I_{harmonics}^{OER}} = \frac{I_{harmonics}^{EOOR} - I_{harmonics}^{OER}}{I_{harmonics}^{OER}} = \frac{k'(c_{surface\ OH^*}^{EOOR} - c_{surface\ OH^*}^{OER})}{k' c_{surface\ OH^*}^{OER}}$$

$$= \frac{(c_{surface\ OH^*}^{EOOR} - c_{surface\ OH^*}^{OER})/c_{overall\ sites}}{c_{surface\ OH^*}^{OER}/c_{overall\ sites}} = \frac{\theta_{OH^*}^{EOOR} - \theta_{OH^*}^{OER}}{\theta_{OH^*}^{OER}} = \frac{\Delta\theta_{OH^*}^{EOOR-OER}}{\theta_{OH^*}^{OER}} \quad (69)$$

(2) It should be noted that, experimentally measure precise ΔG values for each elementary step is extremely challenging, as the observed electrochemical potentials were intrinsically determined by both equilibrium potential of the reaction and the activation energy barriers regarding the transitions state, and

the non-single-crystal surfaces of NiCo oxyhydroxides casts further challenges for experimental measurements. However, the $\Delta V_{\text{harmonics}}$ in FTacV reflects the changes in ΔG under OER conditions and different EOOR conditions, i.e., $\Delta\Delta G_{\text{OH}*}^{\text{EOOR}-\text{OER}}$ (defined as $\Delta\Delta G_{\text{OH}*}^{\text{EOOR}-\text{OER}} = \Delta G_{\text{OH}*}^{\text{EOOR}} - \Delta G_{\text{OH}*}^{\text{OER}}$), which can therefore be used to evaluate the variations in different EOOR reactions that share the same thermodynamic parameter with OER pathway. The measured $\Delta V_{\text{harmonics}}$ (V) values using FTacV is numerically equivalent to $\Delta(\Delta G_{\text{OH}*})$ (eV) to evaluate the variations in different EOOR systems that share the same thermodynamic parameter. This parameter is of great significance towards catalysts design as it represents an intrinsic thermodynamic factor that determines whether the electrocatalytic reactions favors the EOOR or OER pathways, which can be rationally modulated by tailoring the electronic structures of metal sites for different organic substances.
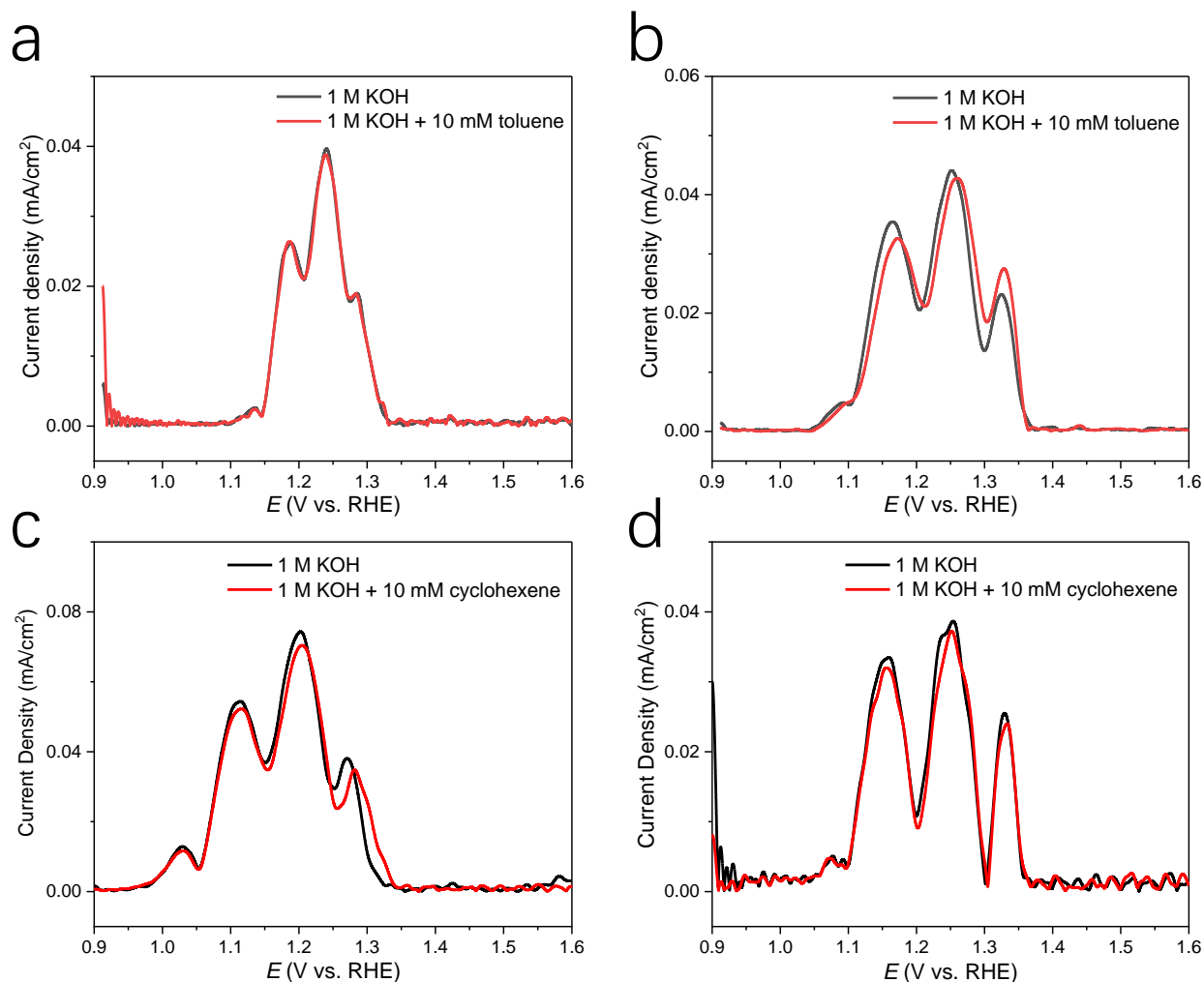
Supplementary Figure S43. The high-order (6th) harmonics of α-Co$_{0.15}$Ni$_{0.85}$(OH)$_2$ (a, c) and α- Ni(OH)$_2$ (b, d) in pure 1 M KOH and the addition of 10 mM toluene and cyclohexene, respectively, where the

signals show almost no significant variation. All electrochemical data were presented without *iR*-correction. The size of carbon papers (C.P.) were 1×2 cm^2.
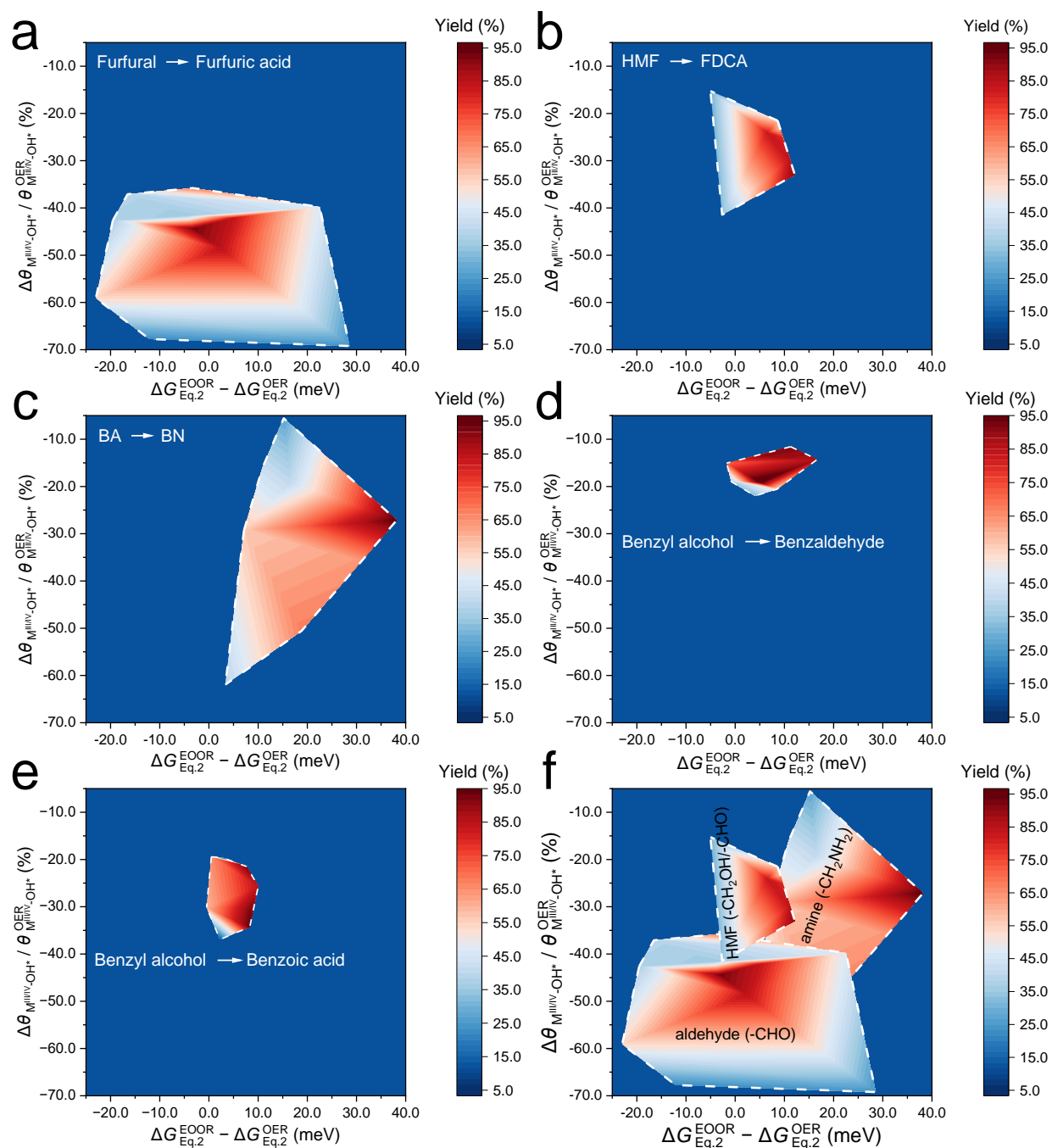
Supplementary Figure S44. The color maps drawn by the data derived from FTacV for (a) FCA yield (oxidation from furfural), (b) FDCA yield (oxidation from HMF), (c) BN yield (oxidation from BA), (d) benzaldehyde yield (oxidation from benzyl alcohol) and (e) benzoic acid yield (oxidation from benzyl

alcohol), respectively. The summarized results can be seen in (f), where the reactive "hot zones" of different substrates can be separated clearly. **Note that the "Eq.2" in abscissa axis represents the reaction 2 in the main text.**
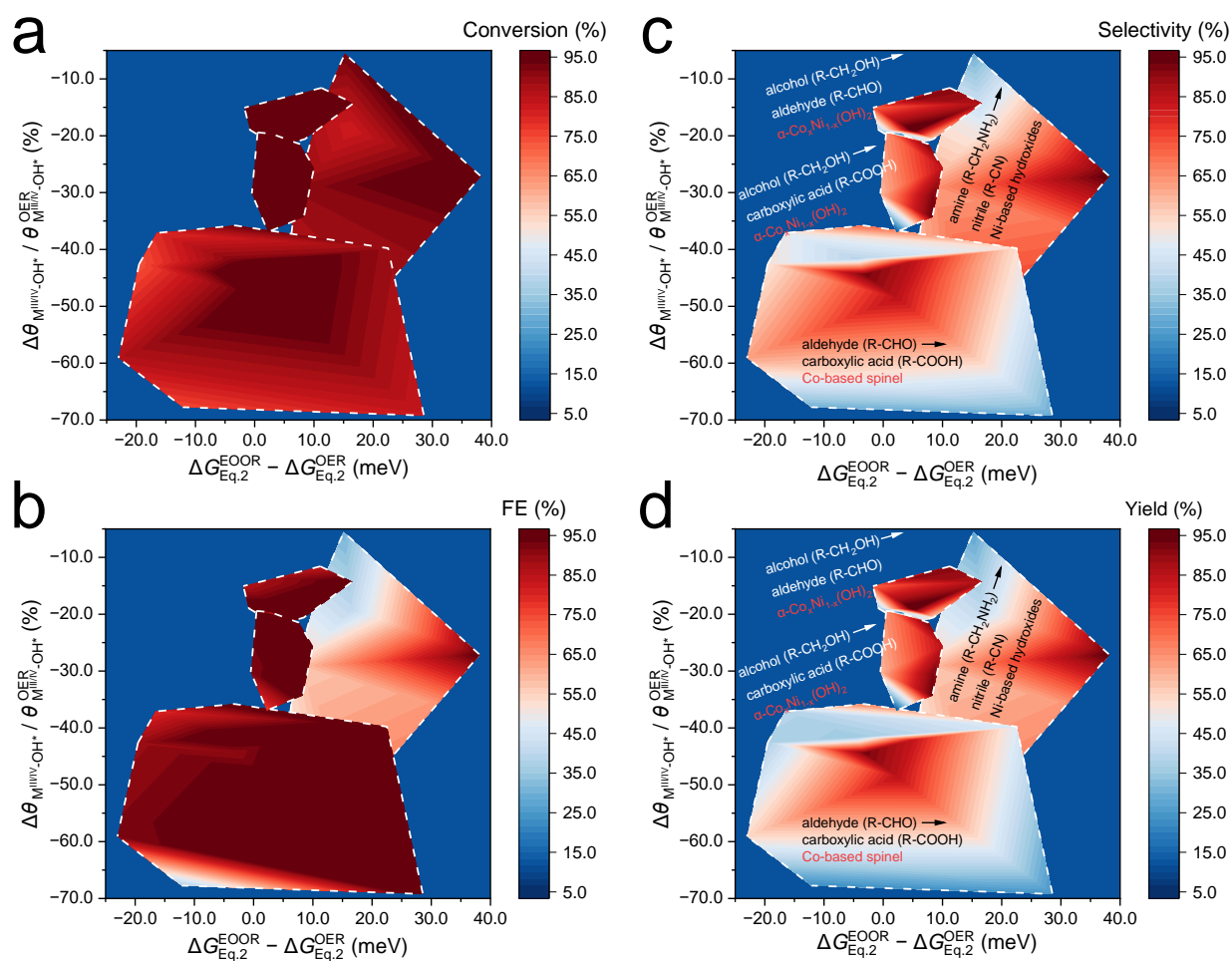
Supplementary Figure S45. The catalytic activity diagrams for EOORs, constructed by two operando physio-chemical descriptors and four key parameters, conversion, yield, selectivity and FEs. **Note that the "Eq.2" in abscissa axis represents the reaction 2 in the main text.**

Specifically, for model EOORs that have relatively easy-to-activate substrates with few side reactions (confirmed by the HPLC/GC quantification, see **Supplementary Fig. S31**), the conversion is generally high, and the reaction yield is equivalent to the selectivity. In case of multiple possible products (such as alcohol to aldehyde or carboxylic acid conversion) when selectivity is critical, it can be divided into two separate reactions (alcohol to aldehyde and alcohol to carboxylic acid) for performance consideration. Furthermore, FE corelates to the overall energy efficiency in EOORs and reflects other non-organic side

reactions such as OER. It is therefore a relatively independent parameter from yield /selectivity offering additional information.

Activity diagrams obtained by d.c. CV
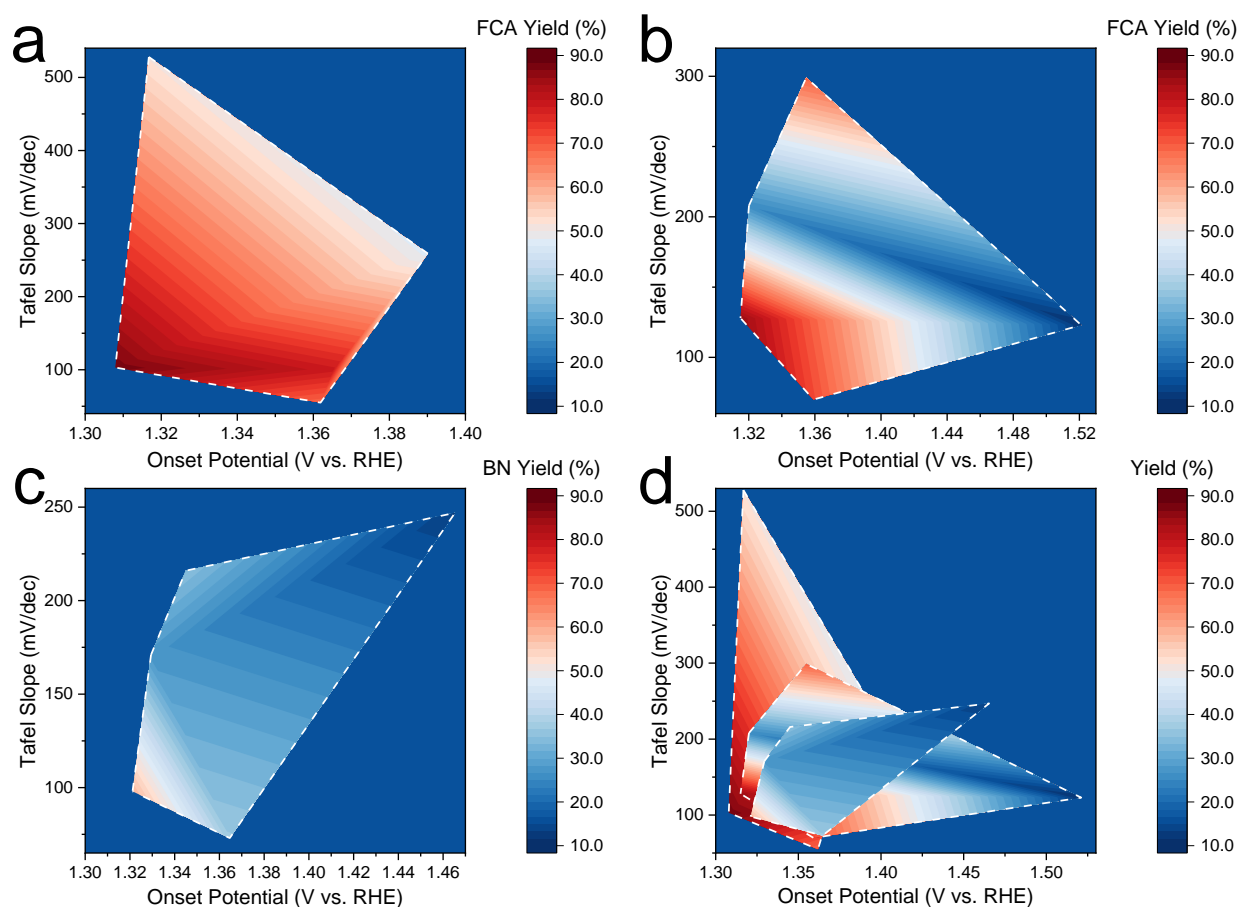
Supplementary Figure S46. The activity diagrams drawn by the data extracted from d.c. CV of a series of Ni doped Co hydroxides for (a) yield of FCA (oxidation from furfural), (b) yield of FCA (oxidation from furfuryl alcohol) and (c) BN yield (oxidation from BA), respectively. The summarized results can be seen in (d), it is obvious that the reactive areas of three substrates overlap with each other.
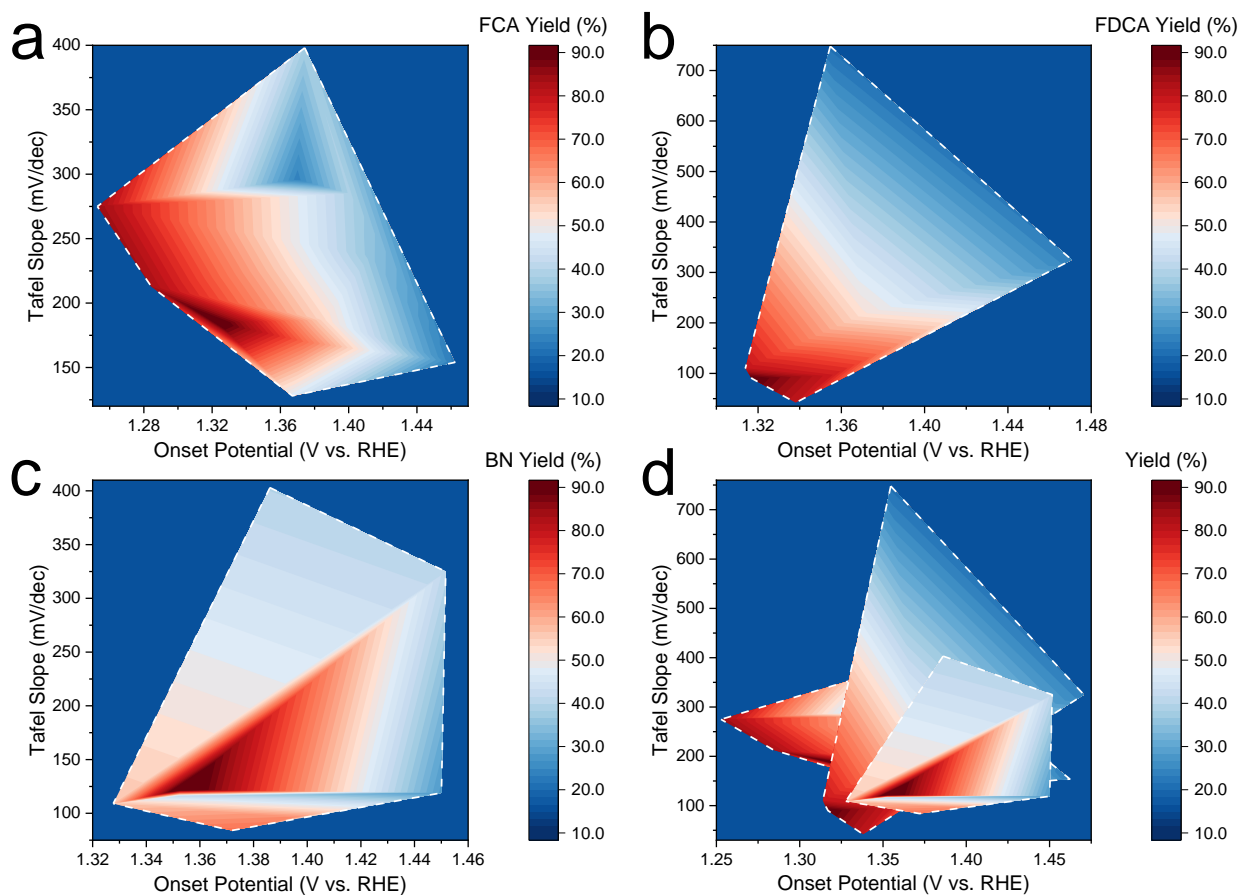
Supplementary Figure S47. The activity diagrams drawn by the data extracted from d.c. CV for (a) FCA yield (spinel derived Co oxyhydroxides catalyzed furfural oxidation), (b) FDCA yield (a series of Ni doped Co hydroxides catalyzed HMF oxidation) and (c) BN yield (mental doped Ni hydroxides catalyzed BA oxidation), respectively. The summarized results can be seen in (d), it is obvious that the reactive areas of three substrates overlap with each other.
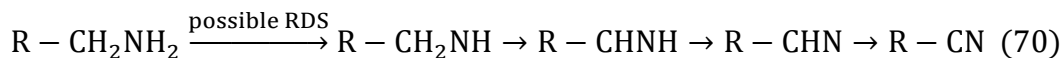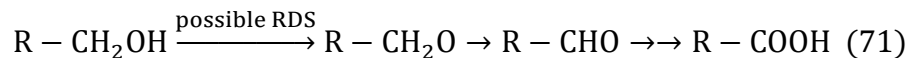
Mechanism analysis of alcohol and amine oxidation (Note 7)

For the amine oxidation, the mechanisms including:[21, 27]

$$R - CH_2NH_2 \xrightarrow{\text{possible RDS}} R - CH_2NH \rightarrow R - CHNH \rightarrow R - CHN \rightarrow R - CN \quad (70)$$

The simplified amine oxidation process including four dehydrogenation steps.

For the alcohol oxidation, the mechanisms including:[27]

$$R - CH_2OH \xrightarrow{\text{possible RDS}} R - CH_2O \rightarrow R - CHO \rightarrow\rightarrow R - COOH \quad (71)$$

The simplified alcohol oxidation process including three dehydrogenation steps and one OH insertion step.

Due to the larger pK_a of R-CH_2NH_2 than R-CH_2OH, the energy barrier for R-CH_2NH_2 oxidation is larger than R-CH_2OH oxidation.

Theoretical considerations on the thermodynamic and kinetic contributions in $\Delta V_{\text{harmonics}}$ signals (Note 8)

In classical d.c. CV, with the linear increasing of electrochemical potential, the diffusion of H_2O/OH^- and electro-adsorption of OH* proceed gradually when the scan rate was not so high. Then the peak potential of $M^{II}-H_2O^* + OH^- \rightarrow M^{III/IV}-OH^* + H_2O + e^-$ in the potential range of 1.3~1.4 V is influenced by both diffusion of H_2O/OH^- and electro-adsorption of OH* ($\ln[\theta_{OH*}/(1-\theta_{OH*})]$).

In the FTacV measurement, the potential varies at a large amplitude of sinusoidal wave ($E = E^0 + vt + A\sin(2\pi ft)$) so fast that the reactive species in the solution phase (such as H_2O/OH^-) do not have enough time to diffuse appreciably to the electrode surface. In such condition, only the electron transfer steps involving pre-adsorbed OH*/H_2O* (with fast enough kinetics) would generate the current response at the measured potential (in this work, $M^{III}-OH^* \rightarrow M^{IV}-OH^* + e^-$ or $M^{II}-H_2O^* \rightarrow M^{III}-OH^* + e^- + H^*$-$\mu_2O$ (bridge O)[6, 21]. The redox transition between these pre-adsorbed states do not involve solution phase reactants and structural rearrangement, exhibiting much faster kinetics compared to other elementary steps ($k_{fast} / k_{slow} > 10^2$), and thus solely contribute to the high-order FTacV harmonic signals. The specific potential-dependent electro-adsorption process of OH* with slower kinetics leads to negligible FTacV signal response, and would not be reflected in the overall FTacV results (see Chapter 3, *Zouraris Dimitrios*,

Electrochemical study of redox enzymes and their utilization on modified electrodes, Doctoral Thesis). For better clarifying this issue, the Equation 1 was updated to include more surface details in revised manuscript as: $M^{II}-H_2O^* \rightarrow M^{III}-OH^* + e^- + H^*-\mu_2O$ (bridge O). Moreover, the rate constant k of the fast electron transfer step, as a function of pre-exponential factor and activation energy (T), would not demonstrate apparent change without the structural variation of the $M^{III}-OH^*$ and $M^{II}-H_2O^*$ sites, even in the condition of EOOR.

Based on the above analysis, the principal peak potential of high-order FTacV harmonics directly reflects the standard (or formal) electrode potential of the fast electron transfer steps (electron transfer steps involving pre-adsorbed OH^*/H_2O^*), reflecting no impact of diffusion or potential-dependent chemical kinetic limitations.[28] Therefore, the experimentally extracted value of $\Delta V_{harmonics}$ in high-order FTacV harmonic signal mostly represent the change in ΔG of Eq. 1 and/or Eq. 2 in the main text, with negligible kinetic contribution of other elementary steps.

Supplementary References

1.   Trotochaud, L., Young, S.L., Ranney, J.K., Boettcher, S.W. Nickel–Iron Oxyhydroxide Oxygen-Evolution Electrocatalysts: The Role of Intentional and Incidental Iron Incorporation. *J. Am. Chem. Soc.* **136**, 6744-6753 (2014).

2.   Halim, U.*, et al.* A rational design of cosolvent exfoliation of layered materials by directly probing liquid–solid interaction. *Nat. Commun.* **4**, 1-7 (2013).

3.   Ding, M., He, Q., Wang, G., Cheng, H.-C., Huang, Y., Duan, X. An on-chip electrical transport spectroscopy approach for in situ monitoring electrochemical interfaces. *Nat. Commun.* **6**, 1-9 (2015).

4.   Mu, Z.*, et al.* On-Chip Electrical Transport Investigation of Metal Nanoparticles: Characteristic Acidic and Alkaline Adsorptions Revealed on Pt and Au Surface. *J. Phys. Chem. Lett.* **11**, 5798-5806 (2020).

5.   Ding, M.*, et al.* On-Chip in Situ Monitoring of Competitive Interfacial Anionic Chemisorption as a Descriptor for Oxygen Reduction Kinetics. *ACS Cent. Sci.* **4**, 590-599 (2018).

6.   Tian, B.*, et al.* Double-Exchange-Induced in situ Conductivity in Nickel-Based Oxyhydroxides: An Effective Descriptor for Electrocatalytic Oxygen Evolution. *Angew. Chem. Int. Ed.* **60**, 16448-16456 (2021).

7.   Zhu, X., Huang, J., Eikerling, M. pH Effects in a Model Electrocatalytic Reaction Disentangled. *JACS Au* **3**, 1052-1064 (2023).

8.   Zhang, J.*, et al.* Advances in Thermodynamic-Kinetic Model for Analyzing the Oxygen Evolution Reaction. *ACS Catal.* **10**, 8597-8610 (2020).

9.   Ran, P.*, et al.* Universal High-Efficiency Electrocatalytic Olefin Epoxidation via a Surface-confined Radical Promotion. *Nat. Commun.* **15**, 8877 (2024).

10. Song, J.-M.*, et al.* A facile synthesis of graphene-like cobalt–nickel double hydroxide nanocomposites at room temperature and their excellent catalytic and adsorption properties. *J. Nanopart. Res.* **16**, 2269 (2014).

11. Xu, H.*, et al.* Heterogeneous $Co(OH)_2$ nanoplates/Co_3O_4 nanocubes enriched with oxygen vacancies enable efficient oxygen evolution reaction electrocatalysis. *Nanoscale* **10**, 18468-18472 (2018).

12. Bao, J.*, et al.* A ternary cobalt–molybdenum–vanadium layered double hydroxide nanosheet array as an efficient bifunctional electrocatalyst for overall water splitting. *Chem. Commun.* **55**, 3521-3524 (2019).

13. Gao, M.*, et al.* Efficient water oxidation using nanostructured α-nickel-hydroxide as an electrocatalyst. *J. Am. Chem. Soc.* **136**, 7077-7084 (2014).

14. Liu, S.*, et al.* Efficient CO_2 Electroreduction with a Monolayer Bi_2WO_6 through a Metallic Intermediate Surface State. *ACS Catal.* **11**, 12476-12484 (2021).

15. Pan, Y.*, et al.* Boosting the performance of single-atom catalysts via external electric field polarization. *Nat. Commun.* **13**, 3063 (2022).

16. Han, S.*, et al.* Ultralow overpotential nitrate reduction to ammonia via a three-step relay mechanism. *Nat. Catal.* **6**, 402-414 (2023).

17. Mefford, J.T.*, et al.* Correlative operando microscopy of oxygen evolution electrocatalysts. *Nature* **593**, 67-73 (2021).

18. Guo, S.-X., Bond, A.M., Zhang, J. Fourier Transformed Large Amplitude Alternating Current Voltammetry: Principles and Applications. *Rev. Polarogr.* **61**, 21-32 (2015).

19. Zhang, J., Bond, A.M. Theoretical studies of large amplitude alternating current voltammetry for a reversible surface-confined electron transfer process coupled to a pseudo first-order electrocatalytic process. *J. Electroanal. Chem.* **600**, 23-34 (2007).

20. Kennedy, G.F., Bond, A.M., Simonov, A.N. Modelling ac voltammetry with MECSim: facilitating simulation–experiment comparisons. *Curr. Opin. Electroche.* **1**, 140-147 (2017).

21. Sun, Y.*, et al.* Highly Selective Electrocatalytic Oxidation of Amines to Nitriles Assisted by Water Oxidation on Metal-Doped α-$Ni(OH)_2$. *J. Am. Chem. Soc.* **144**, 15185-15192 (2022).

22. Guo, S.-X.*, et al.* Facile electrochemical co-deposition of a graphene–cobalt nanocomposite for highly efficient water oxidation in alkaline media: direct detection of underlying electron transfer reactions under catalytic turnover conditions. *Phys. Chem. Chem. Phys.* **16**, 19035-19045 (2014).

23. Adamson, H.*, et al.* Electrochemical evidence that pyranopterin redox chemistry controls the catalysis of YedY, a mononuclear Mo enzyme. *Proc. Natl. Acad. Sci. U.S.A.* **112**, 14506-14511 (2015).
24. Zhang, Y.*, et al.* Direct Detection of Electron Transfer Reactions Underpinning the Tin-Catalyzed Electrochemical Reduction of CO_2 using Fourier-Transformed ac Voltammetry. *ACS Catal.* **7**, 4846-4853 (2017).
25. Adamson, H., Bond, A.M., Parkin, A. Probing biological redox chemistry with large amplitude Fourier transformed ac voltammetry. *Chem. Commun.* **53**, 9519-9533 (2017).
26. Snitkoff-Sol, R.Z.*, et al.* Quantifying the electrochemical active site density of precious metal-free catalysts in situ in fuel cells. *Nat. Catal.* **5**, 163-170 (2022).
27. Hao, Y.*, et al.* Origin of the Universal Potential-Dependent Organic Oxidation on Nickel Oxyhydroxide. *ACS Catal.* **13**, 2916-2927 (2023).
28. Zouraris, D., Karantonis, A. Determination of kinetic and thermodynamic parameters from large amplitude Fourier transform ac voltammetry of immobilized electroactive species. *J. Electroanal. Chem.* **876**, 114729 (2020).